School of Chemistry

Secondary Electron Emission of Functionalised Diamond Transmission Dynodes

James Swarbrigg

This thesis is submitted in partial fulfilment of the requirements for the Honours Degree of MSci at the University of Bristol

Supervisor: Professor Neil Fox
Second Assessor: Professor Paul May
Physical and Theoretical Chemistry

Abstract

Diamond as a material has proven itself in modern science to be a resource of vast usefulness, especially within the electronics industry. One such use is the transmission dynode, which aims to extend the operational lifetime of the photocathode component within microchannel plate photomultiplier tubes, whilst also utilising the secondary electron emission characteristics of diamond during electron transmission to amplify the gain of electrons arriving at the microchannel plate, improving device performance and sensitivity. Two transmission dynodes were fabricated, beginning with 3.3 mm x 3.3 mm polycrystalline diamond substrates, from which thin central membranes were formed. Subsequent low concentration, boron-doped MWCVD growths on the two samples, followed by additional high concentration, boron-doped HFCVD growths formed conductive layers on the substrate, with final membrane thicknesses of 66 μm (Sample 2) and 60 μm (Sample 4) outlining the success of laser etching to form thin films. SEM analysis determined the crystal quality of the initial growth, followed by Raman spectroscopy identifying key peaks at 1332 cm^{-1} for the polycrystalline substrate, broadened boron-doped diamond peaks at ~480 cm^{-1} and ~1218 cm^{-1}, and a Fano zone-centred phonon peak before 1332 cm^{-1} characteristic of high boron concentration growths. These results indicated the crystal quality was high whilst also maintaining a high conductivity which was required for initial electron transmission through the dynode.

Functionalisation of the thin membrane was carried out using oxygen and scandium on Sample 4, leaving Sample 2 as H-terminated. Subsequent XPS analysis looked to examine the effects of applying a negative and positive electron affinity surface on the binding energies of the C1s core electrons of carbon, following literature which describes a negative electron affinity as crucial for secondary electron emission applications. A Kimble Physics flood gun was employed to simulate a photocathode electron source and used to irradiate an ScO-terminated sample. Whilst this test did indicate secondary electron transmission through the dynode, there was no observable electron multiplication ($\delta = 0.7$) as hoped. Because of this, the device would achieve its goals of acting as a protective layer for microchannel plate photomultiplier tube photocathodes, whilst also marginally improving on current protective layer electron collection efficiency. However, further work is required to confirm transmission results observed experimentally. This will involve developing an improved process to form thinner dynode membrane electrodes which can amplify electrons under bias more efficiently.

Acknowledgements

I would like to give many thanks firstly to Professor Neil Fox, my supervisor for the continuous advice and support received throughout the project and especially during the weekly meeting and a massive thank you to Professor Paul May for the support in meetings, providing guidance on next steps and frequently letting me know my ideas were slightly over-ambitious. Also to Liam Cullingford for supervising me in the lab and for the chance to experience work in the clean room, and for his help with any questions or queries through my time in the lab. I would like to also thank Dr. Ramiz Zulkharnay, for his continuous positive presence in the lab, helping extensively with CVD growths, and terminations and once again providing unwavering support and answers to any questions.

I would like to thank Dr. Jude Laverock for providing access to the NanoESCA facility and providing solution after solution when my samples refused to behave during XPS, and Dr. James Smith for help with any problems regarding the Raman spectrometer. Also to Catherine Monk for help with the laser cutter and providing solutions to any other small problems or queries.

Finally, I would like to show much appreciation for everyone who has been in and around the BUDGies diamond lab during my project, especially to my fellow undergraduate project students Ben, Jacob and Axel, the ‘Diamond Boys’. Working alongside these boys both in the lab and during our weekend late-night library sessions has been a pleasure, with so many memories made along the way. I wish them all the best for their future post-graduation and urge them to remember to ‘Live Más!’

Table of Contents

I - Glossary of Terms and Abbreviations

II – Glossary of Figures

III – Glossary of Tables

I - Glossary of Terms and Abbreviations

TSEY	Transmissive Secondary Electron Yield
HTHP	High Temperature High Pressure
GE	General Electric
CVD	Chemical Vapour Deposition
HF	Hot Filament
MW	Microwave Plasma
LED	Light Emitting Diode
SEY	Secondary Electron Yield
NEA	Negative Electron Affinity
SEE	Secondary Electron Emission
PEA	Positive Electron Affinity
UHV	Ultra-High Vacuum
PMT	Photomultiplier Tube
PC	Photocathode
MCP	Microchannel Plate
OLED	Organic Light Emitting Diode
FWHM	Full Width at Half Maximum
HST	Hubble Space Telescope
LEO	Low Earth Orbit
ALD	Atomic Layer Deposition
PCD	Polycrystalline Diamond
CAD	Computer-Aided Design
MFC	Mass Flow Controller
EMS	Emissivity
RIE	Reactive Ion Etching
ICP	Inductively Coupled Plasma
RF	Radio Frequency
SEM	Scanning Electron Microscopy
XPS	X-Ray Photoelectron Spectroscopy
ML	Monolayer
ZCP	Zone-Centre Phonon
PDoS	Primary Density of States

UPS	Ultraviolet Photoelectron Spectroscopy
PEEM	Photoemission Electron Microscopy

II – Glossary of Figures

III – Glossary of Tables

1.0 – Introduction

1.1 – Diamonds

1.1.1 – History

Historically a material symbolic of wealth and status, fuelling decades of war and violence within nations of central and west Africa, the public perception of diamond is often its glittering appearance and extensive use in the jewellery industry. The natural formation of diamond occurs in the Earth's mantle under extreme, high pressure, high temperature conditions, with the average growth time of natural diamonds being ~1 billion years,[1] and it is the past inability to recreate these conditions gave diamonds their value through their rarity. However, 20th-century advancements in laboratory equipment have now allowed the growth of synthetic diamond films to be a viable and cost-effective way of utilising diamonds without the mechanical strains and ethical concerns of traditional diamond mining. Because of this, the unique chemical and physical properties of diamond can be readily utilised and researched. One of the most widely known applications of synthetic diamond is in cutting tools, where deposits of diamond on the surface of tools improves the lifetime when cutting and milling non-ferrous materials, including alloys and ceramics,[2] but its applications cover a wider range of applications including the electronics industry and within particle physics, outlining the clear need for further research into this special material.

1.1.2 - Physical and Chemical Properties

Diamond is an allotrope of carbon which can be described as 'metastable' at atmospheric pressure.[3] Thermodynamically at 1 atm and room temperature, the sp^2 carbon form of graphite is more stable however kinetically, the energy barrier of transformation from diamond to graphite is very high, meaning the transition is extremely slow and negligible at standard conditions. The unique properties of diamond are not limited to just its extreme strength. The high thermal conductivity of single crystal diamond (24-25 $W\ cm^{-1}\ K^{-1}$) has applications in thermal management within high-power electronic devices.[4] The chemical inertness of diamond also benefits its wear-resistant nature, which is specifically useful in high radiation environments, or when exposing diamond thin films to fast-moving ionised gas.[5] The resilience to ionising radiation is attributable to its large band gap ($E_{gap} = 5.47$ eV),[4] which further contributes to diamonds wider variety of key properties which can be found in *Table 1.1.* Coupled with the strong covalent bonds within diamond, the carbon lattice will remain stable against ionising radiation and heavy ion bombardment for long periods of time. This gives diamond a wide range of potential applications as a protective membrane within radiation detectors and particle accelerators.[7]

Table 1.1 – Comprehensive summary of the physical and electronic properties of diamond. Property values taken from reference [4], [6].

Property	***Value***	***Application***
Density / g cm^{-3}	3.52	Cutting tools
Bulk Modulus / N m^{-3}	1.2×10^{12}	Cutting tools
Electrical Resistivity / Ω	10^{13}	Electronics
Thermal Conductivity / (W cm^{-1} K^{-1})	24 – 25	Heat sinks
Band Gap / eV	5.47	Electronics
Optical	Transparent from deep UV to far IR	Optical windows

High resistance to chemical and physical corrosion is crucial when managing the longevity of devices and sensors. Although the initial use of diamond within electronic devices may prove more costly, long-term labour and cost considerations associated with replacing sensors damaged by ion bombardment or radiation will outweigh the price of short-term expenses. Considering further the geometry of diamond, William Henry Bragg and William Lawrence Bragg were the first to analyse the crystal structure of diamond, describing the structure as having a 'face-centred cubical' crystal structure, with a lattice constant, $\alpha = 3.567$ Å.[8] [9] Within this crystal lattice, atoms of carbon bond through one 2s and three 2p orbitals on each carbon atom, giving rise to the sp^3 hybridised carbon.[10] Each carbon is covalently bonded to four adjacent carbon atoms in a tetrahedral arrangement, which is repeated throughout the lattice. The strength and regularity of this covalent lattice is responsible for the extreme strength observed. In comparison, carbon in the sp^2 graphite form, is arranged into two-dimensional planes which are held together by weak van der Waals forces arising from dipole forces originating from the motion of electrons between adjacent planar sheets.[11] This 'diamond-cubic' three-dimensional covalent structure, can be seen in *Figure 1.1*.[12]

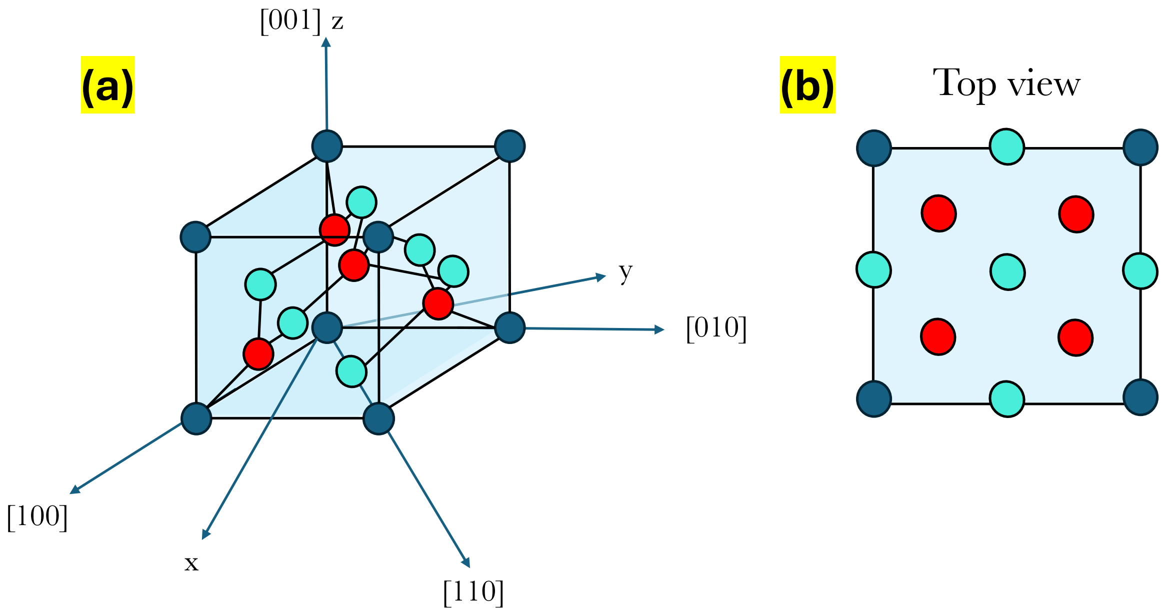

Figure 1.1 – Face centred cubic 3D structure common between diamond and silicon. Showing an axis representation and a top view highlighting the FCC nature of the covalent diamond lattice. Dark blue carbon atoms are positioned at the edges of the unit cell, whereas cyan atoms are positioned centrally in the outer faces of the cell. Red carbon atoms complete the diamond lattice, giving each atom tetrahedral coordination. This diagram was created with reference to [12].

To create membranes of around 50 – 100 μm required in transmission diamond dynode devices or within quantum computing,[13] laser cutting is often required to etch predesigned shapes down to the desired thickness for optimal performance within devices. It is the extremely strong three-dimensional structure possessed by both diamond and silicon that allows for these thin film membranes to remain physically stable down to tens of microns. In transmission dynode applications, thinner dynodes are required to maintain a high transmissive secondary electron yield (TSEY).[14]

1.1.3 - High Temperature High Pressure Formation

1951 saw the formation of the high pressure diamond group at General Electric (GE), with the aim to solve the problems associated with previous attempts of growing diamond, and in 1955 GE successfully grew the first lab grown diamond.[15] The GE approach to growth involved the conversion of graphite to diamond under high pressure and high temperature (HTHP) conditions. The conversion of graphite to diamond is a notoriously slow process, hence catalytic metals including iron, nickel and copper were used.[16] Conditions used by the GE group to convert graphite to diamond involved heating to around 1870 K, whilst maintaining a pressure of 7 GPa. The goal of maintaining these HPHT conditions was to shift thermodynamic stability to favour the formation of diamond with the aid of a metallic flux to lower the temperature required for conversion.[17] Although this technique led the way for diamond growth at the time, the process was expensive to run and maintain and was time-consuming. This resulted in the development of a more optimal method of diamond growth, chemical vapour deposition, which quickly proved to be a more efficient and cost effective method to grow single crystal and polycrystalline diamond.

1.2 - Chemical Vapour Deposition

1.2.1 - Chemical Process

It wasn't until 1962 when the first literature discussing low-pressure diamond growth was published, in the form of a Patent submitted by William G. Eversole, growing diamonds on a seed crystal under metastable conditions.[18] However, reports of low pressure growth were often met with an aura of scepticism as it was assumed growth rates were too slow to be a viable replacement for HPHT growth.[19] Improvements in synthetic diamond growth techniques in 1968 saw growth rates of 250 μm hr^{-1} achieved by Deryagin *et al.* [20] However, follow up work by Deryagin also demonstrated how diamond could be grown from seeding techniques on non-diamond substrates such as silicon and metals.[21] This advancement by Deryagin was particularly important to the future of diamond growth, solving the issue of expenses associated with early homoepitaxial growth on single crystal substrates. This growth technique, which was attainable through chemical vapour deposition (CVD), allowed for far more cost effective synthetic growth of diamond both for further research into applications and also for industrial uses.[22]

CVD is commonly performed through two techniques, hot filament (HF) and microwave plasma (MW) CVD. Within both reactor types, the presence of an abundance of hydrogen gas within the reaction chamber is essential for successful growth. In both cases, the hot filament and microwave plasma aim to dissociate hydrogen molecules into hydrogen radicals. When using a single crystal diamond substrate the surface is naturally terminated with hydrogen. Following the reaction scheme in *Figure 1.2*, the process proceeds through the reaction of a hydrogen radical with a surface atom of hydrogen on the diamond substrate, leaving a carbon surface radical. Methane (CH_4) is also added to the gas stream as a source of carbon the reaction between H and CH_4 forms active CH_3 radicals which upon contact with the vacant surface radical, adding to the diamond lattice. This process is repeated on adjacent surface sites followed by additional H abstraction from the terminal CH_3 group, leaving radical CH_2 groups on the surface. Finally, this radical group can react with neighbouring carbon atoms forming linkages, eventually adding a new layer of diamond to the covalent lattice.[23] This process however will likely not proceed in such a step-wise manner as expressed in *Figure 1.2*. Any non-diamond sp^2 carbon which remains on the surface unreacted will be quickly etched back into the reaction 'soup of gases' by H atoms frequently striking the surface.[24]

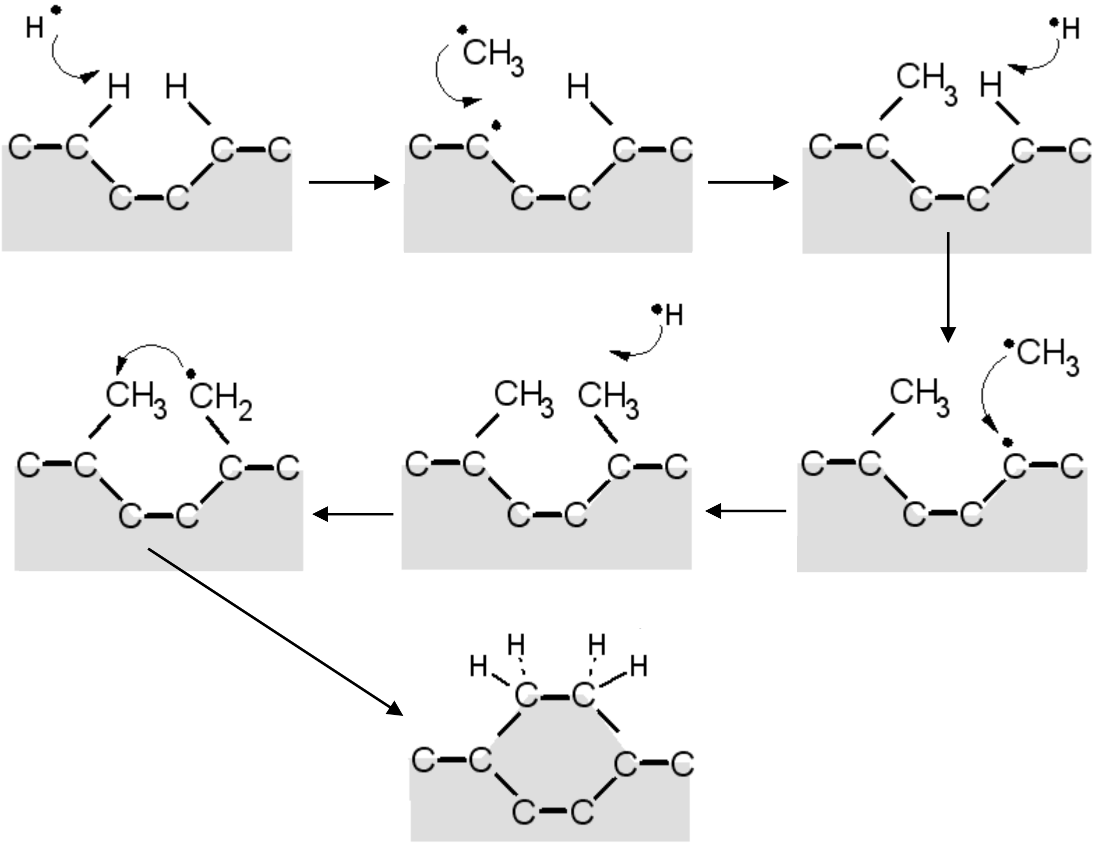

Figure 1.2 – A reaction diagram showing the stepwise formation of diamond using chemical vapour deposition processes. Diagram was rearranged from reference [23].

1.2.2 - Microwave Plasma and Hot Filament CVD

Although the general operation of MWCVD reactors is typically more expensive, it is often regarded as a better method of chemical vapour deposition than HF, producing higher quality crystals coupled with greater growth rates due to the enhanced stability over longer periods of time.[25] HFCVD has drawbacks such as the need to replace the filament which is typically made from tungsten or tantalum. During the degradation of the filament, metal particles can enter the gas stream and contaminate the diamond growth. In environments such as undergraduate labs, where HFCVD is used for student growth, slight contamination may not be as great of an issue, however, the risk of contamination would not be acceptable in industries which require consistent high purity growths such as electronics and sensor applications. This does not mean the use of HFCVD is limited, with its main benefit, being the low operating cost, making it useful for research and early stage development of devices.[26]

Microwave plasma CVD is the main choice for industrial production of diamond films, primarily due to achieving a consistently higher purity and quality of diamond than hot filament deposition. Also, as the plasma acts as the heat source there is less regular maintenance required on the reactor to replace components. Operational times for diamond growth are also typically shorter. MWCVD reactors typically require 5-6 kW power supplies in lab, however, in commercial growth where high area and fast growth is desired, power supplies up to 100 kW are used.[27] Once the hydrogen plasma is ignited, the plasma is focussed as a spherical shape above the molybdenum sample plate. Both homoepitaxial and heteroepitaxial growth can be achieved through MWCVD, however for heteroepitaxial growth (for example polycrystalline diamond on silicon), nucleation pre-treatment of the silicon substrate is required.[27] [28] Common pre-treatment techniques include seeding and mechanical abrasion, in which diamond dust is manually seeded onto the i-silicon substrate. This technique is often faster than electrospray methods, however, mechanical abrasion typically provides a less even surface coverage. Furthermore, lattice mismatches when using substrates such as silicon can result in defects and weakening of the growth due to increased stress. Promising solutions to this include the use of iridium substrates for single crystal diamond growth, exhibiting closely matched atom spacing and reduced lattice mismatch.[29] In general, for homoepitaxial growth onto single crystal diamond, only acid pretreatment is required to clean the substrate to remove any residue that may remain from suppliers.

1.2.3 - Doping

Doping is a widely used technique in chemistry to alter the electrical properties of a material through the introduction of carefully selected impurities to the reaction mixture during the growth of a substrate. Doping is used extensively in the semiconductor industry, in particular, doping of single crystal silicon and crystalline gallium arsenide due to their good room temperature stability.[30] Some common applications of semiconductor materials include solar cells, transistors and light-emitting diodes (LEDs), all of which commonly operate at room temperature and pressure and require conductivity.[31] The idea of semiconducting materials is to have a conductivity between that of an insulator and a metal, which relies on the transfer of electrons and holes throughout the bulk. Dopants can be classified as n-type or p-type dopants. As depicted in *Figure 1.3,* in n-type doping, a molecule with a greater number of valence electrons than the bulk material, such as nitrogen or phosphorus sits below the conduction band donating electrons up into the conduction band. In p-type doping, a molecule with fewer valence electrons, sits above the valence band and receives electrons from the valence band, generating holes.[32] In relation to boron-doped diamond, boron with 5 valence electrons sits about the valence band of carbon (6 valence electrons), acting as a p-type dopant.

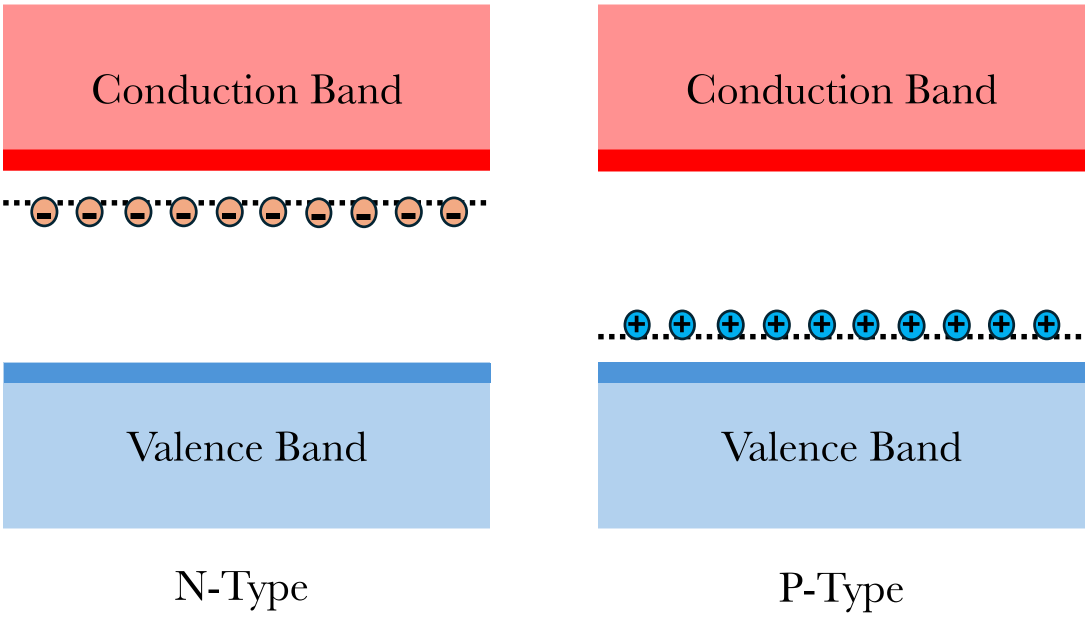

Figure 1.3 – Diagram depicting the position of dopant levels in n-type and p-type doping, with valence electrons (-), sat below the conduction band and holes (+), sitting above the valence band.

The addition of boron to diamond will have minimal effect on the crystal lattice of diamond at low concentrations maintaining its strength and uniform structure. However, as the boron doping concentration is increased the mechanical properties of diamond including hardness and elastic modulus are affected especially at high concentrations.[33] Furthermore, the density of defects will also increase inducing strain on the crystal lattice or resulting in dislocations.[34] In thin film applications, this would not be desirable and would negatively impact the stability of the diamond films at low thickness, resulting in mechanical failure of the substrate during the etching process.

1.2.4 – Morphology of Diamond

CVD diamond surfaces can have a wide range of surface morphologies. The exact surface structures typically originate from the choice of substrate or choice of nucleation technique. For example, the use of manual abrasion with diamond powder can be used to increase nucleation density and therefore increase the grain boundary concentration, however, this technique can damage the substrate, giving poor control of the surface structure.[35] In applications where reactivity, conductivity or etch rate needs to be closely controlled, the choice of, and subsequent control of specific surface orientations of diamond is crucial.[36], [37] Such specific diamond crystal orientations can be typically categorised as <100>, <110> and <111>,[37] with a diagrammatic representation of each orientation shown in *Figure 1.4*.

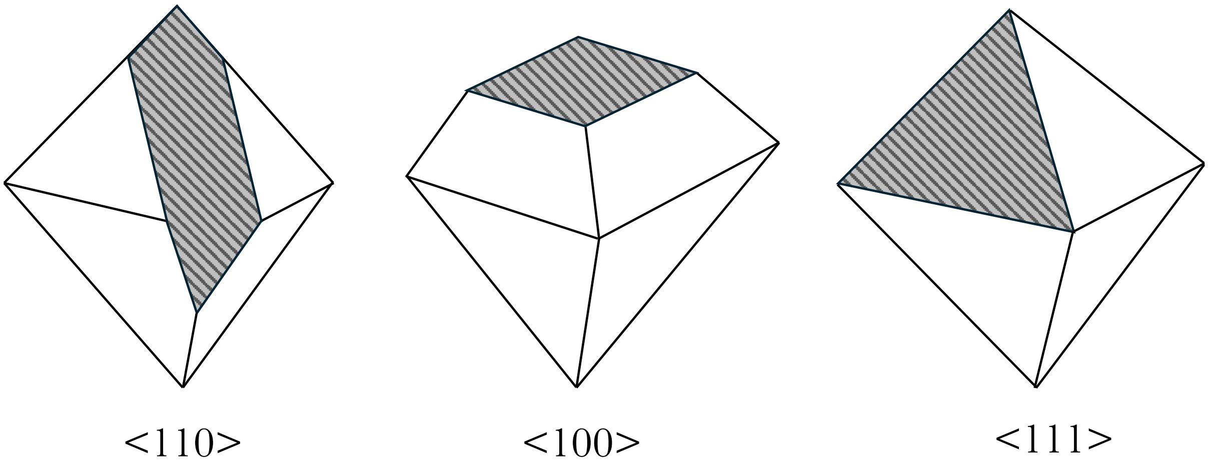

Figure 1.4 – Diagram depicting the three common crystal orientations present on the diamond surface, <110>, <100> and <111>, with the individual facets shown in the shaded area, adapted from reference [38].

For secondary electron emission applications, crystal orientations should be considered, in particular when using single crystal diamond. Whilst this is still somewhat applicable to polycrystalline diamond, PCD surface crystal orientations are often disordered and non-consistent. However, regarding optimised transmission dynodes which utilise single crystal substrates, clean, H-terminated, single crystal diamond surfaces exhibit maximum secondary electron yield with <111> oriented surfaces. This is as opposed to <100> surfaces, which are reported to exhibit slightly lower SEY.[39] However, this changes when alternative functionalisation of the surface is considered. In a study by J. E. Yater *et al.*, in which caesium was used, <100> surfaces exceeded the yield of secondary electrons in comparison to <111>.[39] <100> surfaces have been found to have the greatest density of dangling bonds of the three mentioned orientations, and upon addition of oxygen or in this case caesium to the surface, the C-C dimer bonds on the hydrogenated <100> surface breaks and binds more readily to the functionalising atom of choice. The presence of such C-C dimer bonds in a hydrogenated <100> surface also likely accounts for incomplete hydrogenation of the clean surface, partially raising the electron affinity of the <100> surface in comparison to <111>, meaning SEY yields would be lower for a H-terminated <100> surface as observed.[39] For this reason, when using single crystal diamond, especially for clean hydrogenated surfaces, <111> surfaces should be prioritised for maximum SEY, however for functionalised surfaces, <100> diamond surfaces should be prioritised.

1.3 - Surface Termination

1.3.1 – Negative Electron Affinity

When working with CVD diamond, the term electron affinity, χ, is used to describe the relationship between the conduction band minimum and the vacuum level, V_{VAC}.[40] To achieve a negative electron affinity is to have the conduction band minimum positioned below the vacuum level, which, as a result, means no additional energy input is required to allow electrons to escape to vacuum, assuming such electrons already possess the band gap energy required to be promoted from the valence band to the conduction band. A visual representation of the band diagrams can be seen in *Figure 1.5* with a comparison showing how the vacuum level is positioned within a material possessing a positive and negative electron affinity.

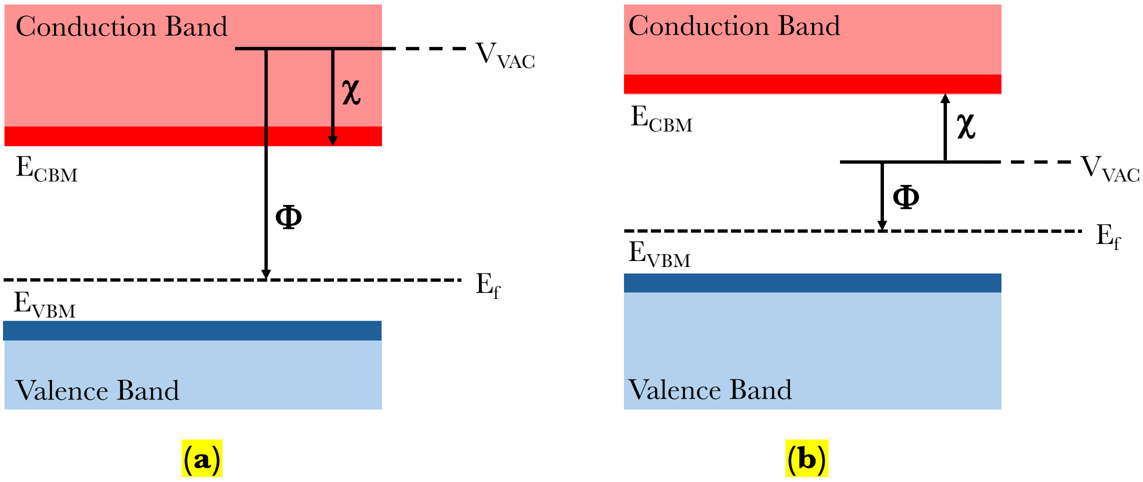

Figure 1.5 – Band diagrams showing (a), a true positive electron affinity and (b) a true negative electron affinity as would be expected from H-terminated diamond surface. In the diagram the term (ϕ) represents the work function. The vacuum level (V_{vac}) is also positioned lower, below the red conduction band when a NEA is present at the surface. This diagram was adapted from reference [41].

The work function of a material is commonly denoted by ϕ and can be defined as the minimum energy required for an electron to be removed from the fermi level to the vacuum level at 0 K.[42] A further benefit of CVD techniques for the growth of diamond is the resulting H-terminated surface, which is achieved through further exposure of the surface to H_2 gas at high temperatures in the reactor chamber. As the growth process is stopped, the hydrogen gas reacts with and terminates the dangling carbon bonds on the surface.[43] H-terminated (100) diamond surfaces have been extensively studied in the literature, with a work function of 4.9 eV and negative electron affinity (NEA) of -1.3 eV commonly reported.[44] [45] Within photomultiplier applications, such as within vacuum photodetectors,[46] dynode membranes must have high secondary electron yield (SEY) which is obtainable with a NEA surface and low work function within diamond membranes.

1.3.2 - Secondary Electron Emission

The emission of electrons from the surface of a material as a result of charged primary particles impacting and penetrating the bulk of the material is referred to as secondary electron emission (SEE). When high energy incident electrons penetrate the material as represented in *Figure 1.6*, the kinetic energy from the incident particles are transferred to electrons in the bulk. For a secondary electron to escape the surface to vacuum it must receive sufficient energy greater than the work function of the material to escape the surface to vacuum.[47]Various energy loss mechanisms can impact the resultant energy and the secondary electron yield, differing between metals and insulating materials. In metals, secondary electrons generated in the bulk lose energy through interactions with conduction electrons, lattice vibrations and defects. On the other hand in insulators, secondary electrons lose energy through the excitation of valence electrons to the conduction band. In wide band gap materials such as diamond, secondary electrons with insufficient kinetic energy cannot partake in electron-electron collisions in which secondary electron energy is lost. Furthermore an absence of electron scattering results in a far smaller amount of energy lost as secondary electrons travel through the material. This gives rise to large escape depths and gives insulating materials a greater SEY.[48] This makes diamond an excellent choice for devices which utilise secondary electron emission.

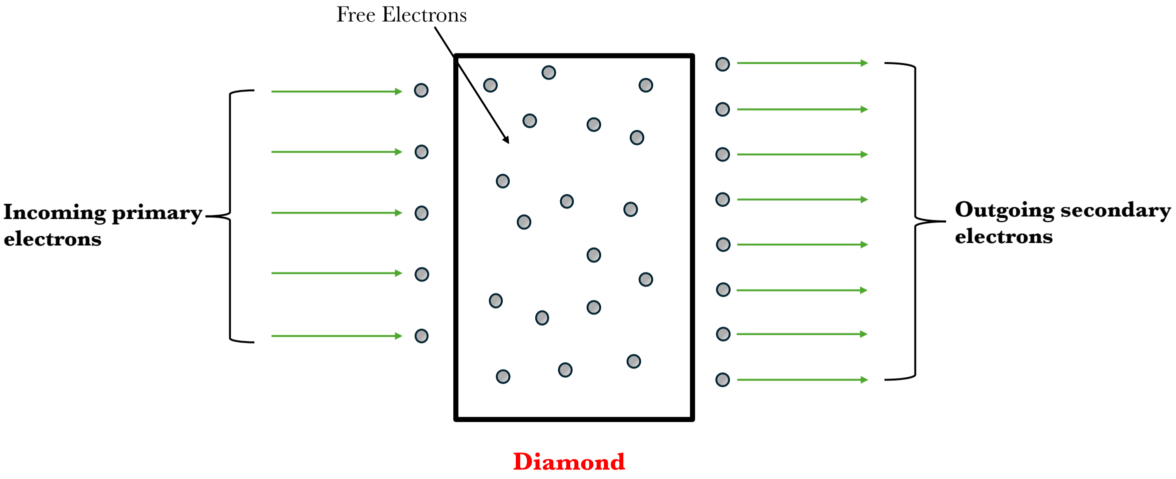

Figure 1.6 – A simplified diagram representing the process of secondary electron emission from a diamond membrane. Incoming primary electrons in this case are fired from an electron beam. The diagram is adapted from reference [49].

Consequently, the SEY (δ) of a material describes the ratio between the total number of emitted secondary electrons referred to as the secondary electron current, I_s, and the number of incident electrons referred to as the primary electron current, I_p and can be found in *Equation 1.*[50]

$$\delta = \frac{I_s}{I_p} \qquad \textbf{(1)}$$

For electron multiplier applications, a $\delta > 1$ is required, meaning for every 1 primary electron that impacts the membrane, some integer value greater than 1 of secondary electrons must exit the material. Regarding H-terminated boron-doped diamond, maximum δ values of 45 at incident electron energy 2.4 keV have been reported.[51] For dynode applications, high SEY values are crucial for electron amplification. To achieve this, thickness, dopant concentration and surface characteristics should be optimised, alongside potential variation of surface termination with oxygen and metals.

1.3.3 – Hydrogen Termination

Hydrogen termination of CVD diamond surfaces is amongst the most reported diamond surface termination in the literature. A commonly used method to prepare H-terminated surfaces when using MWCVD is to re-expose the substrate surface to plasma under a hydrogen gas atmosphere for a short period of time.[52] The primary function of H-termination in relation to dynode devices is to achieve an NEA surface, enhancing electron emission. Hydrogen achieves an NEA surface due to the formation of positive C-H surface dipoles as shown in *Figure 1.7*. This dipole layer will shift the potential of diamond with respect to vacuum.[40] H-termination also benefits the diamond surface physically through stabilisation of the surface. This leads to an overall stabilisation of the bulk, preventing phase transformation to graphite when exposed to reactive conditions or high temperatures.[53]

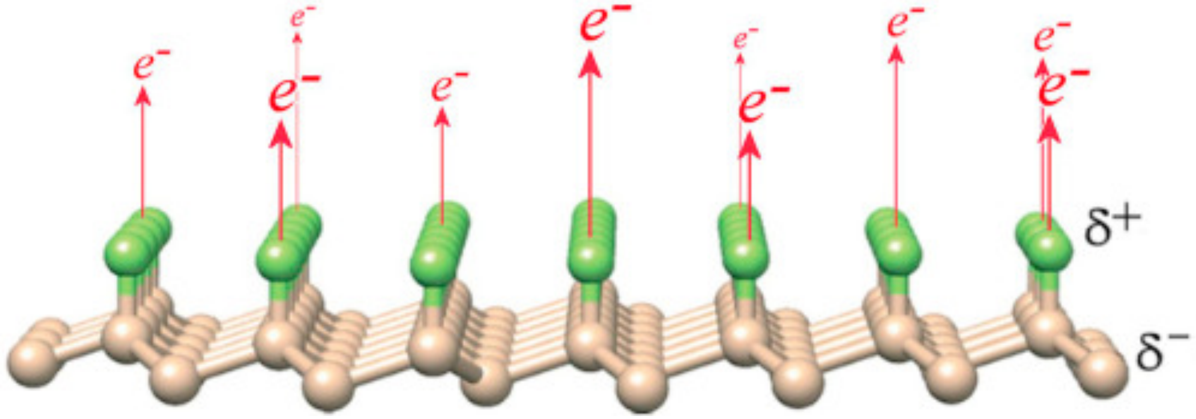

Figure 1.7 – A diagram taken from M. C. James *et al.*, [54] showing the functionalised diamond surface. The terminating hydrogen atoms are represented in green, with electron emission represented through the red electrons leaving the surface.

1.3.4 – Metal Oxide Terminations

Metal-oxygen terminations of the diamond surface, for example, lithium termination of diamond surfaces have been studied and reported in the literature as an alternative to hydrogen when forming an NEA surface. Focusing initially on lithium, it is the lightest of the alkali metals and can be considered as more appropriate than the heavier alkali metals for reduction of the work function in the context of the smaller elements of carbon, hydrogen and oxygen typically associated with the diamond surface. The deposition of lithium on both a clean diamond surface and an oxygenated diamond surface are viable options for reducing the work function, however, lithium deposition on an oxygenated surface has been shown to exhibit both a large adsorption energy and a true NEA.[55] The oxygenation of the surface alone also has an impact on the work function but alternatively results in the formation of a positive electron affinity (PEA) requiring energy input for electrons to move to the vacuum level, whilst also eliminating surface conductivity, undesirable properties for electron emission applications.[56] Alternatively, the formation of a monolayer of Li adsorbed onto a fully oxygenated surface through physical vapour deposition, forms a stable C_d-O-Li surface dipole which maintains the NEA of diamond at 800°C. A promising alternative to H-termination, benefitting the longevity of electron emission devices under extreme conditions.[58] Li-termination is most commonly achieved through annealing of the diamond surface. S. Ullah *et al.,* describes a technique which uses a Li_3N solution as a source of lithium, followed by drop casting onto the clean, O-terminated diamond surface. The NanoESCA facility available at the University of Bristol is then used to anneal the surface under temperatures ranging from 500 to 850 °C under ultra-high vacuum (UHV) conditions.[58]

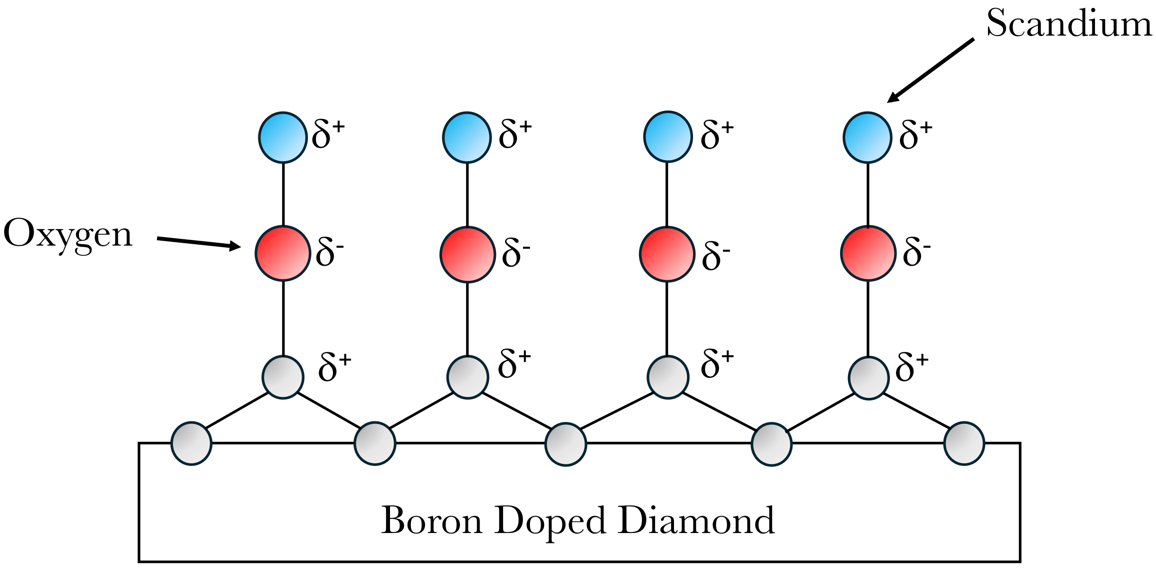

Figure 1.8 - A diagram adapted from reference [57] showing a simple surface arrangement of scandium deposited on an oxygenated surface. In relation to previous discussions, scandium can be interchanged with lithium, however this should be done with respect to differing effects interchanging such metals may have on the electronic properties of the surface.

Alternatively, a ScO-terminated surface as shown in *Figure 1.8*, can also provide a greatly enhanced NEA surface. One benefit of pursuing a ScO-terminated surface is its enhanced stability at higher temperatures. Although heavier group 1 elements, have been found to induce lower work function values (ϕ = 1.5 eV),[58] weak adsorption results in a lack of overall stability when any form of heat is applied. As a result the caesium monolayer will desorb entirely around 500 °C.[59] However, when examining the thermal properties of a Sc-terminated oxygenated surface, a far higher thermal stability is observed (> 1200 °C), which will remain stable, maintaining a high electron emission yield at temperatures around 500 °C.[61] This makes Sc-termination of an oxygenated surface a far more practical option for dynode applications with a focus on operational lifetime, especially when the substrate is being bombarded with high energy electrons over extended periods of time. Considering the deposition of scandium to a diamond surface, deposition uses electron-beam evaporation of pure scandium rods, a simpler deposition process than lithium, giving higher control of coverage.[61] To compare the NEA surface values obtained across the three proposed surface termination approaches (hydrogen, Li-O, Sc-O), refer to *Table 1.2* below comparing the NEA values and adsorption energy of each termination.

Table 1.2 – Table comparing NEA and thermal stability (temperature at which functionalised surface atoms begin to desorb) for each of the selected terminations. Values stated in the table are taken from literature reports however can vary based on the literature source.

Termination	***NEA/ eV***	***Thermal Stability***	***References***
Hydrogen	-1.1	400 °C	J. M. A Beattie *et al.*[62]
Lithium (Oxygenated)	-2.1	800 °C	S. Ullah *et al.*[63], T. L. Martin[30]
Scandium (Oxygenated)	-3.7	1200 °C	R. Zulkharnay *et al.*[61]

Comparing values in the table it is clear that far better performance would be expected from a ScO-terminated surface in comparison to hydrogen and lithium. Whilst H-termination is far more efficient to apply than metal oxide termination, the low thermal stability is problematic and limits the implementation to low temperature applications to reduce hydrogen desorption. Alternatively, scandium, when tested through a range of annealing temperatures up to 900 °C, exhibited a very slight reduction of 0.6% in surface coverage, implying the bonding to oxygen is very strong,[64] and therefore a more sensible choice for termination of diamond structures operating in high energy environments.

1.4 – General Applications of Transmission Diamond Dynodes

The influence behind the development and testing of functionalised transmission diamond dynodes is for wider use within vacuum photodetectors, electron counting and radiation detection devices, typically found in association with linear accelerators in particle physics experiments. Current devices within this industry exhibit the need for improvement in both lifetime and higher count rate capabilities.

1.4.1 – An Introduction to Dynodes

Dynodes are thin electrode membranes that serve the purpose of electron multiplication, typically through a photomultiplier tube (PMT). Dynode devices rely on the secondary electron emission properties of materials as discussed earlier, to amplify charge through a PMT. Dynodes have two common operating modes, reflection and transmission as expressed in *Figure 1.9*. In reflection applications successive dynodes within a tube are supplied with a higher positive potential, resulting in electron acceleration and high multiplication of the initial electron count. This wave of secondary electrons is collected as a current pulse and is screened for pulse height analysis.[65] In transmission photomultiplier applications, much thinner diamond films are required, as the secondary electron pulse must travel through multiple films maintaining sufficient energy to reach the detector for pulse height analysis. In reflection applications, transmission dynodes also rely on the application of a positive bias, which increases at each dynode to accelerate electrons, to compensate for energy loss during the generation of secondary electrons.[14], [65]

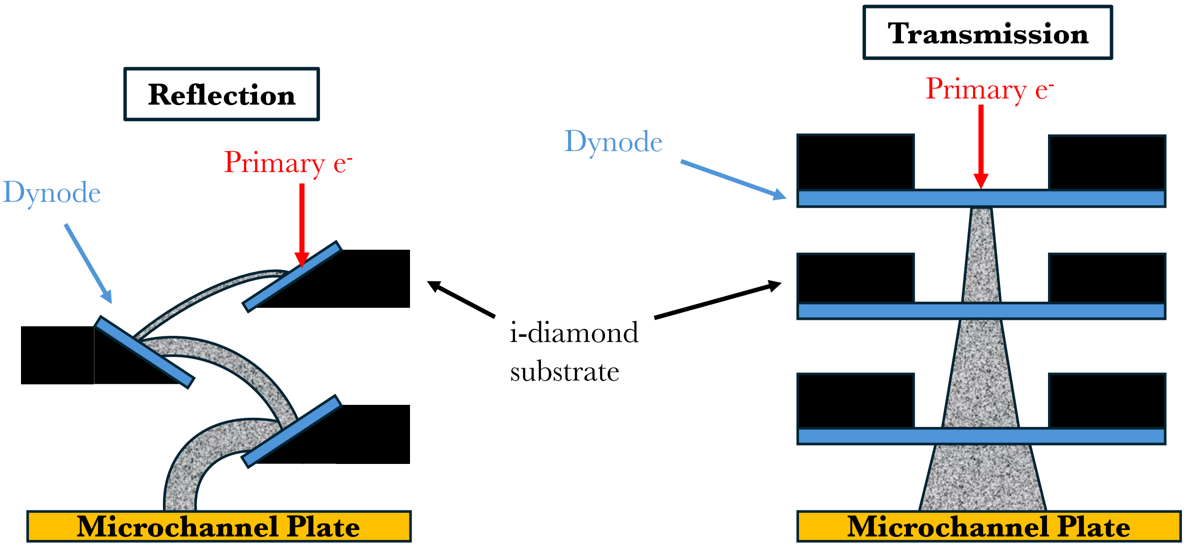

Figure 1.9 – A diagram representing the different electron multiplication mechanisms in (a) reflective, and (b) transmissive dynode membranes, with the blue thin film representing diamond. The diagram used was created with reference to [14].

A comparison between transmission dynodes and reflection dynodes by S. X. Tao *et al.*, identified several advantages to using transmission dynodes. These included (I) an improvement in quantum detection efficiency and pulse amplitude fluctuations relating to its effectiveness in use as a photodetector. (II) A reduction in transit-time fluctuations; (III) uniform response over a large area, eliminating transit-time differences from different parts of the photocathode (PC); (IV) the ability to operate in the presence of intense magnetic fields when originated along the axis of the tube (low magnetic field sensitivity); and (V) short total transit-time and dead-time.[14] Beyond lifetime extension and performance benefits of photomultiplier tubes it is clear utilising dynodes in transmission mode possesses superior properties compared to reflection.

1.4.2 - Microchannel Plate Photomultiplier Tubes

Microchannel plate-photomultiplier tubes (MCP-PMTs) are used within particle acceleration experiments, high precision photon counting, low energy light detection and radiation detection.[66], [67] The structure of a MCP-PMT is made up of a photocathode, where incoming light is converted into an electron of a specific energy, and a microchannel plate, which consists of a glass, circular array of tubes, each typically ranging from 5 – 20 μm in diameter,[68] as expressed in *Figure 1.10*.

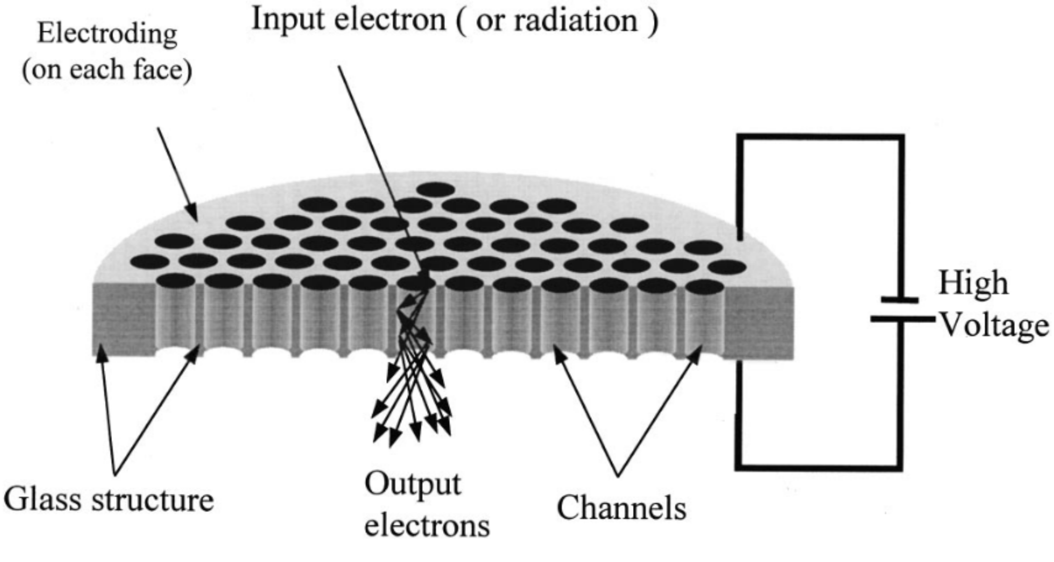

Figure 1.10 – A diagram showing the microchannel plate component of an MCP-PMT, taken from reference [69].

The conversion of incident photons to an electric current at the photocathode occurs due to the photoelectric effect, in which photons above a threshold frequency liberate electrons from the photocathode.[70] Electrons emitted from the photocathode enter traverse the vacuum tube and are then funnelled through the large array of individual capillaries on the microchannel plate. Each capillary acts as an electron multiplier, through the generation of secondary electrons, allowing the individual capillaries to act as reflection dynodes generating high electron multiplication. Finally, a high voltage electric field is applied as shown in *Figure 1.10*, causing secondary electrons to drift, aiding with transit through the device.

High gain MCPs are very sensitive to low energy electrons, making them suitable for low intensity signal detection.[71] The development of MCP-PMTs prototypes was first reported by V.V. Anashin *et al.,* in 1994, proposed for fast time-of-flight scintillation counters, with the MCP replacing previously used fine mesh PMTs.[72] The general structure of MCP-PMTs can be summarised in the *Figure 1.11* diagram, also expressing the positioning of the dynode in between the photocathode and the MCP.

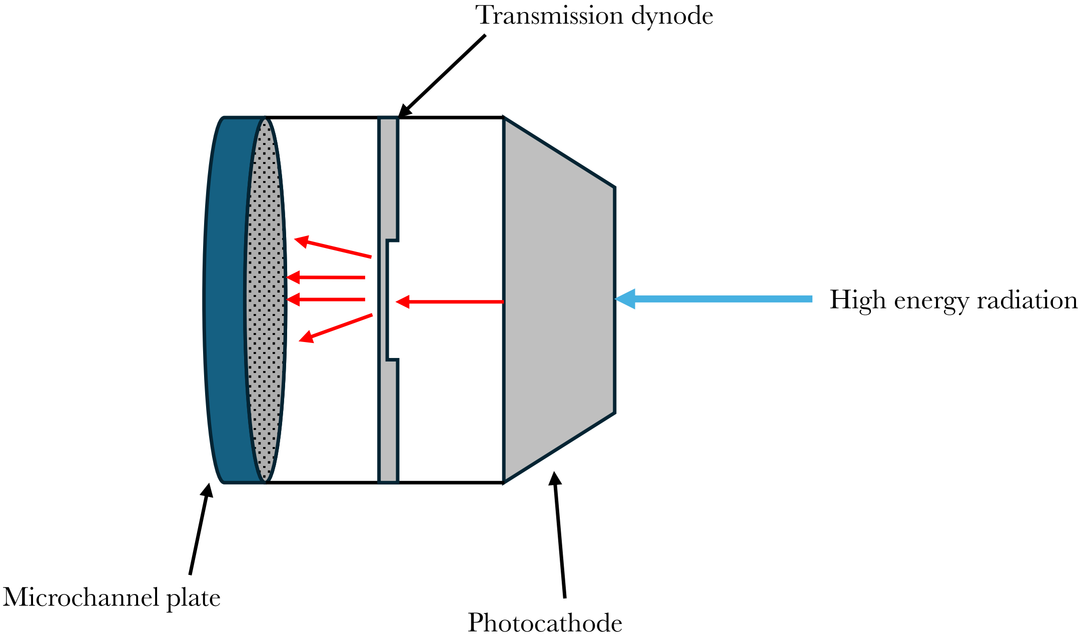

Figure 1.11 – A Simple diagram representing the general structure of an MCP-PMT. The addition of a transmission dynode in between the photocathode and the microchannel plate is in line with the aims of the project to test and develop an optimised dynode membrane to use in MCP-PMTs. Electrons generated at the photocathode and secondary electrons arriving at the microchannel plate are represented by red arrows.

One unique performance feature of MCP-PMTs, outside of its ability to operate in high magnetic fields and harsh radiation environments includes high gain measurement abilities, relating to the number of secondary electrons generated during amplification in the MCP. The gain of an MCP-PMT is controlled *via* the applied voltage across the MCP and is essential in ensuring efficient single photon detection.[73] It is crucial that gain remains high, as a reduction in the gain can increase the maximum count rate of the device leading to saturation.[74] MCPs operate with negative exponential pulse height distribution.[75] This is to allow for accurate detection of low amplitude single photons, whilst also being able to distinguish these photons from the background noise. It is true that reducing the gain can allow MCP-PMTs to operate at higher count rate capabilities, whilst also increasing the detector lifetime,[76] however, a lower gain makes it difficult to accurately detect photon emission events and to distinguish actual detected photons from the background.

Further desirable properties include the time response of the MCP. During the development of MCP-PMTs, it is crucial that the fast time response is maintained, as to not hinder the performance of the device. The transit time of electrons through early MCPs is around 250-800 ps, with times as short as <200 ps for single plate MCPs.[75] However recent developments have found single photon time resolution to be as low as ~70 ps FWHM, vastly outperforming multi-anode PMTs in testing.[77] Although such multi-anode MCP-PMTs benefit from enhanced special resolution and positional sensitivity,[78] achieving a greater time resolution for high sensitivity, detection device applications of MCP-PMTs is essential. For example, when observing decay events lasting within the 250-800 ps range, signal sampling would need to be carried out in time increments to allow for the decay shape to be resolved.[79] In cases where material cost is high, or sample scarcity is a limiting factor, the ability to carry out incremental screening on a limiting number of samples would be important, as opposed to single screening of 10 samples at different points of a decay event, which could be achieved using a device with the ability to detect on the <100 ps time scale.

1.4.3 – Single Photon Counting Applications

By far the most widespread application of MCP-PMTs is within high precision single photon counting experiments where there is potential for further development aiming to optimise performance and lifetime of MCP-PMT devices. Photon counting experiments require the arrival of a photon at the photodetector, which gives a signal response when the photon is converted at the photocathode. Experiments testing the performance of photodetectors require the use of electron beam devices, which will be discussed later in the project, however, key considerations for the use of an electron beam to analyse photomultiplier tubes is the distance of the beam source to the device, which should be kept constant to allow for accurate determination of performance and sensitivity when operating at picosecond timing precision.[80]

1.4.4 – Fluorescence and Phosphorescence Experiments

High precision photon detection and counting is essential for experiments analysing the excited state lifetime of organic molecules. When a molecule relaxes from its excited state to its ground state, the excess energy absorbed during excitation is released through radiative processes of fluorescence and phosphorescence as expressed in the Jablonski diagram in *Figure 1.12*.[81] The excited state lifetime of these molecules is often extremely short lived, on the femtosecond or even picosecond scale, requiring the detection of radiative photons to be almost instantaneous after irradiation of the molecule. Developments in these areas can contribute to a wider range of applications including photovoltaics, chemical sensors, organic light emitting diodes (OLED) and bio-screening, applications which are in continual need for growth in areas including medical and the technology industries.[82]

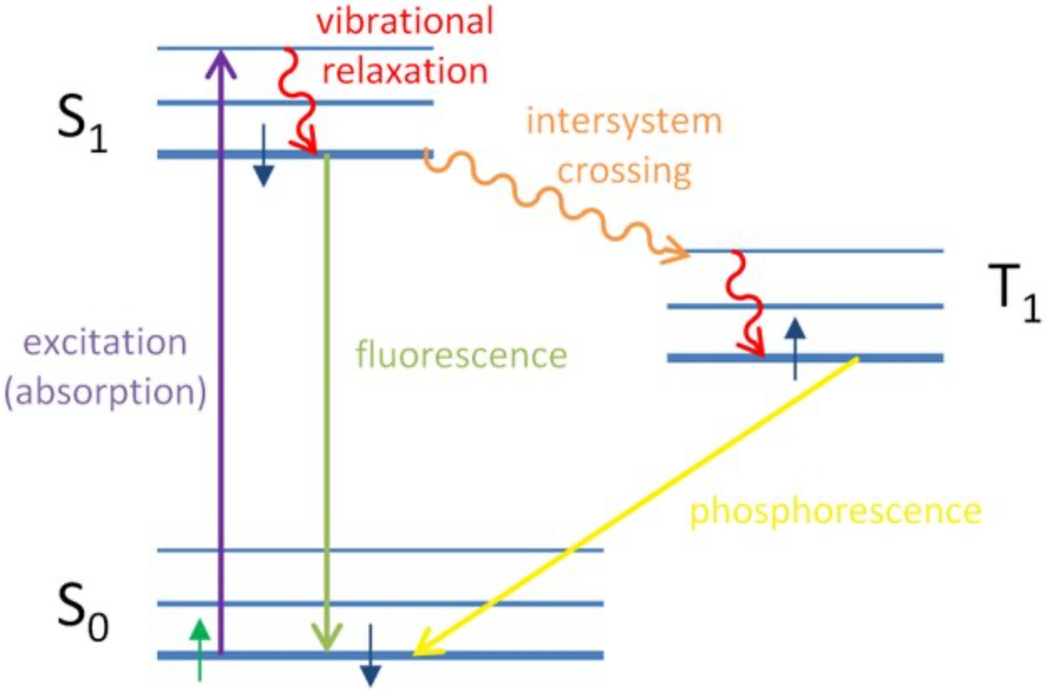

Figure 1.12 – The Jablonski diagram, representing the phosphorescence and fluorescence decay mechanisms at which high precision photon counting devices would be used to measure, taken from reference [83].

1.4.5– High Energy Particle Physics and Cherenkov Radiation

Cherenkov radiation was first reported in literature by Pavel Cherenkov in 1934, in which the luminescence of uranyl salts was induced by radium γ-rays. The early experiment technique relied on human eye detection of the light radiation, a far stretch from the current detection equipment utilised in particle physics experiments.[84] The emission of Cherenkov radiation as photons of light occurs when a charged particle travels through a transparent medium at a speed greater than the speed of light in that medium, which can be solid or liquid. Photon emission is a result of localised polarisation along the path of travel of the particle, emitting electromagnetic radiation when the polarised molecules return to their original states.[85] MCP-PMTs such as the example shown in *Figure 1.13,* are used within particles physics and particle acceleration experiments as Cherenkov counters, aiding in the detection and quantization of energy to determine characteristics of long-lived charged particles, primarily their masses.[86]

Figure 1.13 – Images of a commercially available Photonis MCP-PMT, showing the front window (left) and the back (right) and the component. This device is described as specialising in fluorescence imaging, Cherenkov detection and high energy physics. Images were taken from reference [87].

1.4.6 – Low Energy Imagining in Space Telescopes and Further Application in Space Devices

An MCP-PMT-type device made up part of an addition to the Hubble Space Telescope (HST) in 2003, further outlining the wide range of applications held by MCP-PMTs and thus transmission dynodes. The device installed on the HST was a high throughput UV spectrograph with a CsI photocathode.[88] A more recent 2022 review by H. Tomio *et al.,* discussed developments in highly sensitive photon-counting detectors for space-borne communication applications.[89] Specific properties of interest that were mentioned as beneficial to the device were maintaining a high quantum efficiency up to 800 nm and also its high radiation tolerance, allowing it to be suitable for the space environment having a long lifetime. Degradation of quantum efficiency or photocathode performance aboard these space-borne devices is particularly problematic when considering the cost and difficulty of replacing the detector. This not only outlines the importance of the lifetime but indicates the requirement for further improvement within the lifetime of these devices. Difficulty in replacing MCP-PMT devices can lead to space devices being decommissioned, contributing to the ever growing issue of man-made space debris polluting low Earth orbit (LEO), which poses the threat of unplanned collision with active devices or spacecraft.[90]

1.4.7 – Transmission Dynodes for Improvement of MCP-PMT Devices

The development of transmission diamond dynodes for the improvement of MCP-PMT devices will explore two approaches. A long-term improvement approach relating to the lifetime of the MCP-PMT looks to solve problems relating to cost reduction and frequency of replacement, alongside a shorter term, more direct approach focusing on the performance relating to the secondary electron emission characteristics of the diamond film. Whilst the theory has been largely discussed previously in the project, following sections will look to directly cover the current problems, and the benefits and potential drawbacks associated with implementing transmission diamond dynodes into current MCP-PMT technology.

1.4.8 – Lifetime Considerations

Until recently, the limited lifetimes of MCP-PMTs was the main drawback which prevented more widespread and frequent use, however their extremely fast time responsive characteristics and compact nature was highly advantageous and in demand, especially in particle identification experiments as Cherenkov detectors. Because of this, causes of ageing had to be identified and strategies were to be developed to tackle this issue.[91] The primary cause of ageing and degradation of the photocathode is through MCP material, or residual gas atoms present in the PMT may be ionised in the electron avalanche, and be accelerated towards the PC.[91], [92]

The electron avalanche or more formally referred to as Townsend discharge, is an ionisation mechanism in which the electron generated at the photocathode, within an applied electric field can collide with residual gas molecules and atoms, further liberating an electron. These liberated electrons further ionise gas molecules, resulting in a cascade effect, visualised in *Figure 1.14*, within the PMT forming more reactive gaseous ions, which as previously mentioned can be accelerated back towards the PC, resulting in gradual ionisation damage.[93], [94]

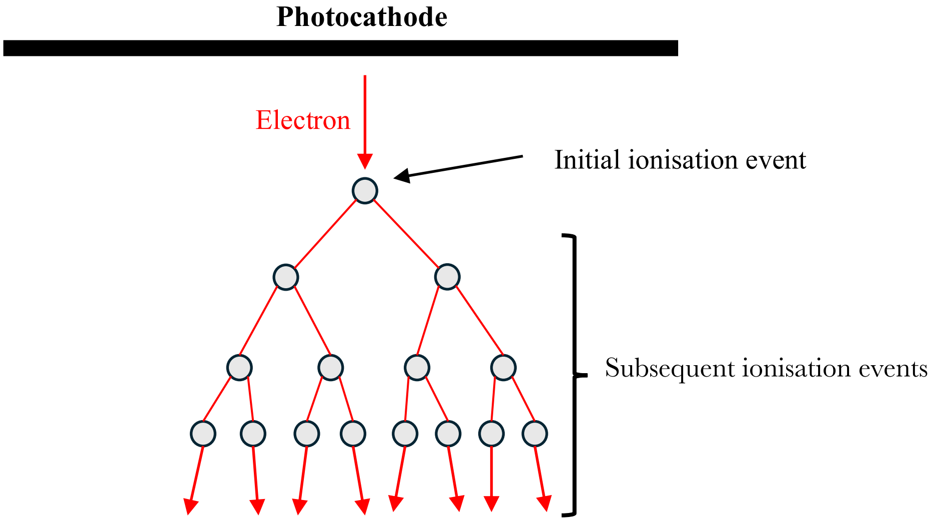

Figure 1.14 – Simplified diagram showing a Townsend discharge mechanism occurring at the photocathode. Expressed in the diagram is a 'chain reaction' style of events in which the number of ionisation events initially increases exponentially. This diagram was adapted from reference [95].

The effect of continuous bombardment of the PC by ionised gas particles is an overall reduction in quantum efficiency, with quantum efficiency, η, being the measure of how well the photocathode will convert photons into electrons described by *Equation 2*.[96]

$$\eta = \frac{Number\ of\ electrons\ emitted}{Number\ of\ photons\ injected} \qquad \textbf{(2)}$$

In 2011 the best commercially available MCP-PMTs degraded to only 50% of their original quantum efficiency after exposure to < 200 mC/cm^2 charge density.[97] However, it was reported in 2018 that the addition of a protective, Al_2O_3 film prevented the ionised gas particles from being back accelerated at the photocathode which significantly slowed down the degradation of the photocathode, however, a new issue was presented in the form of a drastically reduced collection efficiency of electrons arriving at the MCP. It was reported by T. Jinno *et al.*, that the addition of a metal oxide layer in between the PC and MCP leads to a reduction in collection efficiency by ~ 60% compared to a device without a film.[91], [98] This study showed that if the lifetime was to be increased then a film must be incorporated, with metal films still being used in industry to extend the lifetime of the devices. However, this was at the consequence of a reduced performance. It should be noted that where metal thin films aren't employed, MCP-PMT lifetime can be optimised through the application of a higher quality vacuum, aiming to prolong the introduction of residual gas particles into the system, and heavily polished MCP surfaces achieved through electron scrubbing of the MCP. However, whilst these methods did show an increase in lifetime in a study by A. Lehmann *et al.,* this improvement was not as significant as the introduction of a protective film.[91], [99]

1.4.9 - Atomic Layer Deposition

Atomic layer deposition (ALD) is a layer growth process which succeeds in growing very thin layers, in this case within MCPs. Whilst ALD as a process is similar to CVD, the key difference is the sequential manner in which precursors are inserted into the reaction chamber through pulses, as opposed to conventional CVD in which all gaseous precursors are present in the reaction chamber during growth.[100], [101] ALD is another technique for lifetime optimisation within recent literature that looks to extend the lifetime once again of the photocathode through the deposition of a thin metal oxide film, typically aluminium oxide or magnesium oxide onto the surface of the pores within the MCP.[102] ALD techniques operate differently from typical thin film protective layers due to the deposition being directly on the MCP. This aims to protect the photocathode through a focus on the surface stability of the MCP to prevent positive ion feedback to the photocathode.[103] However, this protection layer would only be active against MCP-related outgassing, and would not address the issue that a thin protective layer between the photocathode and the MCP would solve, relating to residual gas present in the PMT. But an additional benefit that shouldn't be ignored is the performance benefits that are gained through the addition of an ALD layer, in relation to high secondary electron emission achieving a high gain. The metal oxide coating within the pores of the MCP not only effectively seals the MCP surface but also enhances SEE properties.[104] This is an advantage over the use of a metal thin protective layer which actively reduces collection efficiency and therefore the gain of the device. Considering the obvious advantages and drawbacks that both ALD and a thin metal protective film present, an optimal device shouldallow for both a high gain, giving enhanced performance to the standard, 'unprotected' MCP-PMT, whilst also greatly protecting the photocathode from positive ion feedback, with the use of a tough material which will maximise the overall lifetime of the device.

1.4.10 – The Diamond Transition Dynode

Tying together previous sections it is obvious there is a clear need for transmission dynode development, harnessing the benefits of both enhanced SEE and also lifetime. The most recent reported structure as of 2025 that follows the same protective layer structure aiming to amplify gain and restrict ion feedback, is in the form of a stainless steel calendared woven mesh of 30 μm thickness and 50% optical transparency achieving a total gain on the level of ∂ (10^5–10^6).[105] This leaves diamond as a very promising candidate to rival both performance and lifetime extension abilities of current steel mesh protection layer. Benefitting from a strong SEE, enhanced by improving the NEA surface through surface functionalisation, leading to gain improvements and strong radiation hardness, protecting the often delicate photocathode. Unlike previous ALD Al_2O_3 layers, which require difficult ultra-thin deposition to maintain quantum efficiency, and metal thin-films which have been found to greatly reduce quantum efficiency, diamond transmission dynodes will aim to amplify charge emission from the photocathode, whilst remaining less challenging to reproduce and implement than ultra-thin layers, which are often fragile and susceptible to environmental damage.

1.5 – General Project Aims

This project aims to fabricate a diamond transmission dynode device which will attempt to solve the two problems currently associated with MCP-PMT-type vacuum photodetectors such as reduced photocathode lifetimes, through the feedback of gaseous ions. This transmission dynode will act as a protective layer preventing this backflow of ions whilst allowing the efficient transmission of electrons so as to not compromise the electron gain of the device. Recently adopted methods to prolong the lifetime of the photocathode involve the use of metal or metal oxide protective layers, however, this has been found to reduce the gain of electrons arriving at the detector significantly, impacting device vacuum photodetector performance.[98] The diamond transmission dynode will look to improve on current gain and collection efficiency values, with a TESY ideally ≥ 1, which would drastically improve device sensitivity and performance with the benefit of lifetime improvement. Analysis into secondary electron yield optimisation will be achieved through varying surface terminations including standard H-termination and metal-oxygen terminations, with the goal of maximising surface negative electron affinity.

To fabricate such devices, thin films will be etched from commercially available substrates, followed by electrically conductive boron-doped diamond growths, termination of the substrate membrane surface and final electron beam testing to simulate operation within a vacuum photodetector-type device.

2.0 – Methods

2.1 – Dynode Design and Fabrication

The design and testing of a novel transmission dynode structure implemented a wide range of tests and techniques to fabricate each layer and component of the device. The fabrication process explored an alternative method of creating thin films of diamond. Typical methods to form thin, diamond films involve a laser-etch, wet-etch process, typically using a seeded silicon substrate, followed by growth of an intrinsic diamond layer, laser etching and a final wet etch using KOH.[106] However previous and current work within the lab found the initial growth of the i-diamond layer to be weak and prone to delamination and fracture of the membrane. The laser etch approach aimed to increase the strength of the thin central membrane at lower thicknesses by using a polycrystalline diamond (PCD) starting substrate. Laser etching also maintains grain boundaries, which may be uneven or deformed in a growth on a nucleated silicon substrate, contributing to increased substrate and membrane strength.

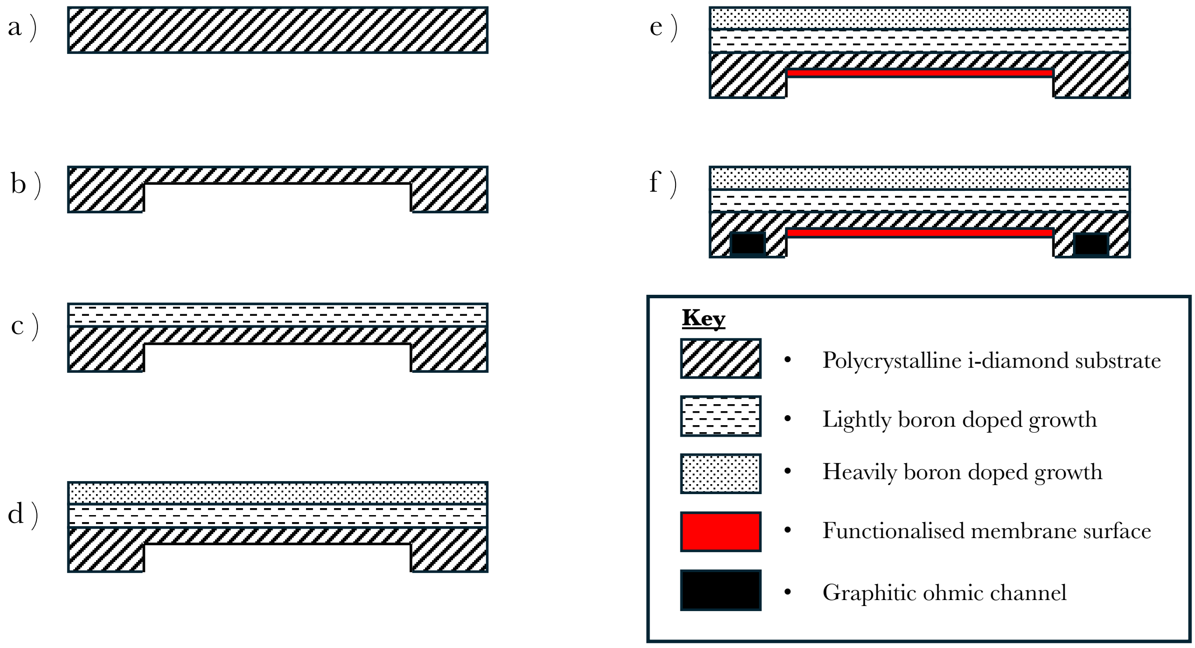

Figure 2.1 – Schematic representing the makeup of each layer within the transmission dynode. (a) shows the starting substrate provided by Element Six, which was laser etched (b), and then BDD was deposited in (c) & (d). The inner cavity surface was then functionalised with ScO and H (e), with the ohmic channel deposited through laser etching (f).

As expressed in *Figure 2.1,* from the initial 5 starting polycrystalline diamond substrates (a), only 3 survived laser etching without complete detachment of the central membrane, with 2 out of 3 then being taken to completion without any membrane cracking. However, the 2 completed dynodes remained structurally stable to allow for additional CVD growth, membrane functionalisation, surface analysis and testing. This demonstrated the benefits of using an alternative, 'purely laser' etching strategy however there is room for improvement across the board with the fabrication process which will become evident within the results.

2.1.1 – Laser Micromachining of the Substrate

Figure 2.2 – Image of the Oxford Lasers Alpha 532-XYZ-AU micromachining system used to laser etch samples.

The starting substrates used in the fabrication of the transmission dynodes were 3.3 mm x 3.3 mm polycrystalline diamond off cuts, taken initially from a 10 mm x 10 mm, 0.3 mm thick free-standing PCD substrate provided by Element Six. The PCD had been cut prior to beginning the project by a previous student but acted as a good starting substrate in which mistakes or breakages would be less costly. The laser micromachining setup was an Oxford Lasers Alpha 532–XYZ–A–U micromachining system shown in *Figure 2.2*, and the parameters as shown in *Table 2.1,* set for the laser etching runs remained constant.

Table 2.1 – Parameters used for laser etching of the central cavity of the starting PCD substrate. Pulse frequency, cut width and etch speed were kept constant however power was reduced gradually as the diamond became thinner,

Power/ %	20 – 40%
Pulse Frequency/ kHz	25 kHz
Width of Cut	0.005
Etch Speed/ (mm s^{-1})	2

The gradual reduction in laser power in line with increasing material removal was carried out to give better control of the thickness whilst also reducing the risk of 'blow-out' of the central membrane within the laser. The cavity was 2 mm x 2 mm, with the etching pattern incorporating a cross-hatched design with liner removal in both the X and Y direction, which was found experimentally to give a smoother finish than etching across only one 2-dimensional axis. Etching and cutting designs used within this project were designed using ALPHACAM computer-aided design (CAD) software which transposed designs onto Cimita v4.3.6 laser control software, simplifying etch parameters in the X and Y axis. Rough control of etching in the Z direction can be achieved by varying the power and etch speed of each pass.

2.1.2 - Ohmic Channel Deposition

To attempt to provide conductivity to the outermost channel, a graphitic, ohmic channel was deposited on the outermost face of the intrinsic polycrystalline diamond substrate. 3.57 mm^2 of conductive graphitic carbon was deposited using the following laser parameters as shown in *Table 2.2*.

Table 2.2 – Parameters used for laser etching of the ohmic channel of the starting PCD substrate with no parameters varied.

Power/ %	40
Pulse Frequency/ kHz	25
Width of Cut	0.005
Etch Speed/ (mm s^{-1})	1

2.1.3 – Laser Cutting of Transmission Stand

To allow for testing of the transmission properties of the dynode device, a stand was designed and cut from aluminium foil, comprising of arms to attach to bolts within the electron beam sample plate, along with sides to support the platform above the plate at which charge from the electron beam arrived. To allow the central functionalised membrane to be visible to the charge collection plate, a circle (diameter = 2.6 mm) was cut out of the centre. The complete structure had to be slightly modified to ensure no contact was made with the collector plate, and an image of this can be found in *Figure 2.3*. This was once again designed using ALPHACAM and the following parameters can be found in *Table 2.3.*

Table 2.3 – Parameters used for laser cutting of the transmission stand required for transmission testing of the dynode within the electron beam gun.

Power/ %	90
Pulse Frequency/ kHz	25
Width of Cut	0.005
Etch Speed/ (mm s^{-1})	1

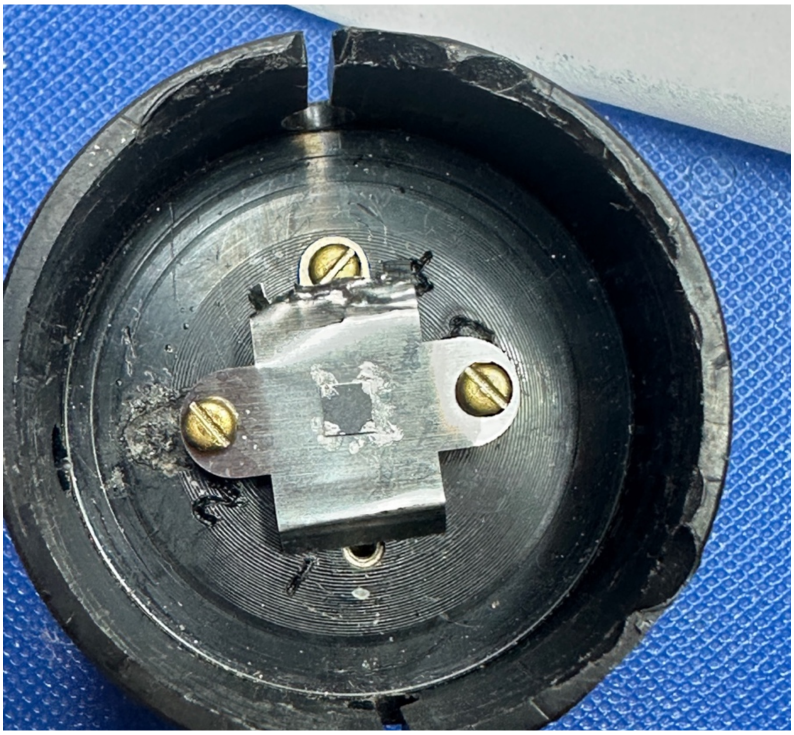

Figure 2.3 – Image of the transmission stand with the dynode mounted with silver DAG adhesive, prior to e-beam testing.

2.1.4 – Microwave Chemical Vapour Deposition Process

The initial growth on both etched Sample 2 and 4 substrates was carried out using an ASTeX-type MWCVD reactor, depositing undoped and boron-doped diamond on the PCD substrate. The initial deposition was ran for 2 hours from the point at which the plasma was struck, depositing a layer of very lightly boron-doped diamond. The growth conditions can be found below in *Table 2.4*, in which growth conditions were the same for both samples.

Table 2.4 – Growth conditions used in the initial MWCVD boron-doped diamond growth on samples 2 and 4. Growths were carried out on independently on samples therefore temperature may vary however it is expected to see a temperature around 1000 °C for such conditions.

Temperature/ °C	1051
Methane flow rate/ sccm	12.5
Hydrogen flow rate/ sccm	300
Diborane flow rate/ sccm	Residual (0)
Power/ kW	1
Pressure/ Torr	100
Time/ h	2
Emissivity	0.19

Testing the surface resistance of the MWCVD growths found resistances of 19 MΩ (Sample 2) and 13 MΩ (Sample 4), with an estimated growth thickness of around 20 μm, implying a growth rate of 10 μm h^{-1}.

During the MWCVD process, a high power microwave generator emits microwaves, which are channelled through the waveguide, focused through the quartz window into the vacuum reaction chamber. Reflected power is controlled through the tuning stubs and gas flow is controlled externally through the use of a mass flow controller (MFC). The microwave power utilises electromagnetic radiation to form gaseous radicals within the plasma 'ball' which engulfs the substrate.[107] These radicals then form bonds on the substrate surface which is positioned on a centred molybdenum plate on the sample stand. Once growth is complete, a vacuum valve is opened to expel the remaining gas from the reaction chamber. A full diagram of an MWCVD reactor can be seen below in *Figure 2.4*.

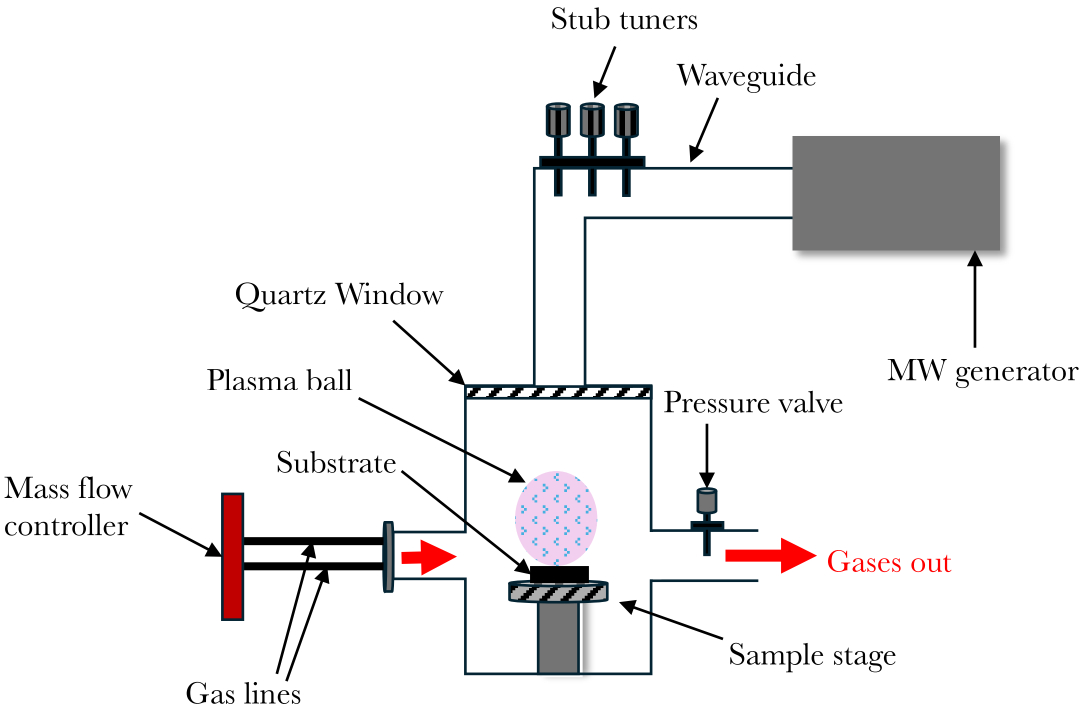

Figure 2.4 – Schematic of a microwave powered chemical vapour deposition reactor created with reference to [108].

To perform hydrogen plasma treatments to remove graphitic carbon, or to hydrogen terminate the surface, an alternative diborane-free ASTeX-type MWCVD reactor was used. The addition of an alternate diborane free reactor is crucial to ensure there is no unwanted cross-contamination of residual boron in i-diamond growths. Hydrogen plasma treatments to remove graphitic carbon ran for 30 minutes, with consistent conditions including a hydrogen flow rate of 300 sccm, a power of 1.2 kW a pressure of 110 Torr and an emissivity (EMS) of 0.15. Alternatively, hydrogen plasma treatment to hydrogen terminate samples prior to later analysis utilised conditions which gradually reduced pressure and power as described in *Table 2.5* in 2 minute intervals.

Table 2.5 – Parameters used in the H-termination treatment of dynode Sample 2 and Sample 4. Across all hydrogen plasma-related treatments EMS = 0.15.

Hydrogen Flow Rate/ sccm	*Time*/ mins	*Pressure*/ Torr	*Power*/ kW	*Temperature*/ °C
300	2	140	1.4	~900
300	2	90	1.0	~700
300	2	30	0	~20

2.1.5 – Hot Filament Chemical Vapour Deposition

Due to limitations in using the MWCVD reactor as a result of work being carried out to upgrade the system, later growths during the project had to be carried out using hot filament chemical vapour deposition. A thin, heavily boron-doped diamond layer was deposited on top of the original growth, with a growth rate of 1 μm h^{-1}. Surface resistance of the growth was found to be 43 Ω (Sample 2) and 35 Ω (Sample 4), with the following conditions as shown in *Table 2.6* below.

Table 2.6 – Parameters used in the HFCVD growth on samples 2 and 4. It is important to note that diborane was introduced to the reaction chamber after 30 minutes of exposure to only hydrogen and methane.

Pressure/ Torr	20
Current/ A	4
Hydrogen Flow Rate/ sccm	200
Methane Flow Rate/ sccm	2
Diborane Flow Rate/ sccm	0.5
Substrate Temperature/ °C	906
Filament Temperature/ °C	2000
Distance Between Filament and Substrate/ mm	3
Time/ h	2

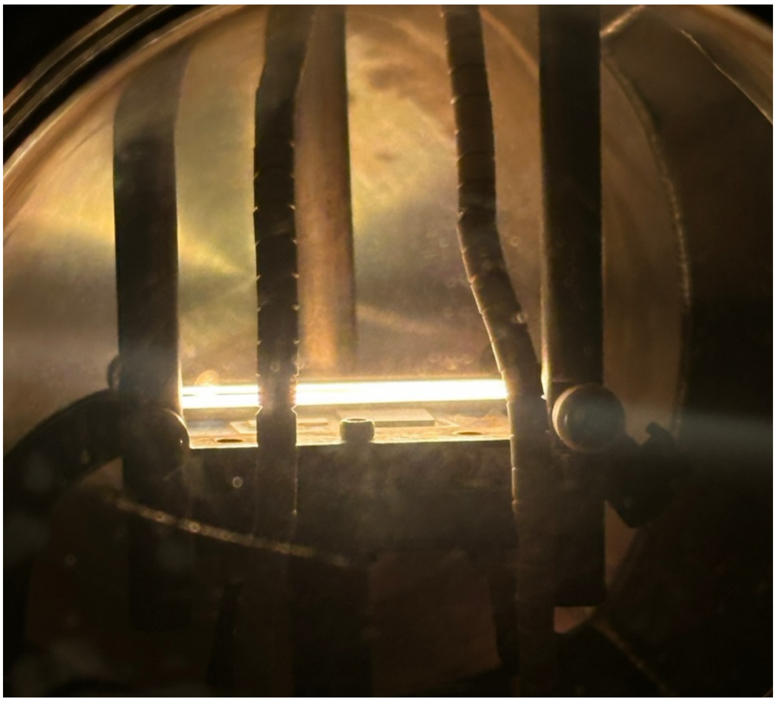

Figure 2.5 – Image of HFCVD deposition of heavily boron-doped diamond, in which samples can be seen below the glowing tantalum filament.

The filament used was a freshly prepared tantalum coil which can be seen in operation in *Figure 2.5*, which was heated gradually for 10 minutes prior to the addition of gas to confirm the structural integrity of the coil. Following a 2 hour growth, 2 µm of boron-doped polycrystalline diamond was deposited. A full schematic of the reactor used can be found in *Figure 2.6*.

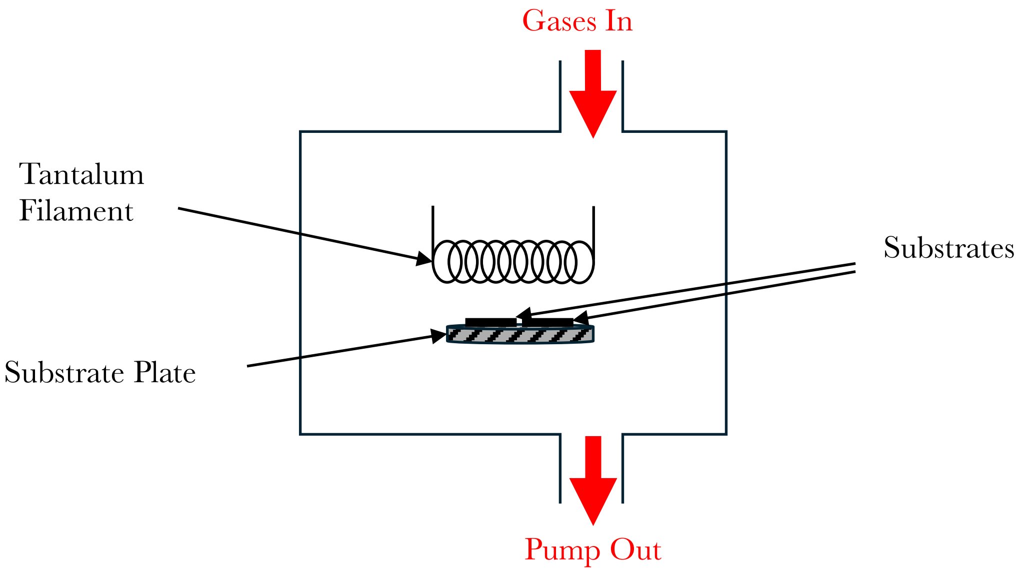

Figure 2.6 – Schematic of a hot filament chemical vapour deposition reactor created with reference to [109].

2.1.6 – Silicon Inductively Coupled Plasma Reactive Ion Etching

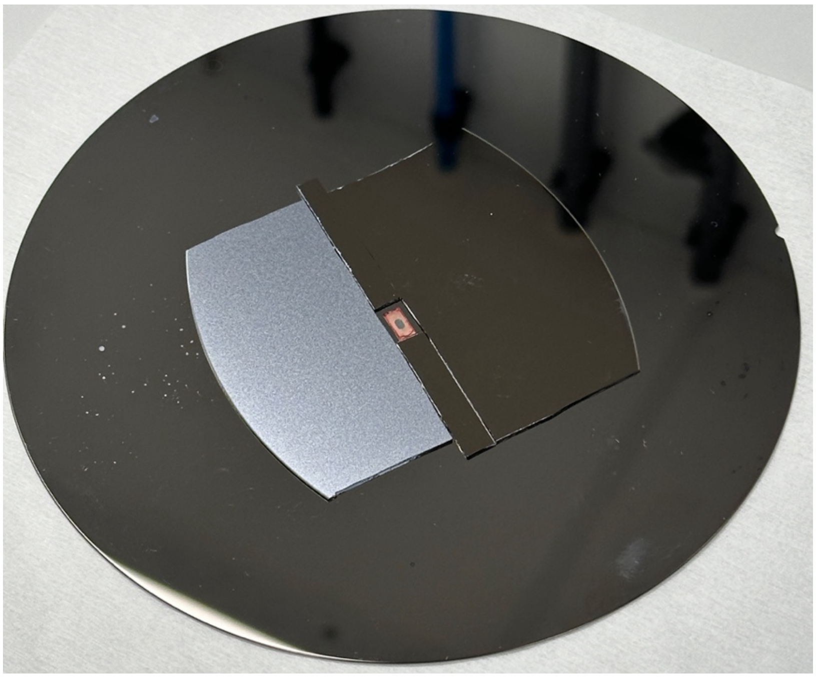

Figure 2.7 – Image of the ICP RIE plate loaded with reference offcuts of silicon, surrounding the thin film PCD diamond substrate. The central 'unmasked' area of the structure acted as the thin membrane.

Whilst this etching technique was not directly used on any of the samples, this was a technique that was used within the project to create similar thin film diamond membranes. Using an Oxford Instruments PlasmaPro 100 ICP RIE, a pre-existing PCD diamond membrane structure was selectively etched using oxygen gas at a flow rate of 50.0 sccm at a forward power of 1500 W. The chemical etching process occurred through the formation of oxygen radicals, which form volatile gases (CO and CO_2)[110], etching diamond with excellent control of the etch rate. The use of plasma assisted reactive ion etching (RIE) allows for anisotropic pattern transfer alongside strong dimensional control which makes it a useful technique for shaping hard materials such as diamond.[111] However Inductively coupled plasma (ICP) RIE is a high density plasma technique, meaning that at higher pressures and higher bias power (RF power), isotropic etching can occur. Although both parameters can be adjusted, finding the correct balance between pressure and radio frequency (RF) power can be difficult, meaning for individual samples optimisation of conditions or the utilisation of pre-existing conditions would be required to minimise isotropic etching effects.[112] The completion of repeated etching runs achieved a thickness estimated to be around 50 μm (etch rate = 40 nm min^{-1}), in which removal post ICP etching was determined using a Dektak surface profiler. Thin offcuts of silicon were used as a reference as shown in *Figure 2.7* for thickness and comparing silicon thicknesses pre and post ICP RIE to allow for the calculation of an accurate etch rate.

Whilst isotropic etching tendencies may cause issues in manufacturing exact structures, ICP RIE etching benefits from both a superior selectivity when utilising the correct gas mixture, alongside more precise control of the thickness, with a far reduced likelihood of membrane fracture in comparison to standard laser etching. For this reason, a continuation of the project may look to explore the use of the combination of such techniques mentioned in later stage fabrication of thinner transmission dynodes.

2.1.7 - UV-Ozone Cracking for Oxygen Termination

Ultraviolet ozone cracking was used to terminate the diamond surface with oxygen. UV light was emitted from a mercury lamp, generating ozone directly from the air above the cavity surface of the dynode within a UVO-cleaner kit (Model 42, Jetlight Company Inc.).[113] O-termination of the diamond surface results in a raising of the work function, alongside filling vacancies on the diamond surface and the removal of graphitic diamond. A run time of 30 minutes was set for Sample 4 to achieve a full monolayer coverage,[113] which had been previously H-terminated and left overnight under vacuum to maintain a clean surface

2.2 – Structural Characterisation Techniques

2.2.1 – Raman Spectroscopy

Raman spectroscopy is a very useful characterisation technique, which can be used in tandem with chemical vapour deposition to analyse the purity of diamond growths. The spectrum provides structural information in the form of chemical shifts, regarding primarily vibrational and rotational energy levels of the structure, alongside other lower frequency modes.[114] The structural fingerprint is obtained through the inelastic scattering of monochromatic light, the source of which is typically a laser, operating at a wavelengths within either the visible, near-infrared or near-ultraviolet region.[115] The scattering of monochromatic light during the spectroscopic analysis can be categorised into two different scattering processes. Inelastic Raman scattering results in the gain or loss of energy from the differing vibrational energy associated with atoms or molecules engaged in the process. As a result, the emergent light differs in energy from the light impinging on the substrate giving the user direct structural information regarding the substrate. Molecular or atomic matter responsible for elastic Rayleigh scattering, on the other hand, neither loses nor gains energy in the process, resulting in scattered light having identical energy to that which is impinging on the sample. The Raman process can be further split into two types, Stokes and anti-Stokes, in which the Stokes process results in a molecular transition to a higher energy state and alternatively, the anti-Stokes is a transition to a lower energy state[116].

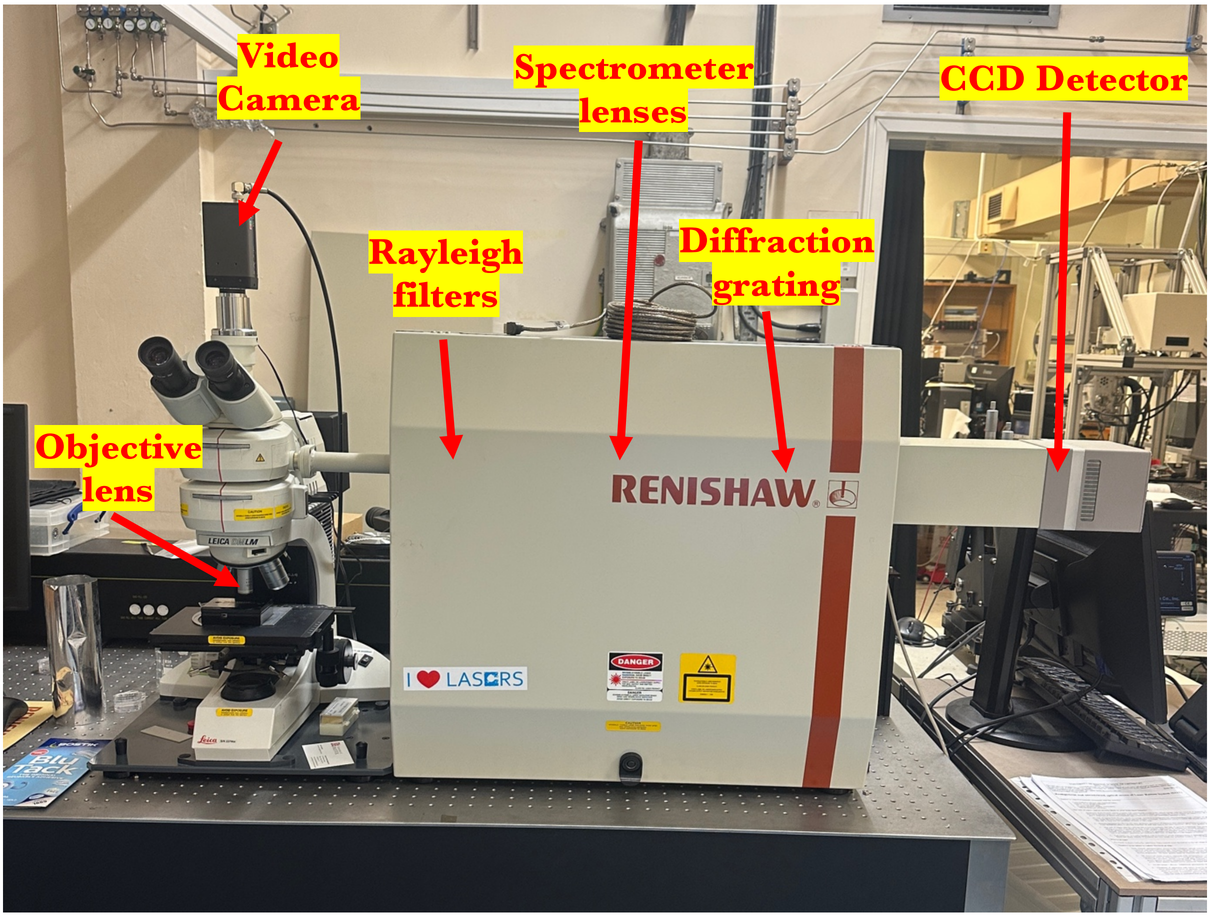

Figure 2.8 – Image of the Renishaw Ramascope 2000 Raman system, including labels for the position of key components within the system.

Considering the use of Raman spectroscopy in material identification, the main benefits associated with this technique include its non-destructive nature, fast analysis time and the intensity of spectral features being directly proportional to the particular species concentration, which can be useful in determining impurity or defect concentration within a sample.[117] Key Raman shifts include a sharp peak at 1332 cm^{-1} correlating to pure diamond, however, most diamond grown through CVD consist of diamond crystals surrounded by graphitic grain boundaries, producing additional signals within the spectrum, with the amount of additional shifts ultimately correlating to overall crystal quality. Regarding graphitic carbon, single crystal graphite produces a single peak at 1575 cm^{-1}, along with an additional feature around 1355 cm^{-1} in which the overall intensity of this peak increases and decreases relative to the amount of disorganised crystalline carbon within the sample.[118] Raman spectroscopy was carried out using a Renishaw Ramascope System 2000 pictured in *Figure 2.8*, operating at room temperature. An offcut of high purity single crystal diamond was used prior to new acquisitions to calibrate the instrument. Acquisitions were taken with 10 accumulations, at 2.00 s exposure time or with 5 accumulations and 10.00 s exposure time for extended range, using a green Ar^+ laser, with a laser excitation wavelength of 514.

2.2.2 - Scanning Electron Microscopy

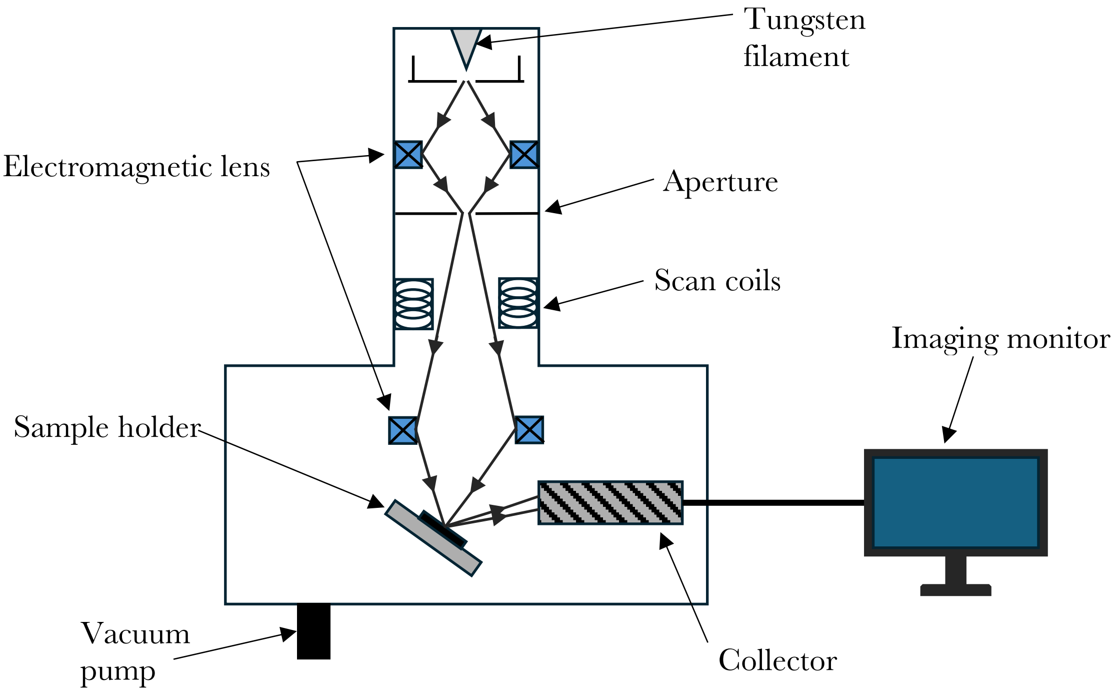

Figure 2.9 – Simplified schematic of a scanning electron microscopy device created with reference to [119].

Scanning electron microscopy (SEM) is a technique used to analyse the surface morphology of a sample with extremely high resolution. During operation, a finely focused beam of electrons is rastered across the surface of the target sample, with the chamber placed under a high vacuum. The reflected electrons are then collected and detailed images of surface characteristics are revealed.[120] All project related SEM analysis was performed using a JEOL IT300 scanning electron microscope, of which a simplified diagram can be found in *Figure 2.9*, generating a beam of electrons through thermionic emission by heating a tungsten filament. An applied voltage accelerates this primary electron beam which is focussed using electromagnetic lenses onto the sample. Finally, a combination of backscattered secondary electrons and some emitted secondary electrons are collected at a detector as a result of beam interaction with the top few nanometres of the surface, from which backscattered and emitted secondary electron intensity is measured and an image is formed.[121] The intensity is related to the surface topology of the sample, which can allow 2-dimensional images of the sample to be formed. Images of both the BDD growth and the etched cavity were taken, with magnifications ranging between 30x – 4000x. The primary beam energy was set to 15 kV, the working distance at 10.5 mm and the SEM was run in high vacuum mode. For non-conductive samples or samples which are unable to be coated with a conductive coating, low vacuum mode can be selected to reduce surface charging effects by introducing a controlled gas environment to neutralise the charge.[122]

2.2.3 – LEXT Laser Microscope

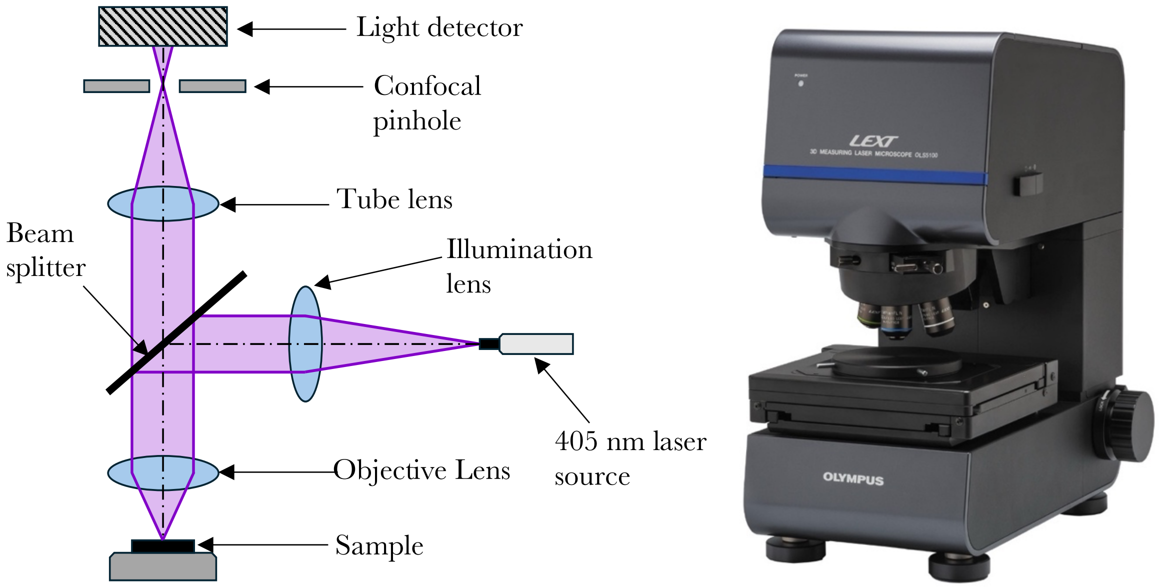

Figure 2.10 – A diagram showing the operation of a confocal laser microscope with a purple 405 nm laser (left) adapted from reference [124]. Alongside an image of the Olympus LEXT OLS5100 used for surface analysis taken (right) taken from reference [125].

Throughout the project, an Olympus LEXT OLS5100 3D measuring confocal laser microscope as shown in *Figure 2.10,* was used extensively to analyse both surface features and estimate the central membrane thickness throughout the laser etching process.[123] To analyse surface features both post-growth and post-laser etching, a 405 nm laser operating as expressed in *Figure 2.10* captured images and surface features varying zoom between 10x and 100x objectives, generating 3D acquisitions of surface characteristics and 2D surface profiles. For larger areas, stitching of multiple analysed areas allowed for more detailed analysis of the entire sample area. By setting manual height limits more accurate estimates of the sample height was able to be calculated from 3D acquisitions. From each 3D acquisition, a height profile could be generated in relation to the sample stage, with the average for each area (central membrane and outermost surface) taken and the height calculated in micrometres. From this, estimates for the etch rate of the laser could be made, however, etch rates were largely inconsistent. For similar projects, LEXT 3D laser microscopes are a very useful tool for fast and accurate analysis of both growths and structures, allowing for detailed, in-situ generation of clear images and height profiles of transmission dynode devices and other similar thin films.

2.2.4 - X-Ray Photoelectron Spectroscopy

X-ray photoelectron spectroscopy (XPS) is an analytical technique that was available to use as part of the University of Bristol NanoESCA system as shown in *Figure 2.11*. XPS was used to analyse the surface composition of the functionalised diamond transmission dynodes. Prior to XPS analysis the H-terminated (Sample 2) and O-terminated (Sample 4) dynodes were placed face down in 3 mm x 3 mm circular adaptor mounts, held by a slip plate and secured using a tungsten spring. The NanoESCA chamber was then pumped down to 6.00×10^{-7} mbar pressure and a subsequent 1 hour anneal at 300 ºC was performed to remove any surface adsorbates. Following the anneal, XPS analysis was performed on the H-terminated sample, using a Scienta Omicron XPS Argus multipurpose analyser, with an Al Kα monochromatic source (1486.7 eV) at a pass energy of 50 eV, positioned at an angle of 45º to the target sample. To offset surface charging a charge neutraliser of 20 μA was applied for each analytical run across both samples.

Scandium was then deposited onto Sample 4, using a scandium rod and an electron beam evaporator at room temperature. Deposition was ran for 30 minutes to achieve a 0.25 monolayer (ML) coverage. Following deposition, Sample 4 was annealed at 700 °C for 15 minutes, with the aid of a Ti^{4+} sublimation pump to resolve the outgassing of oxygen from the surface, as indicated by a large pressure jump from 1 x 10^{-8} mbar to 8 x 10^{-7} mbar. Following the successful anneal, XPS analysis was once again carried out on Sample 4, following the exact parameters as used for the H-terminated sample.

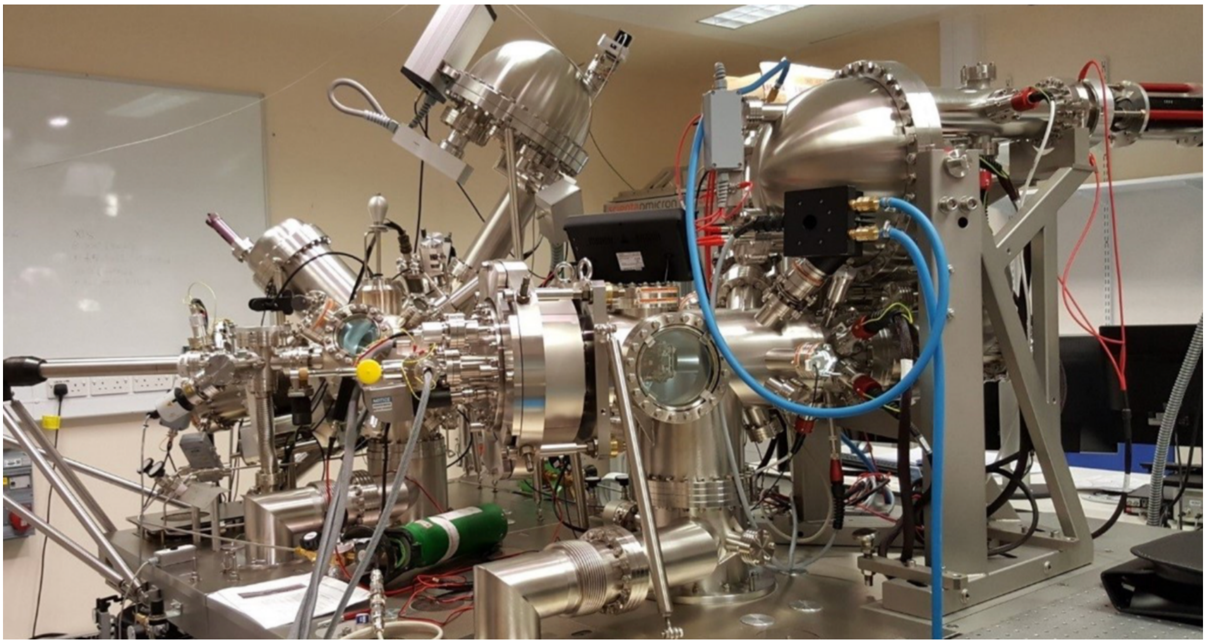

Figure 2.11 – An image of the University of Bristol NanoESCA facility used for XPS analysis and scandium deposition, taken from reference [126].

2.2.5 – Electron Beam Testing

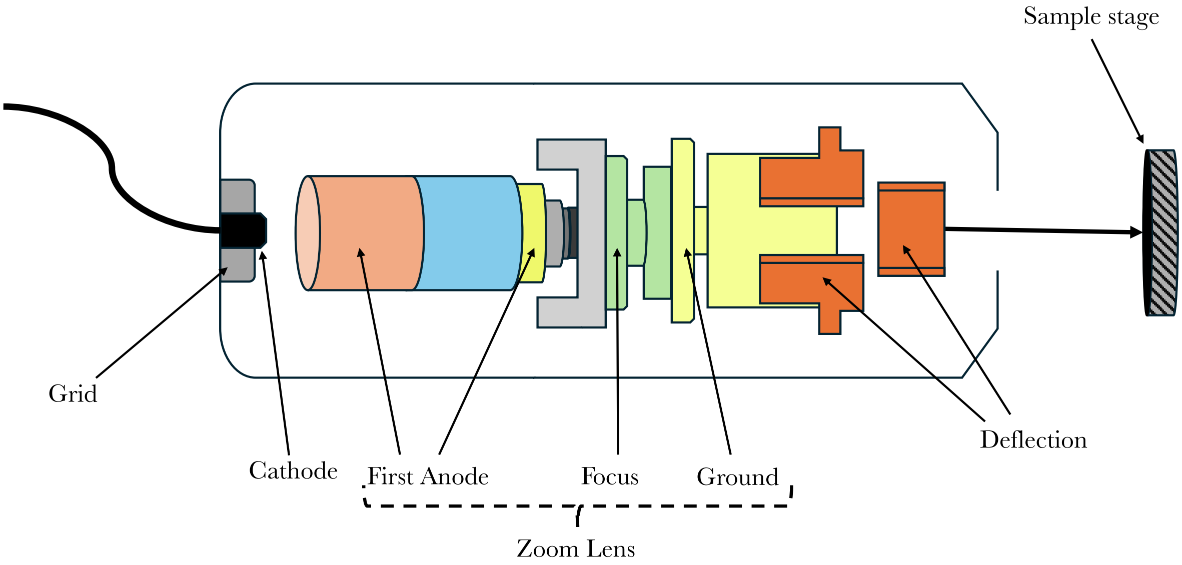

Figure 2.12 – A diagram showing the electron gun compartment of an e-beam. It should be noted that the whole system is closed and under vacuum. This diagram was created with reference to [127].

The transmission secondary electron emission properties of the finalised dynode structures were analysed under high vacuum conditions, maintaining a base pressure ~1.4 x 10^{-6} mbar, with Sample 4 (ScO-termination) mounted to the pre-fabricated transmission stand positioned above a current detector plate within a Faraday cup to minimise charge loss effects for more accurate determination of collected charge and optimisation of electron beam quality.[128], [129] A Kimble EGF-3104 electron gun powered by an EGPS-3104 power supply system was used as the primary electron source, of which a simplified diagram can be found in *Figure 2.12*. During operation, electrons are emitted from a tantalum cathode, with the ability to vary the beam energy (E_0 = 0–20 keV). To maintain consistency in between runs, the positioning of the dynode with reference to the charge collection plate remained constant (d = 3 mm) in which operation can be seen in *Figure 2.13*.

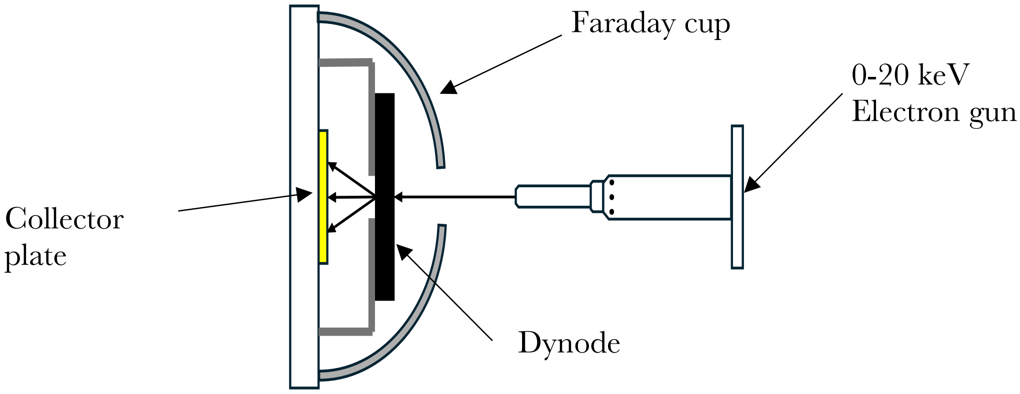

Figure 2.13 – A schematic of the electron beam in operation to study the TSEY of a diamond dynode, in which data is in relation to primary charge compared to charge arriving at the collector plate. This schematic was created with reference to [129].

For TSEY testing runs, the initial run tested with the addition of the transmission dynode, and this was followed by control testing without to calculate differences in current received. Across both runs operation parameters remained consistent, with beam energy set as $E_0 = 10$ keV, and an emission current $I_0 = 0.01$ mA. Similar to SEM operation, electron beam systems use electromagnetic lenses to focus the electron beam where the shape and strength of the magnetic field can be controlled by the voltage, which was set to 300 V during operation. The spot size at which electrons arrive at the sample is roughly determined and controlled by the ratio of the focus voltage to the 1st anode voltage, which was set to 500 V. Setting the focus and 1st anode voltage lens configuration in this way will maintain a relatively consistent spot size as beam energy is varied up or down.[127] To prevent potential cathode damage, a beam current limit of 1.7 mA was also set during each test run. A Keithley 6517A Electrometer/ High Resistance Meter was used in series to plot the collected current response I_s, in relation to emission current I_0, over an operation time of 10 minutes. From which comparing the current responses with and without the transmission dynode would allow for the estimation of transmission yield, and whether this indicated any charge multiplication effects.

3.0 – Results and Discussion

3.1 - Laser Micromachining of Thin Films

Although this aspect of the project falls neither under characterisation or performance based analysis, developing a laser micromachining technique to consistently fabricate robust thin films down to tens of microns thickness made up a reasonable proportion of the workload and therefore it is useful to report on the findings for future development of techniques, as an alternative viable pathway to generating potentially more robust thin films as opposed to using wet-etching of i-diamond growths on silicon wafers. Early attempts explored running high etch pass, low power etching in an attempt to have greater control over the film thickness, however, this was found to be as ineffective as it was time-consuming. Alternatively the running initial high power (~50%) runs was found to be effective in marking an initial graphitic central region. However, on successful runs which achieved final thicknesses around 30 μm - 50 μm it was determined that varying laser power between 20 – 30% achieved the best control without compromising etch rate. Tabulating data regarding material removed gives a clearer outline of future etching strategies that should be adopted, whilst also highlighting points in the process in which faults were most likely to occur, which in turn indicates the need for a reduced power during operation.

Table 3.1 – Summary of the membrane thicknesses for each transmission dynode sample 1-5, per etch pass with points highlighted to show membrane fracture or dynode completion.

Etch Pass	***Sample 1/ µm***	***Sample 2/ µm***	***Sample 3/ µm***	***Sample 4/ µm***	***Sample 5/ µm***
0	300.0	300.0	300.0	300.0	300.0
1	235.0	276.5	265.9	238.5	267.0
2	200.5	243.1	231.8	176.9	224.5
3	166.0	209.7	197.6	176.9	182.0
4	134.0	163.6	163.5	176.9	171.5
5	102.0	117.4	129.4	147.5	161.0
6	60.0	88.2	115.5	118.1	142.0
7	***Fracture***	58.9	101.7	90.0	123.0
8		46.0	86.5	62.0	120.0
9		***Complete***	71.2	49.1	117.0
10			***Fracture***	32.9	109.2
11				***Complete***	101.4
12					***Fracture***

Whilst *Table 3.1* shows no immediate trends in terms of points where samples fractured or where completion was determined, it is evident that when operating the laser power between 20 – 30%, care should be taken at the point of 8 etch passes when following a cross-hatched design. This can of course be further scaled to reflect the varying thickness of other substrates. Laser microscope observation identified the Sample 1 fracture to be a small crack, which was likely a result of mishandling of the sample during transfer within the lab, meaning this result can be discounted in reference to direct involvement of the laser. Focusing on the points prior to fracture on Sample 3 and 5, interestingly these points were thicker than at the final etch runs for the 2 completed samples. The likely cause of this was an increase in power. As opposed to the completed samples which greatly decreased the power to 17% on the last run to remove some graphitic carbon, Sample 3 and 5 both fractured when power was increased to 30% identifying a future need for care and patience at lower thicknesses. Average etch rates for Samples 1-5 were 39.3, 31.8, 25.4, 33.4 and 18.1 µm/pass respectively and whilst it is true that power was not varied consistently across all runs, these etch rates were generally inconsistent, in line with what would be expected for laser etching. However, as observed within similar ongoing experiments within the lab from a fellow student, wet etching of diamond grown on silicon substrates to isolate thin films led to both poor control of etching, frequent delamination and fracturing, proving it to be a more time-consuming and inconsistent method for thin film fabrication. Alternatively, experimental methods such as ICP RIE as previously mentioned, have been identified as probable solutions to this, etching in a far less destructive nature than laser etching.

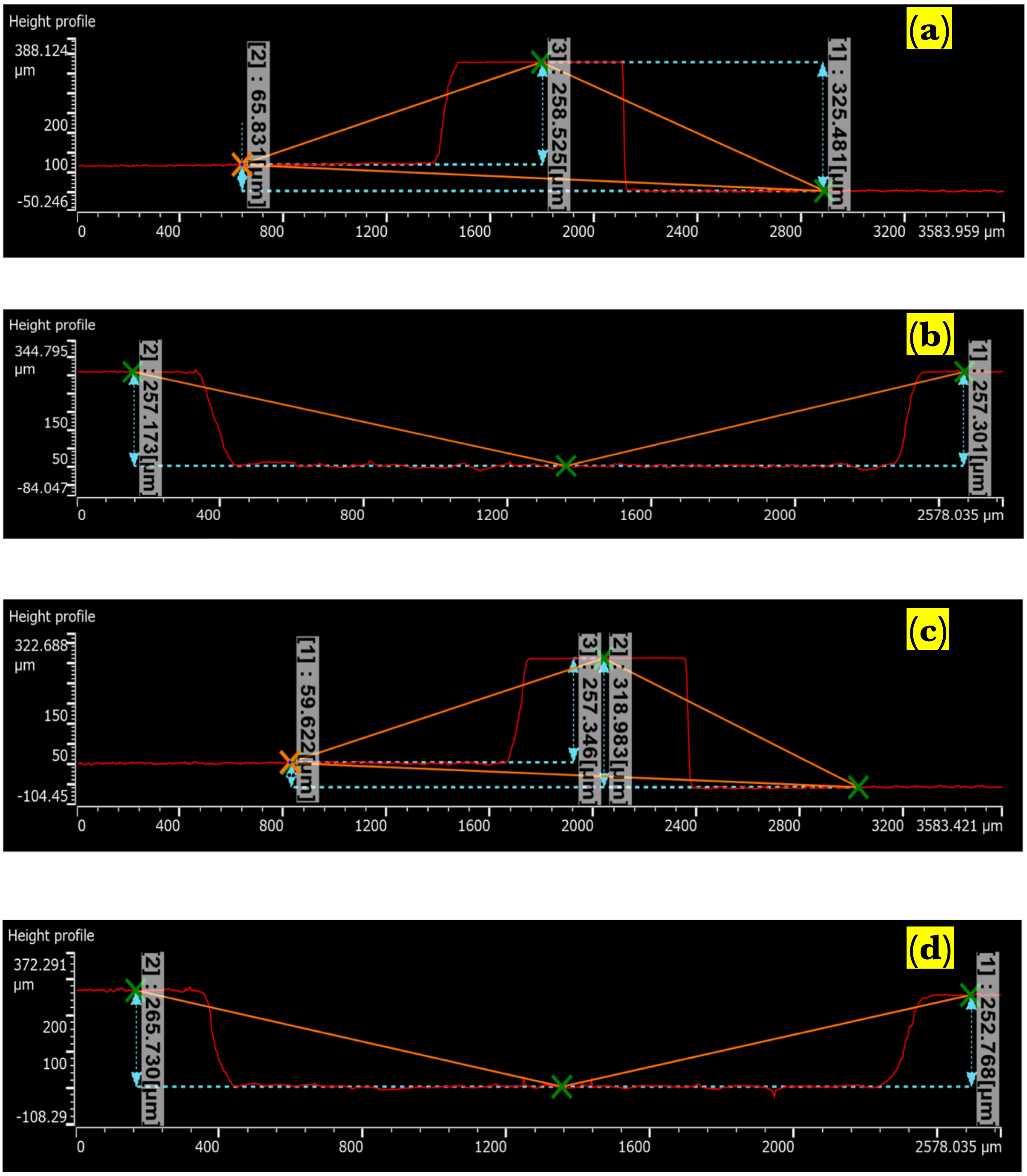

Figure 3.1 – LEXT profiles taken from both completed transmission samples showing (a) the final membrane thickness of Sample 2 (65.8 µm), taken in relation to the LEXT sample stage, (b) the well depth of Sample 2 which was analysed during etching, (c) the membrane thickness of Sample 4 (59.6 µm) in relation to the sample stage and (d) the well depth of Sample 4. All measurements were taken using the average of each surface to account for minor surface discrepancies.

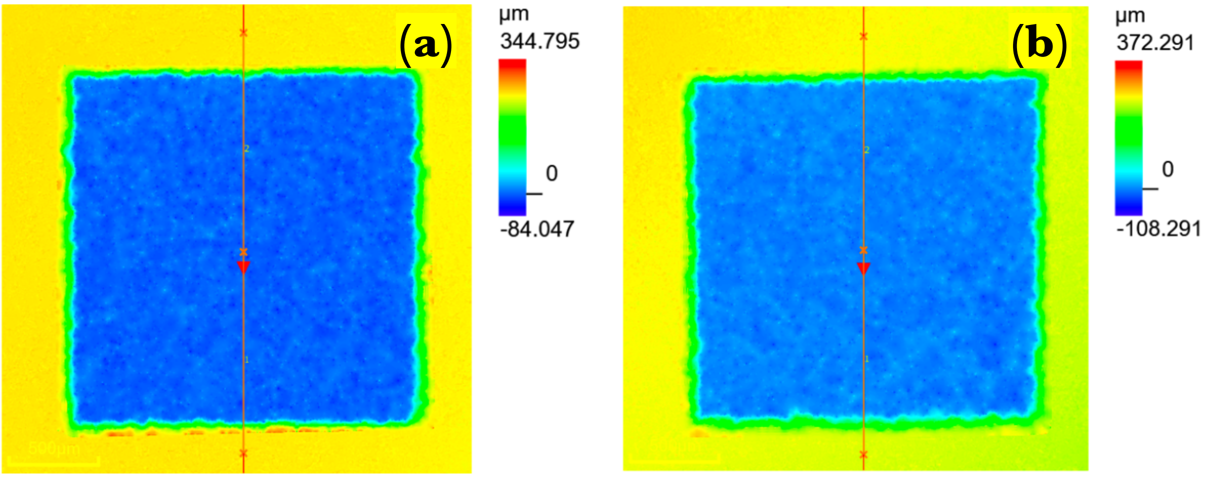

Figure 3.2 – Colour gradient height maps showing the smooth surfaces of (a) Sample 2 and (b) Sample 4 post laser etching. In reference to the scale (a) -84.047 is taken as the lowest point and (b) -108.291 is taken as the lowest point.

The above *Figure 3.1* shows the side profiles generated through 3D acquisition from the Olympus LEXT. These profiles represent the final profiles used to determine the thickness of each membrane post growth however, they were also used extensively throughout to provide fast and accurate surface analysis. *Figure 3.1* profiles were also used to monitor the surface roughness which was found to be relatively smooth with only a 1 – 5 μm discrepancy as a result of the cross-hatched etching pattern. This is better represented through *Figure 3.2* which further implies a smooth surface on the micron scale. The relation of surface roughness to secondary electron emission is well studied and will be discussed in further detail with the addition of SEM analysis, and imaging down to the nm scale. The yield of secondary electrons can be greatly reduced by the presence of rough surfaces, especially such that may arise from laser etching with the formation of deep valleys or irregularities, which can trap or backscatter escaping electrons preventing emission,[130] negatively impacting transmission dynode performance.

3.2 – SEM and LEXT Surface Analysis

A combination of scanning electron microscopy and LEXT laser microscopy was used to analyse a variety of important features within the dynode Sample 2 and Sample 4. This primarily included a focus on growth quality, film thickness as previously discussed, surface morphology and surface orientations present within PCD growths and etched substrates. For ease of understanding the dynode structure can be separated into two key surface components, comprising of the BDD growth side, in which electrons are initially received to begin transmission, and the etched ‘cavity’ side, where secondary electrons are emitted. To analyse the growth quality and the identification of any surface orientations of the initial, thicker growth SEM images can be found in *Figure 3.3*.

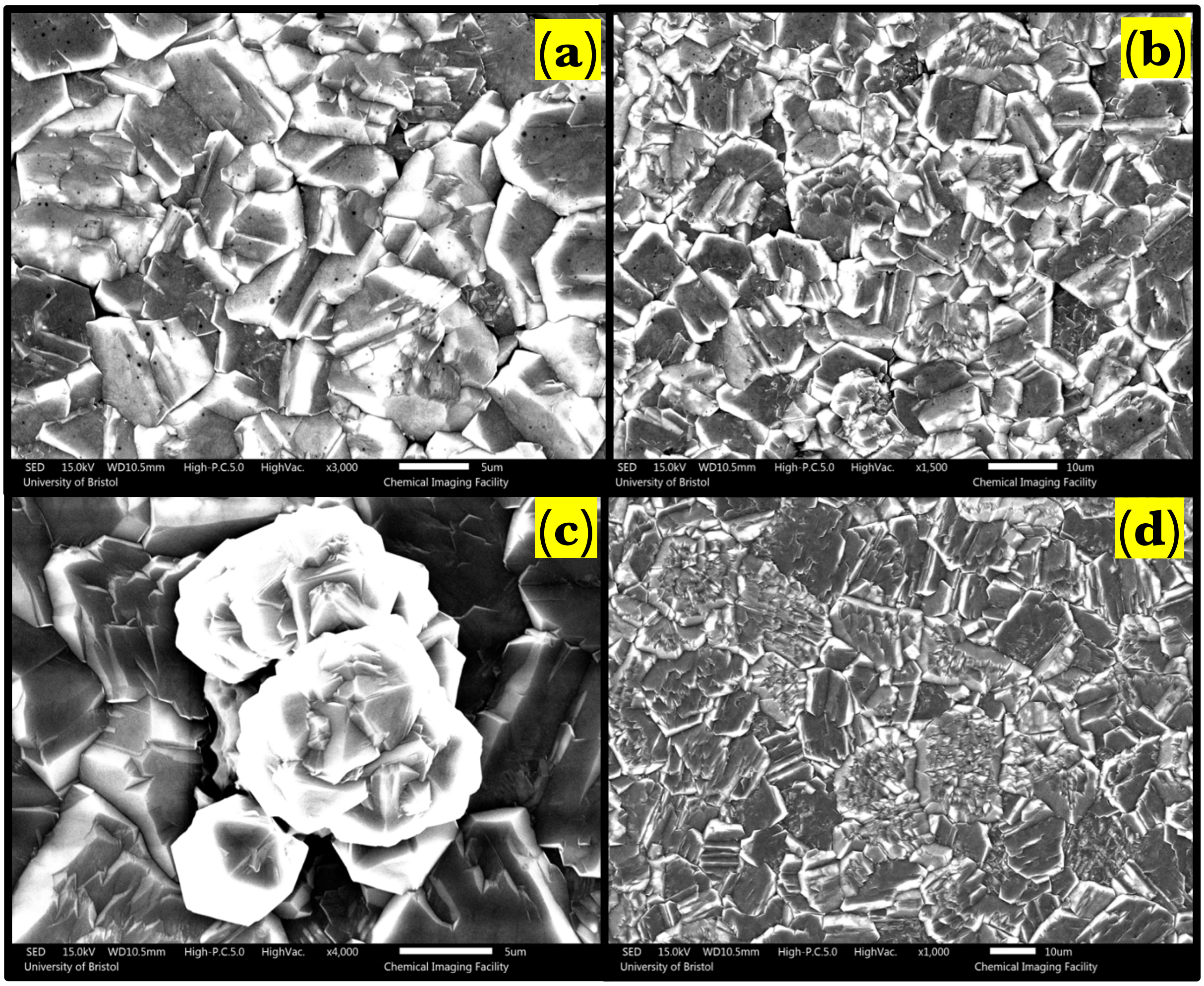

Figure 3.3 – SEM images of the initial low concentration MWCVD BDD growth; (a) Sample 2 high zoom, scale = 5 μm, (b) Sample 2 wider field, scale = 10 μm, (c) Sampe 4 high zoom, scale = 5 μm, (d) Sample 4 wider field, scale = 10 μm.

The growth quality of both samples can be best understood by looking at (a) and (c). The black speckles present within Sample 2 (a) were initially of interest and were consistent across the entire sample. This phenomenon is not widely reported with one report from R. Bogdanowicz *et al.,* reporting similar black spots as graphitic regions.[131] However, the uniform nature and far smaller size of the spots present within (a) and (b) implies that this is not the case and after discussion, it was determined this was likely trapped hydrogen. Once again it is difficult to comment with certainty the reason this arose, but it should be noted Sample 2 was the first ‘unassisted’ growth, with possible user error relating to unstable plasma, or general slow operation of the MFC gauges possibly being at fault. Whilst secondary ion mass spectrometry (SIMS) could have confirmed this, the extremely small concentration of hydrogen likely contained within these pockets would not significantly interfere with electrical conductivity in operation making this additional step unnecessary.

Comparing the crystal quality of Sample 2 (a) and (b) to Sample 4 (c) and (d), Sample 4 appears to be a slightly better growth, as evidenced by an overall clearer and more well-ordered crystal structure. Image sharpness within SEM is related directly to conductivity, in which Sample 4 appears sharper and better defined, which is supported when considering the slightly lower initial surface resistance of 13 MΩ. Whilst it would be sensible to assume this is due to the absence of trapped hydrogen within the crystal, there is not enough supporting evidence to draw this conclusion. Alternatively, surface orientations should be considered with a focus on their effects on the electrical conductivity of diamond. The lack of grain boundary order and high defect concentration within PCD, in comparison to high purity single crystal means that electrons can become trapped at grain boundaries within PCD impacting transmission of electrons through the bulk of the material.[132] This lack of order is also expressed within the diamond surface orientations that can be identified through SEM. Whilst both Sample 2 and Sample 4 express a high concentration of <110> surface orientations, Sample 4 has a greater presence of <111> crystal growths across the surface. For very low boron concentration, H-terminated diamond such as Sample 2 and Sample 4 at the time of SEM analysis, the <111> surface arrangements will accommodate a greater amount of field-induced free carriers than <110>, as a result increasing the conductivity, as observed with initial surface resistance tests.[133] The LEXT was used to carry out an analysis of the second HFCVD growth with the results shown in *Figure 3.4*.

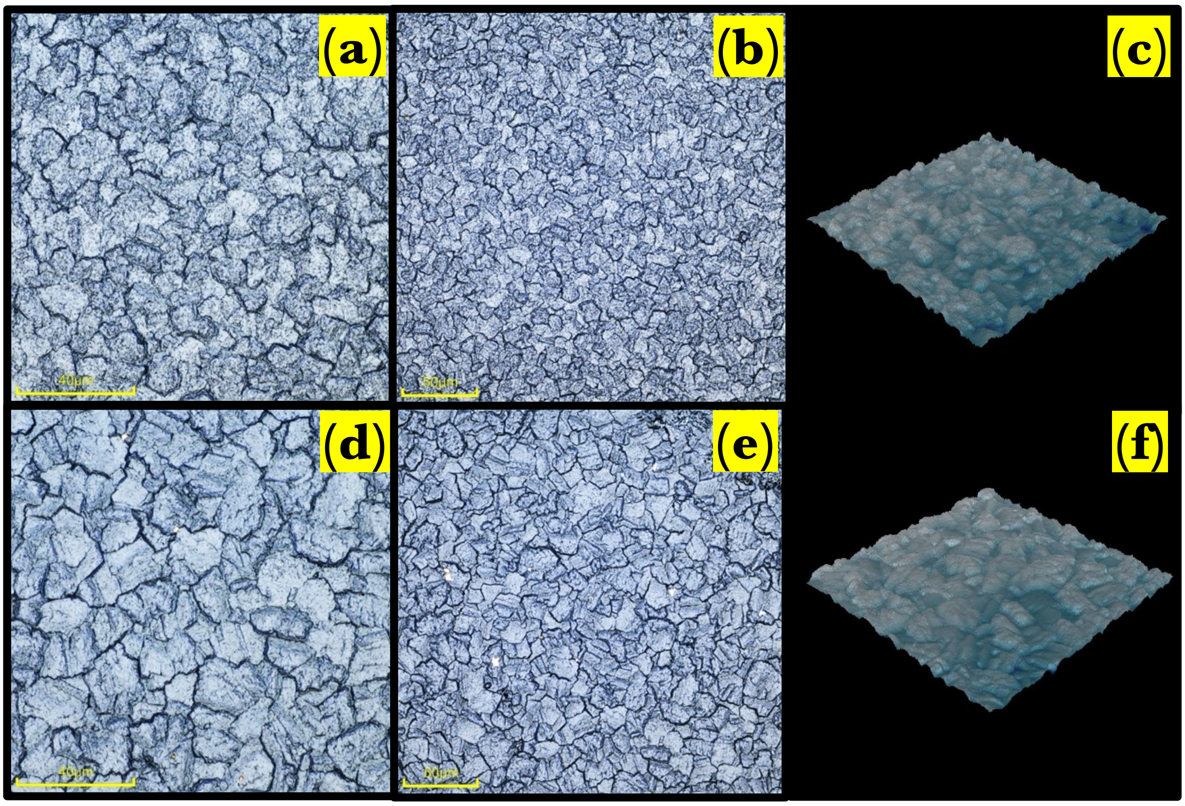

Figure 3.4 – LEXT images of high concentration HFCVD BDD growth; (a) Sample 2, 100x magnification, scale = 40 µm (b) Sample 2, 50x magnification, scale = 50 µm (c) Sample 2, 100x magnification 3D surface render, (d) Sample 4, 100x magnification, scale = 40 µm (e) Sample 4, 50x magnification, scale = 50 µm (f) Sample 4, 100x magnification 3D surface render.

The LEXT laser microscope was used post CVD growth to analyse the surface quality and morphology of Sample 2 and Sample 4 as seen in *Figure 3.4*. Comparing 100x and 50x magnifications of Sample 2 (a), (b) and Sample 4 (d), (e), the grains appear marginally larger in Sample 4. For electron emission properties, smaller grain boundaries are reported to produce a larger emission current over more uniform areas. However, this statement is largely in reference to a comparison between PCD and NCD, meaning emission current differences between the two samples would be minimal in this case.[134] Overall both growths appeared high quality, with the absence of graphitic regions later confirmed through the use of Raman spectroscopy. Electrical resistance was also observed to drop significantly (19 MΩ to 43 Ω for Sample 2 and 13 MΩ to 35 Ω in Sample 4) achieving the goal of increasing conductivity at the primary surface for electron transmission.

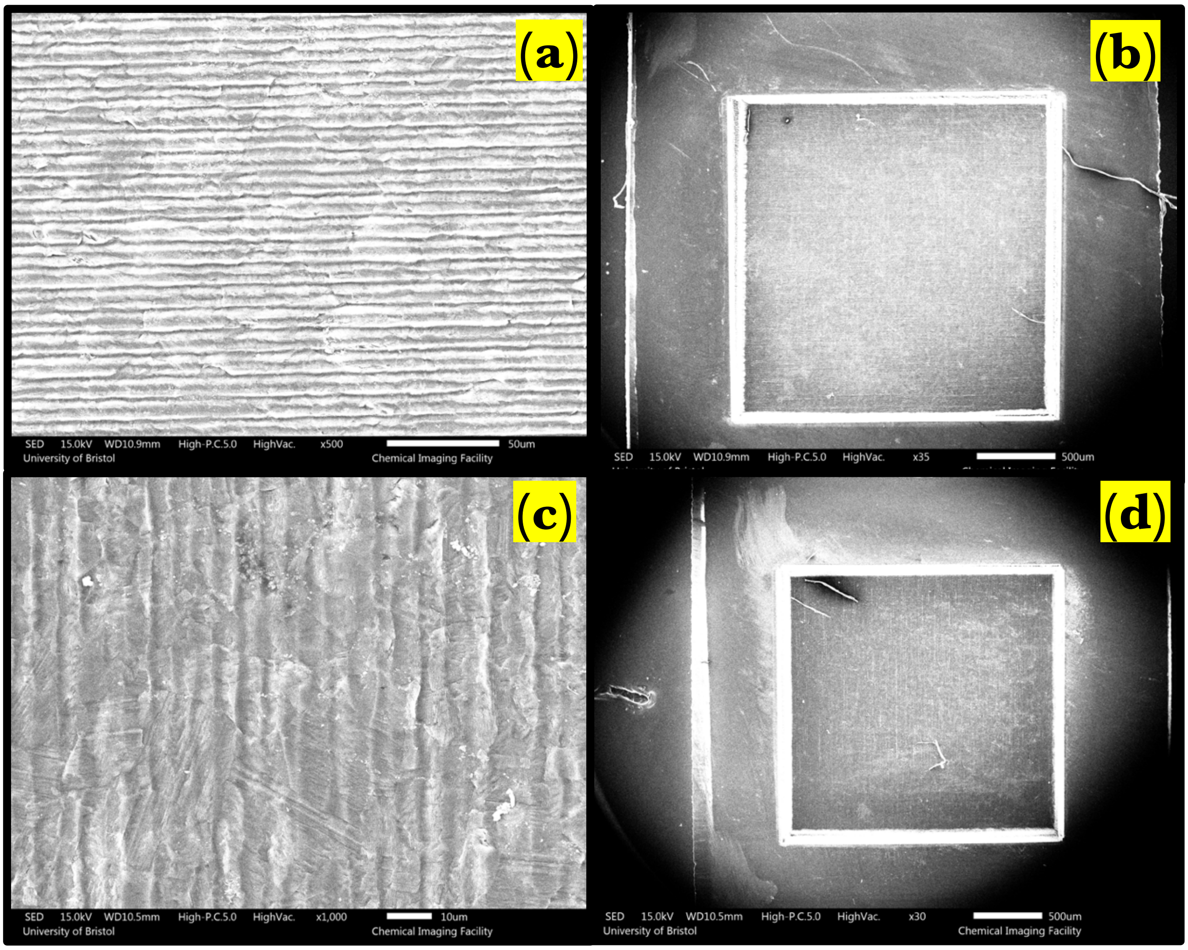

Figure 3.5 – SEM images showing the reverse etched side of Sample 2 and Sample 4; (a) Sample 2 high zoom, scale = 50 µm, (b) Sample 2 low zoom cavity, scale = 500 µm, (c) Sample 4 high zoom, scale = 10 µm, (d) Sample 4 low zoom cavity, scale = 500 µm.

SEM images shown in *Figure 3.5* of the entire cavity shown in (b) and (d) highlight the uniformity of the cross-hatched etching procedure. Of the two, (d) of Sample 4 appeared more consistent regarding the membrane edges which appear slightly offset in (b). (a) and (c) provide additional information regarding the smoothness of the membrane, in reference to grooves and troughs formed as a result of laser etching. The laser etching process flattens and removes a large majority of identifiable surface orientations as reflected in the high zoom SEM images, requiring the focus to be shifted towards potential recombination effects or electron scattering which may occur as a result of an uneven or rough surface, in reference to grooves. Overall (a) appears rougher with more prevalent lines remaining from the laser etching, and whilst there are visible grooves remaining on (c), these appear far less pronounced. This indicates that later etching processes, in particular where a greater total of etch passes alongside the addition of low power passes to towards the end, will aid in achieving a flatter and more consistent surface morphology. The benefit of obtaining a smooth surface lies in the reduced likelihood of obstruction or reabsorption from neighbouring crystals or irregularities, which in turn reduces the secondary electron emission yield.[135] The secondary electron emission yield properties of diamond films have also been found to be closely related to escape depth, λ_s, and when correlated with surface morphology, can determine both the roughness and crystal quality of diamond films, which can be controlled by varying the methane percentage during CVD.[136] Whilst exact methane concentrations used within Element Six PCD substrates is not publicly available, filed patents can be used to estimate this to be around 3.5 % (H_2/Ar/CH_4/SiH_4 in H_2 at 600/10/23/9.5 sccm),[137] which implies the SEY of the PCD substrate would sit between the 2 % and 4 % concentrations tested. From this, it is estimated that the substrate from which secondary electrons are emitted, operates towards to upper end of SEY as reported, which is beneficial for use within transmission dynode electron multiplication applications. However it is evident that this study would further benefit from the addition of a calculated escape depth to allow for modelling and optimisation of the SEY from PCD substrates, which could be achieved through further electron beam testing.

3.3 - Raman Spectrum

Raman spectra were taken for both the higher boron concentration growths and were used to analyse the surface characteristics and structural properties of boron-doped diamond. Alongside this, Raman spectrum was acquired for the PCD substrate, acting not only as a point of comparison between high purity industry standard PCD, but also to confirm the absence of any graphitic regions and the later presence of scandium within the membrane cavity. Unfortunately due to complications which arose with the bulb breaking in the Raman spectrometer, Raman analysis could not be carried out on initial, low concentration residual boron growth layers. Raman data taken from these initial growths would have been useful to compare the similarities between very low doping concentrations and i-diamond. Furthermore, the presence of peaks and Fano effect which arise due to a greater concentration of boron related defects would be clearer. However, such analysis was still attainable, and Raman spectrum obtained can be seen in *Figure 3.6*.

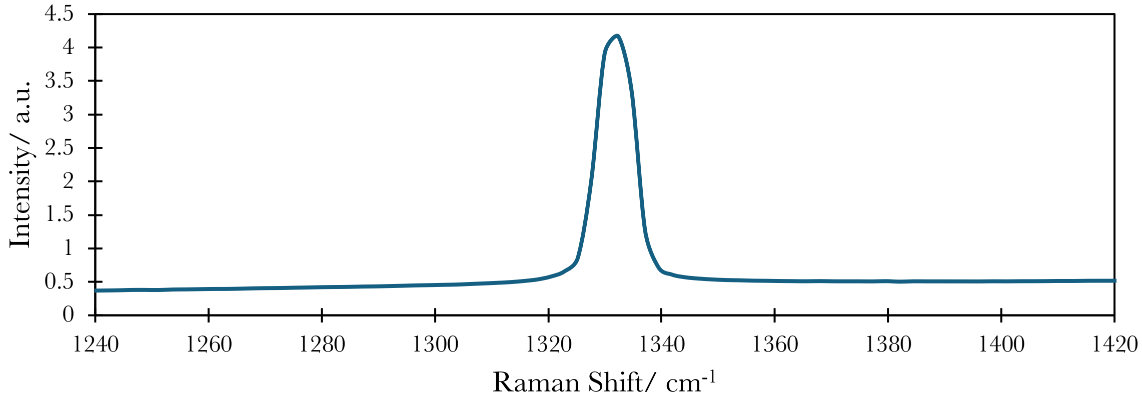

Figure 3.6 – Raman spectrum of the Element Six, polycrystalline diamond substrate of Sample 2 showing the key peak at 1332 cm^{-1}.

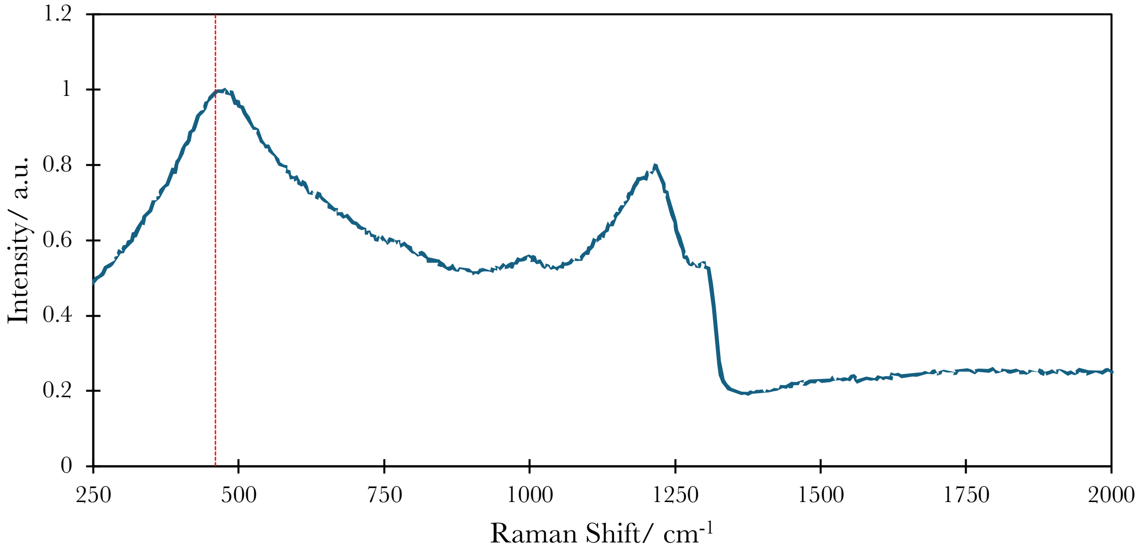

Figure 3.7 – Raman spectrum of the Sample 2 high concentration boron growth with the Lorentzian component, ω, represented by the red dashed line around ~465 cm^{-1}.

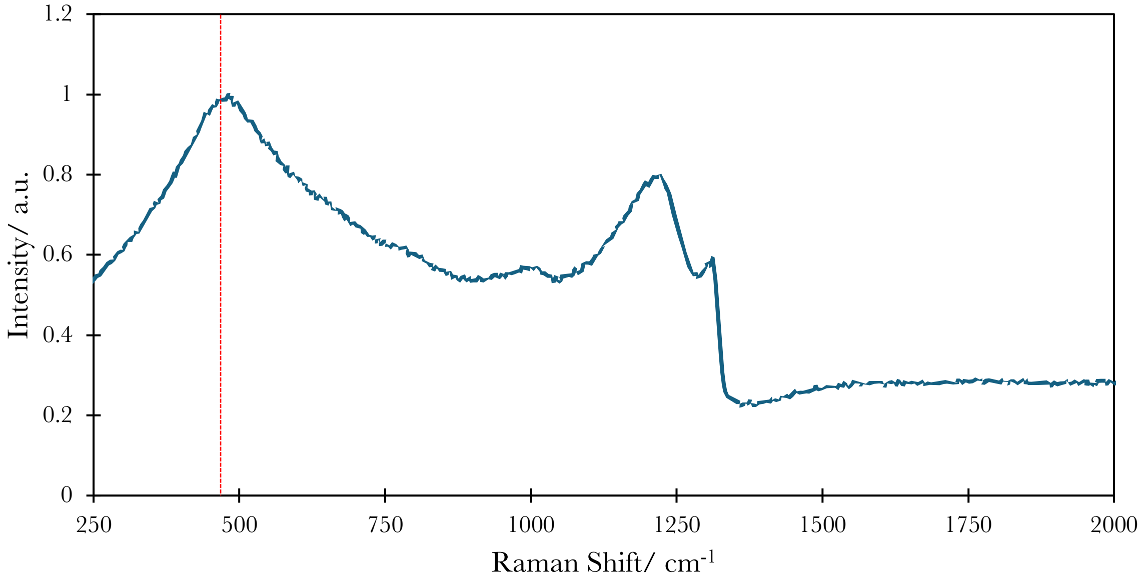

Figure 3.8 – Raman spectrum of the Sample 4 high concentration boron growth with the Lorentzian component, ω, represented by the red dashed line ~474 cm^{-1}.

A comparison between Sample 2 and Sample 4 was carried out with spectra shown in *Figure 3.7* and *Figure 3.8*. Key literature peaks which were expected included two broad bands ~480 cm^{-1} and ~1218 cm^{-1} alongside the addition of a Fano-shaped zone-centre phonon (ZCP) band before 1332 cm^{-1}.[138] The additional band ~500 cm^{-1} arises due to the vibrational modes of boron dimers within diamond which form at high boron doping concentrations.[138] The presence of all three key bands were identified in both cases, confirming the successful growth of BDD. Furthermore the absence of crystalline graphite bands ~1575 cm^{-1},[118] within both spectra implied hydrogen plasma treatment had been successful in removing surface graphite regions. The polycrystalline substrate spectra was also as expected, with one sharp band at 1332 cm^{-1}, further enforcing the success of hydrogen plasma treatment to remove graphitic carbon post laser etching.

It is clear from the *Figure 3.7* and *Figure 3.8* spectra, that both Sample 2 and Sample 4 had high quality growths, with well-defined characteristic Raman bands within the ~500 cm^{-1} and ~1200 cm^{-1} region. Comparing spectral features of the two growths it is difficult to assign one growth as distinctively better than the other. Both spectra feature broadened diamond primary density of state (PDoS) bands around 1200 cm^{-1},[138] implying that boron incorporation during the growth process was high within both samples. This broadening of the PDoS spectral band can be accredited to an increased concentration of boron related crystal defects, caused by higher dopant concentration, increasing the probability of inelastic scattering at characteristic frequencies. Considering boron incorporation into the crystal lattice for individual samples, *Equation 3* as expressed in a report by P. W. May *et* al., can be utilised to calculate estimations for boron concentration in heavily doped diamond, where ω is the Lorentzian component of the ~500 cm^{-1} band in wavenumbers, cm^{-1}.[139]

$$[B]/\,cm^{-3} = 8.44 \times 10^{30}\ \exp\left(-0.048\omega\right) \qquad \mathbf{(3)}$$

Computational modelling of the 450 – 550 cm^{-1} region of *Figure 3.7* and *Figure 3.8* estimated the respective Lorentzian components to be 465.0 cm^{-1} (Sample 2) and 473.7 (Sample 4) with the fitted curves expressed in *Figure 3.9* and *Figure 3.10*. From this [B] was estimated using *Equation 3* to be 1.71 x 10^{21} cm^{-1} (Sample 2) and 1.13 x 10^{21} cm^{-1} (Sample 4).[140] This slightly higher incorporation within Sample 2 is in line with what was discussed earlier regarding smaller grains present within the Sample 2 LEXT analysis, with a decrease in grain size correlating to an increase in B/C ratios.[141] Regarding the overall Fano effects, this is observable across both spectra through the asymmetry of the bands, especially within the ~1200 cm^{-1} region, indicating that both samples are approaching metallic-like conductivity.[142]

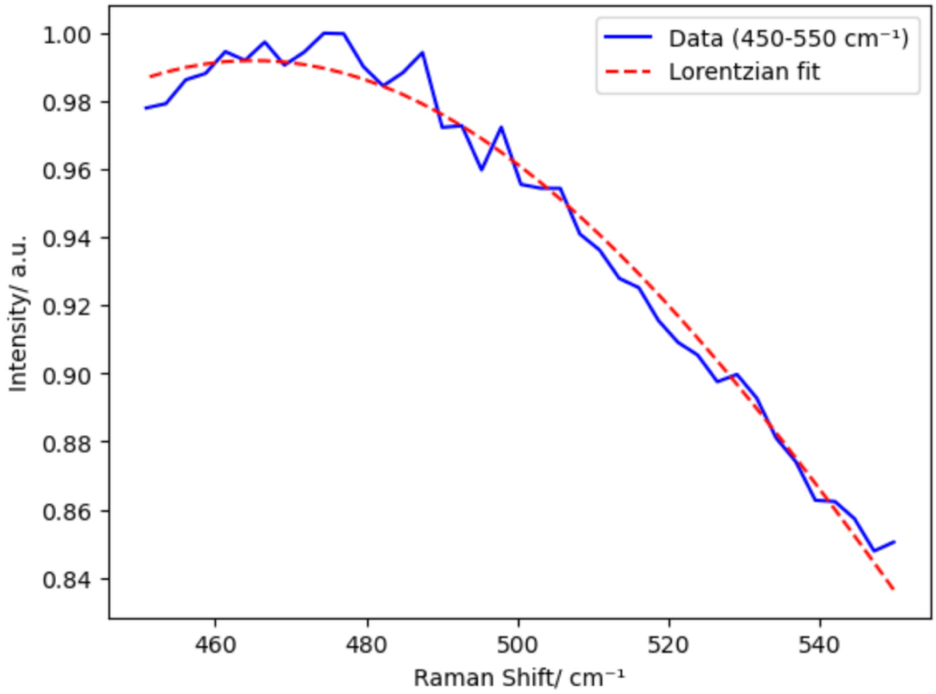

Figure 3.9 – Lorentzian fitted curve shown in red for H-terminated Sample 2, used to determine, ω, the Lorentzian component taken from peak centre = 465.0 cm^{-1} of the modelled curve over the 450 cm^{-1} – 550 cm^{-1} spectral region.

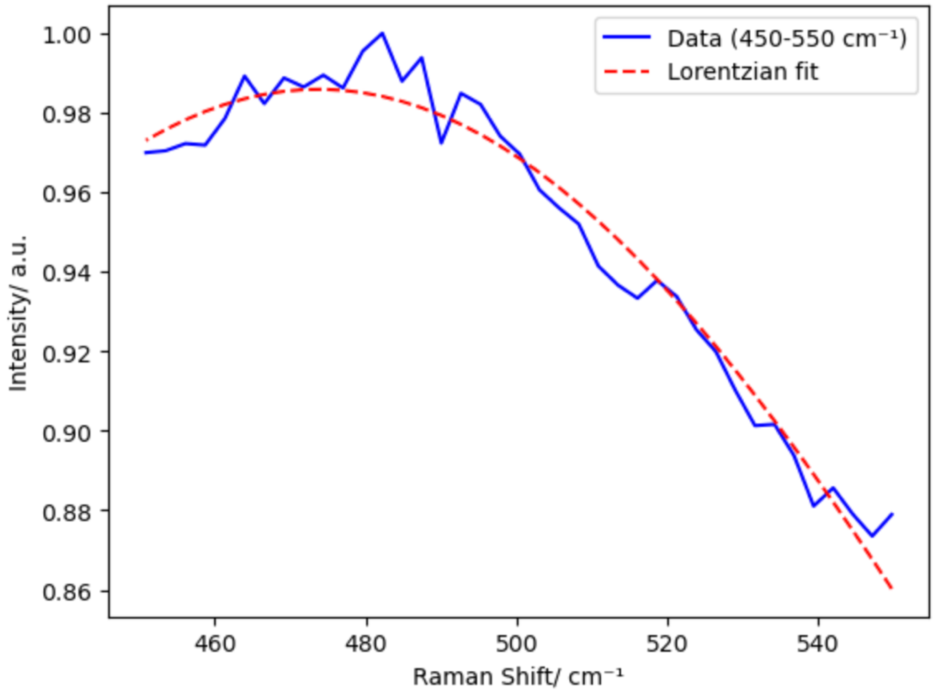

Figure 3.10 – Lorentzian fitted curve shown in red for ScO-terminated Sample 4, used to determine, ω, the Lorentzian component taken from peak centre = 473.7 cm^{-1} of the modelled curve over the 450 cm^{-1} – 550 cm^{-1} spectral region.

3.4 – X-Ray Photoelectron Spectroscopy

XPS was used to provide key analytical data relating to the functionalised membrane surface, in particular the three key stages of termination being the hydrogen, oxygen and scandium oxygen termination. The initial application of XPS focused on confirming the presence of H-termination on Sample 2 and O-termination on Sample 4. Due to surface charging experienced on both H-terminated and O-terminated surfaces and within the later scandium-oxygen functionalised surface, core electron binding energies were offset from literature values upon correction with the use of a charge neutraliser. Because of this, accurate calculations of the valence band energy level in reference to the fermi level were not possible. This would prevent the accurate calculation of exact electron affinity and work function values however this did not prevent the observation of shifts between positive and negative electron affinities with the application of oxygen and H-terminations respectively, and the subsequent switch from a positive to a negative electron affinity surface with the adsorption of scandium to the O-terminated surface.

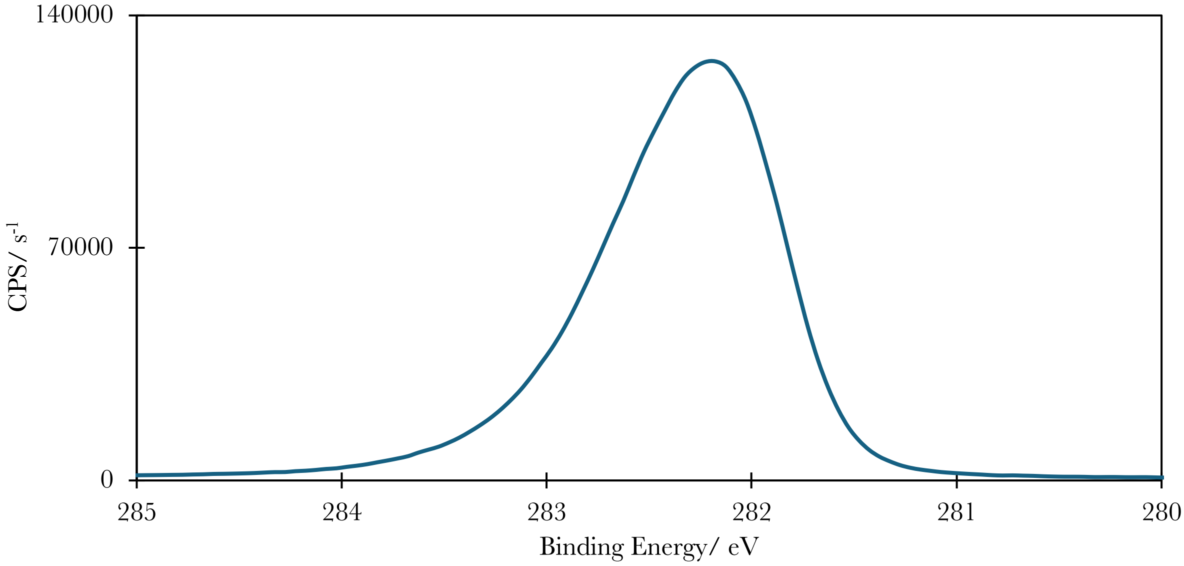

Figure 3.11 – C1s core electron binding energy peak for the H-terminated diamond surface of Sample 2 present at 282.2 eV used as a point of reference for XPS analysis using alternative O and ScO-terminations.

To observe the effects of varying electron affinity, the study focused primarily on core electron photoemission spectroscopy of C, O and Sc surface elements. Following the 15 minute, 300 °C anneal of the H-terminated Sample 2 and O-terminated Sample 4, spectra correlating to the C1s core electron energy level of carbon were generated as shown in *Figure 3.11*, at a binding energy of 282.2 eV correlating to bulk sp^3 hybridised surface carbon atoms. Due to surface charging this value was offset by 2.2 eV from typical literature reports of ~284.4 eV typically reported for clean, H-terminated diamond surfaces.[143] From the survey, the oxygen O1s region at ~531.0 eV was also analysed, from which no peak was observed, implying the use of an overnight vacuum and hydrogen plasma termination had been successful. This result could be further described as abnormally successful, as typically sample surfaces become partially oxygenated when exposed to air, especially in transit between labs. This implies to achieve such clean surfaces in future work, the time between H-termination and XPS analysis should be minimised to no more than 1 hour to prevent unwanted surface contamination.

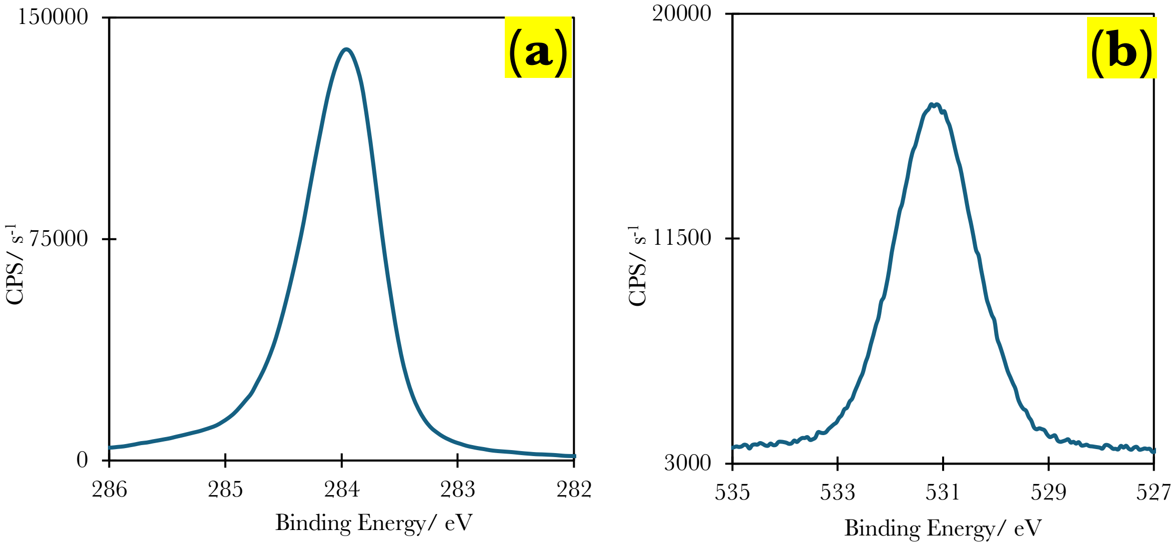

Figure 3.12 – XPS core electron spectra for Sample 4 oxygenated surface with (a) C1s core electron binding energy and (b) O1s core electron binding energy.

A full scan survey of the surface composition of the O-terminated sample identified the presence of two key peaks, correlating to the O1s and C1s core electron energy levels shown in *Figure 3.12*. Analysis initially focused on the prevalent O1s peak at 531.2 eV confirming the presence of an oxygenated surface. This was in very strong agreement with values previously reported for diamond surface carbon, C_d=O, formed from UV-ozone deposition.[56] A comparison between the oxygenated C1s peak and the hydrogenated C1s peak, observing a shift to a higher binding energy of 284.0 eV for sp^3 hybridised surface carbon, once again offset by 1.2 eV from previously reported values.[56] This shift to higher binding energy is in line with what is to be expected with the change of surface dipoles from positive to negative. With the change to negative $C_d^{\delta+}=O^{\delta-}$ dipoles, electron density is repelled onto the central carbon atom, increasing the effective nuclear charge, Z_{eff}, and in turn, increasing the binding energy to the core C1s electrons.

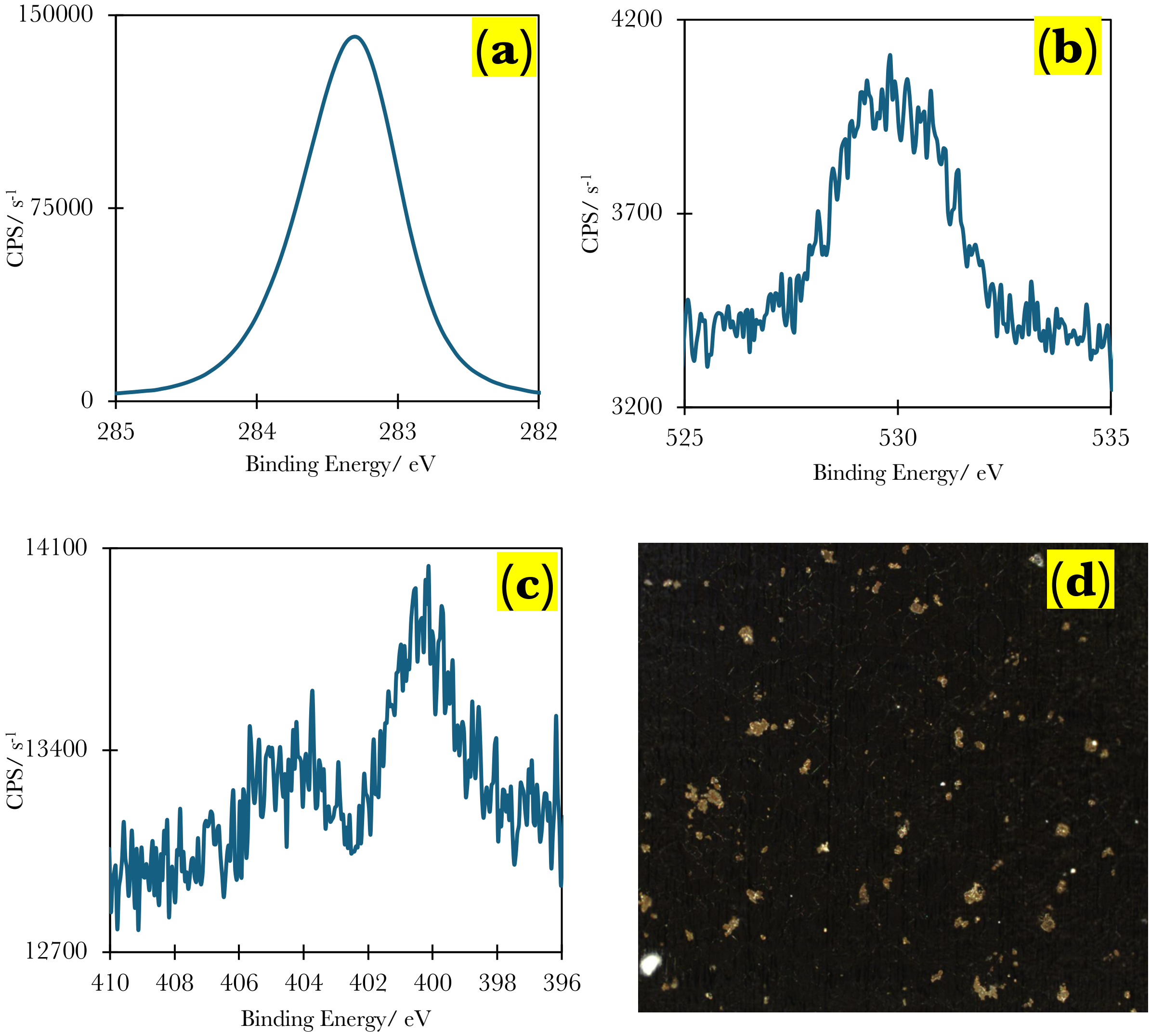

Figure 3.13 – XPS spectra for the ScO-terminated Sample 4 with (a) C1s core electron peak, (b) reduced O1s core electron peak, (c) Sc 2p$_{1/2}$ and 2p$_{3/2}$ core electron peaks and (d) low brightness LEXT surface image showing the presence of scandium metal on the surface.

Following the deposition of Scandium and the subsequent 700 °C anneal, final XPS analysis was carried out with results shown in *Figure 3.13*. The 700 °C anneal was performed in line with a report by R. Zulkharnay *et al.*,[64] which when annealing Sc-O-C_d functionalised surfaces over a range of 300 °C – 900 °C, 700 °C gave the highest activation of an NEA surface. The presence of scandium was detected through XPS analysis however the relative counts of both the Sc $2p_{3/2}$ and $2p_{1/2}$ peaks, alongside the counts of the O1s peak were very low. This was likely as a result of poor surface coverage of scandium onto the oxygenated surface due to the complex surface structure with the presence of steep vertical cavity walls and an additional outer surface, preventing a large majority of deposition onto the target central membrane. The low 0.25 ML of Sc used was also too low to counteract such complications, and future studies using similar device structures may look to use a greater monolayer coverage to ensure a more consistent overall scandium deposition. This was supported by the observation of outgassing of oxygen from the surface, resulting in a significant pressure rise within the NanoESCA chamber suggesting a portion of the oxygen remained unterminated. The two 2p core electron energy peaks observed for scandium appeared at 403.7 eV ($2p_{1/2}$) and 400.1 eV ($2p_{3/2}$), with the observed splitting as a result of spin-orbit coupling. Furthermore, the $2p_{3/2}$ exhibits a greater intensity due to greater degeneracy ($g = 4$) compared to $2p_{1/2}$ ($g = 2$). Finally, the presence of an NEA surface was confirmed with the observation of the switch to positive surface dipoles ($C_d^{\delta+}$- $O^{\delta-}$-$Sc^{\delta+}$) which draws electron density away from the central carbon atom, reducing Z_{eff} and therefore reducing the binding energy to the core C1s electrons. This observation was made through the comparison between the previously reported C1s binding energy peak of the C_d surface and the C1s binding energy peak of the C_d-Sc-O surface, in which binding energy was shifted to a lower 283.3 eV, confirming the presence of an NEA surface, crucial for secondary electron emission.

3.5 - Electron Beam Testing

Transmission dynode performance testing using the e-beam aimed to analyse potential transmission and electron multiplication characteristics of the dynode structures to determine where such a structure could be used within conventional MCP-PMT vacuum photodetectors. Unfortunately, complications which arose during the installation of the new electron gun component greatly hindered testing and only one test run was able to be performed. The device chosen for operation was the ScO-terminated Sample 4, as this aimed to achieve the aims of the project of improving dynode performance through metal-oxygen functionalisation of thin diamond membranes. The resultant current response over time graphs can be seen in *Figure 3.14 and Figure 3.15.*

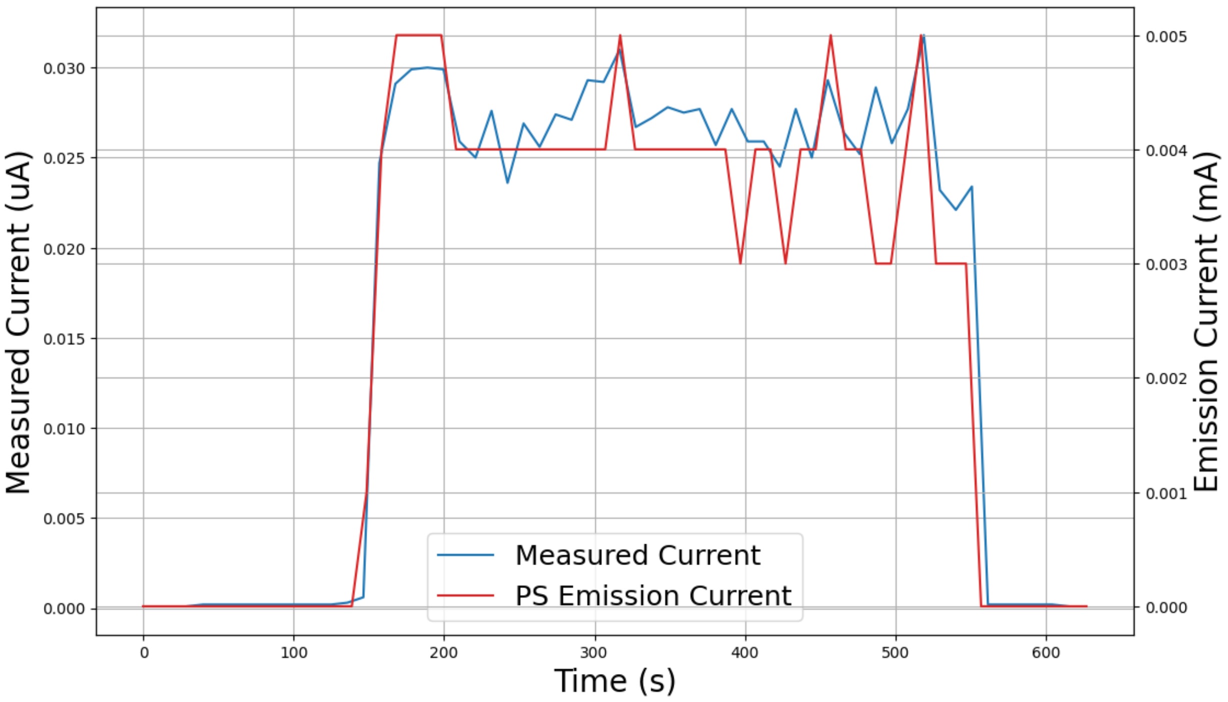

Figure 3.14 – Electron beam current over time response graph, correlating to the control run which operated without the inclusion of a transmission dynode to act as a baseline for current response, to be used in later comparison with a run including the use of the final transmission dynode structure.

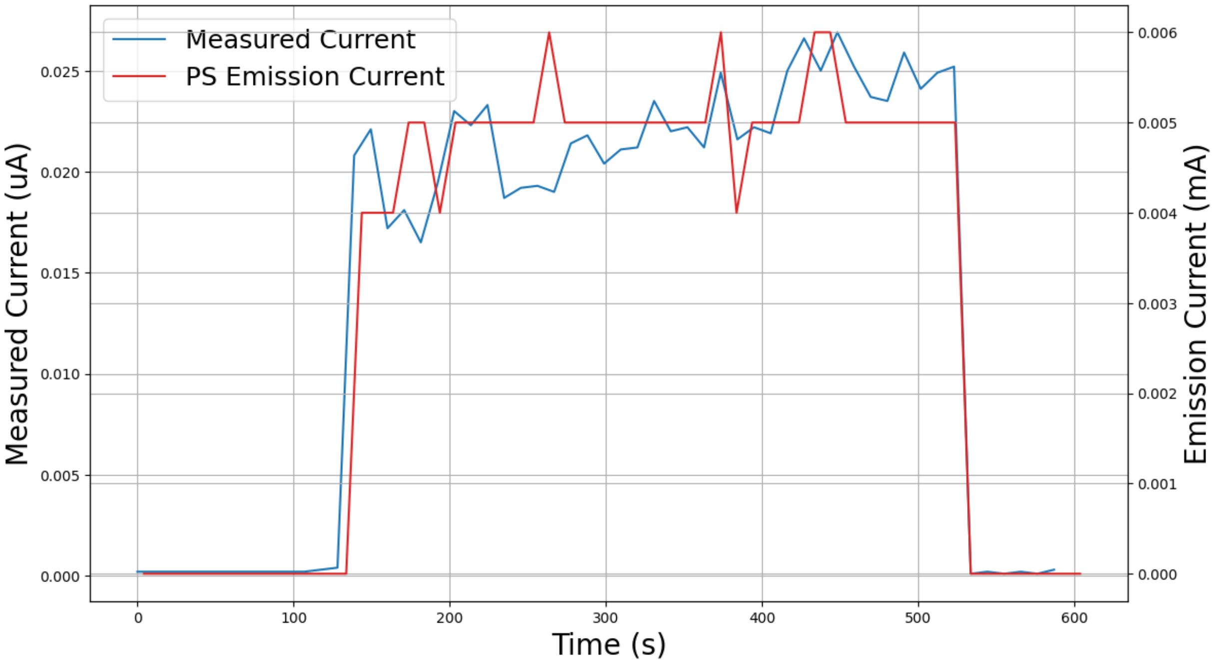

Figure 3.15 – Electron beam current over time response graph, operating with the inclusion of a transmission dynode to test the electron multiplication and transmission performance of the finalised transmission dynode structure.

From the current response graphs, values for minimum current, I_{min}, maximum current, I_{max}, and a baseline current from which the maximum and minimum values fluctuated, I_{base}, were calculated and tabulated in *Table 3.2*.

Table 3.2 – Measured current values for the control run and Sample 4 run. I_{min}, I_{base}, and I_{max} represent the minimum, maximum and baseline measured current for both runs. Current values were determined using physical copies of the two graphs and assigning a scale, X mm = 0.05 μA, from which estimates could be taken.

	I_{min}/ μA	I_{base}/ μA	I_{max}/ μA
Control	0.0192	0.0256	0.0320
Sample 4	0.0180	0.0225	0.0270

The current values, I_x, were normalised using *Equation 4,* which divided the measured secondary current, I_s, by the primary emission current, I_p to ensure that results were consistent and comparable to account for varying emission current.

$$I_x^* = \frac{I_s}{I_p} \qquad \textbf{(4)}$$

Table 3.3 – Normalised current values for the maximum, minimum and baseline measured current. In both cases the minimum emission current, $I_p = 0.003$ mA, the baseline $I_p = 0.004$ mA and the maximum $I_p = 0.005$ mA.

	I_{min}^*/ μA	I_{base}^*/ μA	I_{max}^*/ μA
Control	6.40×10^{-3}	6.40×10^{-3}	6.40×10^{-3}
Sample 4	4.50×10^{-3}	4.50×10^{-3}	4.50×10^{-3}

From the values quoted in *Table 3.3,* three values for the transmission secondary electron yield can be calculated using *Equation 5,* from which the TSEY, δ is calculated from the transmission dynode current, I_{TD}, over control current, I_{cont}. Results from these calculations are quoted in *Table 3.4*.

$$\delta = \frac{I_{TD}}{I_{cont}} \qquad \textbf{(5)}$$

Table 3.4 – TSEY values for transmission dynode Sample 4. Calculated using values included in *Table 4.2* using *Equation 5*.

	δ_{min}	δ_{max}	δ_{base}
TSEY of Dynode 4	0.703	0.703	0.703

From the values stated in *Table 3.4,* the TSEY was determined to be $\delta = 0.7$. What this implies is that for every one electron, on average 0.7 transmitted secondary electrons reach the collector plate. From this result we can draw two conclusions, the first being this device would be suitable and beneficial for applications in which the primary goal is to extend the lifetime of the photocathode. However for applications in which the primary goal is to improve device performance through an amplification of electrons arriving at the microchannel plate, this device would not be beneficial, but in the context of current techniques reducing collection efficiency by ~60 %, such results could be classified as an improvement of up to ~10 %. A previous report by X. Chang *et al.*, reported high transmission yields (~40) for 500 μm thick high purity single crystal diamond, excluded the use of polycrystalline diamond at 500 μm thicknesses for transmission applications due to electron and hole trapping at grain boundaries.[132] In reference to this, the results imply that the use of thinner PCD membranes would allow for transmission applications but the gain of electrons arriving at the detector would be impacted. Although these results are promising, a single test is not sufficient evidence to draw appropriate conclusions. The control and test currents are relatively similar in nature, which may imply the electron beam is providing false readings, which could be supported by the additional information that at the time of testing, a phosphor screen had not been used to correctly calibrate the instrument to be sure that the beam was focused directly on the dynode. Furthermore, the lack of repeat testing or comparisons with non-metal-oxygen functionalised devices means that we cannot validate our results *in situ*.

4.0 – Conclusion

Two complete transmission dynode structures were fabricated using a combination of laser etching to create initial thin PCD membranes, followed by the deposition of boron-doped diamond to form a conductive surface for primary electrons to begin transmission. The addition of a high boron doping concentration layer provided a solution to the initial growth having a high measured surface resistance when tested. The two structures were analysed using SEM and with a LEXT laser microscope, observing a high surface crystal quality and thin 66 μm and 60 μm membrane thicknesses. Raman spectroscopy and XPS to analysed surface composition, with Raman spectra identifying key bands ~480 cm^{-1} and ~1218 cm^{-1} alongside the additional Fano-shaped zone-centre phonon (ZCP) band before 1332 cm^{-1}. Raman spectra was also used to estimate boron incorporation to be 1.71 x 10^{21} cm^{-1} (Sample 2) and 1.13 x 10^{21} cm^{-1} (Sample 4).

H-termination of the samples was initially performed using a variable pressure and power hydrogen plasma treatment, with later oxygenation of the surface using UV-ozone cracking to form surface ketones. A similar use of hydrogen plasma was also used in between growths and etching processes to remove graphitic sp^2 surface carbon which may have formed, creating clean and high quality surfaces. Later functionalisation with scandium on the oxygenated surface of Sample 4 was carried out using the NanoESCA, which was followed by XPS analysis of the H-terminated and ScO-terminated surface, from which the C1s core electron binding energy peak of 282.2 eV for H-terminated PCD allowed for observations of the effects of NEA and PEA diamond surfaces. Such NEA surfaces are essential for secondary electron emission applications. However surface charging restricted further analysis through ultraviolet photoelectron spectroscopy (UPS) and photoemission electron microscopy (PEEM) which would have provided useful information regarding exact work function and electron affinity values. Solutions to this may include the use of commercially available boron-doped diamond substrates, which should be explored in future work.

This single run using the electron beam suggested the successful transmission of electrons through the sample ($\delta = 0.7$), alongside a slightly reduced gain in electrons through the generation of additional secondary electrons. However these results still suggested the device may hold use for the extension of the lifetime in MCP-PMT vacuum photomultipliers. Unfortunately, time restrictions and further complications with the electron beam meant that repeat testing or additional testing of Sample 2 which contained the additional ohmic channel were not possible. alongside this, the possibility of false results due to improper calibration or surface charging make it very difficult to validate these results. These results did show some promise however, and the project displayed that following similar steps it is possible to fabricate functionalised diamond transmission dynodes, but more work would be required to optimise the device fabrication process and validate or build upon results.

5.0 – Future Work

Future work would benefit from the use of a different, possibly larger starting substrate, whilst also exploring alternative techniques such as ICP RIE to form thin film transmission dynode substrates with improved control of the etch rate. This substrate should be single crystal following the report by X. Chang *et al.*,[132] regarding vastly increased secondary electron yields but crystal surface orientations should also be considered in line with what was reported by J. E. Yater *et al.*, when functionalising the surface.[39] Furthermore, a lightly boron-doped substrate would allow for further NanoESCA testing including UPS and PEEM by removing any potential surface charging, to give precise work function values and ultrahigh resolution of sample surfaces. In addition, scandium was the only metal explored for functionalisation of the oxygenated surface, leaving obvious room for alternative metal functionalisation using magnesium and lithium.

Further testing with the electron beam should also be carried out, not only to test for an increase in electron gain at the detector using optimised structures, but also to investigate how the functionalised surface would be maintained over repeated, high energy bombardment. This avenue of work would be crucial for determining whether such devices could be implemented into MCP-PMTs, as repeat testing could simulate extended periods of experimental use and outline the potential need to periodically re-terminate the surface to maintain high gain performance.

6.0 - References

1. T. Stachel, J. W. Harris, *Journal of Physics: Condensed Matter,* 2009, **21**, 364206.

2. K. Kanda, S. Takehana, S. Yoshida, R. Watanabe, S. Takano, H. Ando, F. Shimakura, *Surface and Coatings Technology,* 1995, **73**, 115-120.

3. D. Das, *Carbon-Based Nanofillers and Their Rubber Nanocomposites,* 2019, **1**, 123-181.

4. J. E. Graebner, L. S. Pan, D. R. Kania, *Diamond: Electronic Properties and Applications*, Springer Science & Business Media, New York, 2013.

5. T. Behnke, M. Doucet, N. Ghodbane, A. Imhof, C. Martínez, W. Zeuner, *Detectors and Associated Equipment*, 2002, **489**, 230-240.

6. E. H. Wahl, PhD Thesis, Stanford University, 2001.

7. C. J. H. Wort, R. S. Balmer, *Materials Today,* 2008, **11**, 22-28.

8. W. H. Bragg and W. L. Bragg, *Proceedings of the Royal Society of London. Series A, Containing Papers of a Mathematical and Physical Character*, 1913, **89**, 277-291.

9. M. E. Straumanis, E. Z. Aka, *Journal of the American Chemical Society*, 1951, **73**, 5521-5933.

10. C. Weigel, D. Peak, J. W. Corbett, G. D. Watkins and R. P. Messmer, *Physical Review B*, 1973, **8**, 2906-2915.

11. J. C. Charlier, X Gonze, J. P. Michenaud, *A Letters Journal Exploring The Fronteirs of Physics,* 1994, **28**, 403.

12. C. Brendel, PhD Thesis, Max Planck Instutute for the science of light, 2019.

13. L. Basso, M. Titze, J. Henshaw, P. Kehayias, R. Cong, M. S. Ziabari, T. Lu, M. P. Lilly, A. M. Mounce, *Giant*, 2024, **17**, 100238.

14. S. X. Tao, H. W. Chan, H. v. d. Graaf, *Materials (Basel),* 2016, **9**, 1017.

15. K. Nassau, J. Nassau, *Journal of Crystal Growth,* 1979, **46**, 157-172.

16. J. W. Yang, J. H. Park, M. G. Byun, J. Park, B. D. Yu, N. M. Hwang, *Diamond and Related Materials*, 2020, **107**, 107875.

17. S. S. Dossa, I. Ponomarev, B. N. Feigelson, M. Hainke, C. Kranert, J. Freidrich, J. J. Derby, *Journal of Crystal Growth,* 2023, **609**, 127150.

18. William G. Eversole, United States Patent Office, 750,309, 1961.

19. J. C. Angus, *Diamond and Related Materials,* 2014, **49**, 77-86.

20. B. V. Derjaguin, D. V. Fedoseev, V. M. Lukyanovich, B. V. Spitzin, V. A. Ryabov, A. V. Lavrentyev, *Journal of Crystak Growth*, 1968, **2**, 380-384.

21. B. V. Deryagin, B. V. Spitzin, L. L. Builov, A. A. Klochov, A. E. Gorodetskii, A, V. Smol'yanimov, *Dokl. Akad. Nauk. SSSR,* 1976, **231**, 333.

22. S. Mandal, *RSC Advances*, 2021, **11**, 10159-10182.

23. https://www.chm.bris.ac.uk/pt/diamond/growthmodel.htm (Accessed October 17th 2024).

24. P. W. May, *Philosophical transactions of the Royal Society A*, 2000, **358**, 473-495.

25. K. H. Lee, W. K. Seong, R. S. Ruoff, *Carbon*, 2022, **187**, 396-403.

26. M. Amaral, *Diamond-Based Materials for Biomedical Applications*, 2013, **1**, 48-70.

27. P. W. May, R. Zulkharnay, *Diamond thin films: a 21st century material: Part 2: a new hope.* Phil Trans R Soc Lond A, 2024.

28. J. A. Cuenca, S. Mandal, E. L. H. Thomas, O. A. Williams, *Diamond and Related Materials,* 2022, **124**, 108917.

29. V. Uwihoreye, Y. Hu, G. Cao, X. Zhang, F. E. Oropeza, K. H. L, Zhang, *Electron*, 2024, **2**, 70.

30. B. Lussem, M. Riede, K. Leo, *Physica status solidi (a)*, 2012, **1**, 9-43.

31. A. Rahman, *American Scientific Research Journal for Engineering, Technology and Sciences,* 2014, **7**, 50-70.

32. A. Zunger, O. I. Malyi, *Chemical Reviews*, 2021, **121**, 3031-3060.

33. J. G. Buijnsters, M. Tsigkourakos, T. Hantschel, F. O. V. Gomes, T. Nuytten, P. Favia, H. Bender, K. Arstila, J.-P. Celis and W. Vandervorst, *ACS Applied Materials & Interfaces*, 2016, **8**, 26381-26391.

34. D. Araujo, F. Lloret, G. Alba, M. P. Alegre, M. P. Villar, *Applied Physics Letters*, 2021, **118**, 052108.

35. W. Ahmed, C. A. Rego, R. Cherry, A. Afzal, N. Ali, I. U. Hassan, *Vacuum*, 2000, **56**, 153-158.

36. V. Damle, K. Wu, O. De Luca, N. Ortí-Casañ, N. Norouzi, A. Morita, J. de Vries, H. Kaper, I. S. Zuhorn, U. Eisel, D. E. P. Vanpoucke, P. Rudolf, R. Schirhagl, *Carbon*, 2020, **162**, 1-12.

37. F. G. Tseng, K. C. Chang, *Journal of Micromechanics and Microengineering*, 2003, **13**, 47.

38. M. S. Uddin, K. H. W. Seah, X. P. Li, M. Rahman, K. Liu, *Wear*, 2004, **257**, 751-759.

39. J. E. Yater, A. Shih, *Journal of Applied Physics*, 2000, **87**, 8103-8112.

40. R. J. Nemanich, L. Bergman, K. F. Turner, J. van der Weide and T. P. Humphreys, in *Wide-Band-Gap Semiconductors*, ed. C. G. Van de Walle, Elsevier, Amsterdam, 1993, 528-538.

41. T. L. Martin, PhD thesis, The University of Bristol, 2011.

42. Y. Zhang, Y. Lin, T. Duan, L. Song, *Materials Today*, 2021, **48**, 115-134.

43. L. Mosinska, P. Popielarski, K. Fabisiak, A. Dychalska, *Optical Materials,* 2020, **101,** 109676.

44. B. Rezek, C. Sauerer, C. E. Nebel, M. Stutzmann, J. Ristein, L. Ley, E. Snidero, P. Bergonzo, *Applied Physics Letters,* 2003, **82**, 1063.

45. J. H. Lay, K. M. O'Donnell, P. W. May, *Chemical Physics Letters,* 2011, **515**, 151-154.

46. W. Zheng, L. Jia, F. Huang, *iScience,* 2020, **23**, 101145.

47. T. I. Awan, A. Bashir, A. Tehseen and S. Bibi, in *Chemistry of Nanomaterials*, eds. T. I. Awan, A. Bashir and A. Tehseen, Elsevier, 2020, 179-206.

48. A. Shih, J. Yater, C. Hor, R. Abrams, *Applied Surface Science,* 1997, **111**, 251-258.

49. Secondary Electron Emission, https://www.physics-and-radio-electronics.com/electronic-devices-and-circuits/electron-emission/secondaryelectronemission.html , (accessed November 2024).

50. R. Vaz, P. W. May, N. A. Fox, C. J. Harwood, V. Chatterjee, J. A. Smith, C. J. Horsfield, J. S. Lapington, S. Osbourne, *Journal of* Instrumentation, 2015, **10**, 03004.

51. J. S. Lapington, P. W. May, N. A. Fox, J. Howarth, J. Milnes, https://www.chm.bris.ac.uk/pt/diamond/pdf/lfw2008.pdf , (accessed November 2024).

52. M. C. Salvadori, W. W. R. Araujo, F. S. Teixeira, M. Cattani, A. Pasquarelli, E. M. Oks, I. G. Brown, *Diamond and Related Materials,* 2010, **19**, 324-328.

53. H. Kawarada, *Surface Science Reports*, 1996, **26**, 205-206.

54. M. C. James, F. Fogarty, R. Zulkharnay, N. Fox, P. W. May, *Carbon*, 2021, **171**, 532-550.

55. K. M. O'Donnell, T. L. Martin, N. L. Allen, *Chemistry of Materials,* 2015, **27**, 1306-1315.

56. R. Zulkharnay, G. Zulpukarova, P. May, *Applied Surface Science,* 2024, **658**, 159776.

57. H. Kawarada, *Journal of Physics D: Applied Physics,* 2023, **56**, 053001.

58. S. Ullah, L. Cullingford, T. Zhang, J. R. Wong, G. Wan, M. Cattelan, N. Fox, *MRS Advances*, 2021, **6**, 311-320.

59. K. P. Loh, X. N. Xie, S. W. Yang, J. S. Pan, P. Wu, *Diamond and Related Materials,* 2002, **11,** 1379-1384.

60. R. Zulkharnay, P. W. May, *Journal of Materials Chemistry A*, 2023, **11**, 13432-13445.

61. R. Zulkharnay, N. L. Allen, P. W. May, *Carbon,* 2022, **196**, 176-185.

62. J. M. A. Beattie, J. P. Gross, M. J. Rayson, P. R. Briddon, *Diamond and Related Materials,* 2019, **94**, 137-145.

63. S. Ullah, G. Wan, C. Kouzios, C. Woodgate, Mattia Cattelan, N. Fox, *Applied Surface Science,* 2021, **559**, 149962.

64. R. Zulkharnay, N. A. Fox, P. W. May, *Small,* 2024, **20**, 2405408.

65. M. F. L'Annunziata, *Handbook of Radioactivity Analysis*, 2003, **2**, 845-987.

66. A. Lehmann, M. Böhm, D. Miehling, M. Pfaffinger, S. Stelter, F. Uhlig, A. Ali, A. Belias, R. Dzhygadlo, A. Gerhardt, M. Krebs, D. Lehmann, K. Peters, G. Schepers, C. Schwarz, J. Schwiening, M. Traxler, L. Schmitt, M. Düren, E. Etzelmüller, K. Föhl, A. Hayrapetyan, K. Kreutzfeld, J. Rieke, M. Schmidt, T. Wasem, C. Sfienti, *Nuclear Instruments and Methods in Physics Research Section A: Accelerators, Spectrometers, Detectors and Associated Equipment,* 2020, **958**, 162357.

67. L. Chen, H. Yang, X. Wang, L. Tian, D. Ding, Y. Wang, K. Ji, P. Xiang, T. Luo, C. She, *Scientific Reports,* 2023, **13**, 20436.

68. K. Smith, *Methods in Experimental Physics,* 1995, **29**, 253-272.

69. J. Taewon, S. Yu, J. Lee, *Journal of Vacuum science& Technology B Microelectronics Processing and Phenomena,* 2001, **19**, 2247-2251.

70. J. Kloprogge, B. Wood, *Handbook of Mineral Spectroscopy,* Elsevier, 1, 2021, Introduction, xiii-xxv.

71. P.R. Bolton, M. Borghesi, C. Brenner, D.C. Carroll, C. De Martinis, F. Fiorini, A. Flacco, V. Floquet, J. Fuchs, P. Gallegos, D. Giove, J.S. Green, S. Green, B. Jones, D. Kirby, P. McKenna, D. Neely, F. Nuesslin, R. Prasad, S. Reinhardt, M. Roth, U. Schramm, G.G. Scott, S. Ter-Avetisyan, M. Tolley, G. Turchetti, J.J. Wilkens, *Physica Medica,* 2014, **30**, 255-270.

72. V. V. Anashin, P. M. Beschastnov, V. B. Golubev, L. A. Mironenko, A. A. Salnikov, S. I. Serednyakov, *Nuclear Instruments and Methods in Physics Research A*, 1995, **357**, 103-109.

73. A. Lehmann, M. Bohm, M. J. Gotz, K. Gumbert, S. Krauss, D. Miehling, M. Pfaffinger, *Nuclear Instruments and Methods in Physics Research Section A: Accelerators, Spectrometers, Detectors and Associated Equipment*, 2024, **1065**, 169536.

74. C. Lv, W. Zhang, L. You, P. Hu, H. Wang, H. Li, C. Zhang, J. Huang, Y. Wang, X. Yang, Z. Wang, X. Xie, *AIP Advances*, 2018, **8**, 105018.

75. O. H. W. Siegmund, *Vacuum Ultraviolet Spectroscopy,* 1999, **2**, 139-175.

76. A. S. Tremsin, J. V. Vallerga, *Radiation Measurements*, 2020, **130**, 106228.

77. M. Calvi, S. Capelli, P. Carniti, C. Gotti, G. Pessina, *Jounral of Instrumentation,* 2020, **15**, 10031.

78. L. Ma, L. Chen, P. Chai, Z.Liang, G. Huang, J. Hu, X. Han, Z. Hua, X. Huang, M. Jin, X. Jiang, Z. Jin, S. Liu, W. Pan, S. Qian, L. Ren, S. Si, J. Sun, L. Wei, Q. Wu, T. Wang, X. Wang, Y. Wang, Y. Wang, Z.Wang, Z. Wang, N. Wang, K. Wu, X. Yan, H. Zhang, Z. Zhang, *Nuclear Instruments and Methods in Physics Research Section A; Accelerators, Spectrometers, Detectors and Associated Equipment*, 2023, **1049**, 168089.

79. Time-Correlated Single Photon Counting, https://www.picoquant.com/images/uploads/page/files/7253/technote_tcspc.pdf (accessed February 2025).

80. J.H. Eberly, P.W. Milonni, *Encyclopaedia of Physical Science and Technology*, 2003, **3**, 409-439.

81. T. Itoh, *Chemical Reviews,* 2012, **112**, 4541-4568.

82. G. Baryshnikov, B. Minaev, H. Agren, *Chemical Reviews,* 2017, **117**, 6500-6537.

83. M. Eck, PhD Thesis, The University of Freiburg, 2014.

84. E. P. Cherenkova, *Nuclear Instruments and Methods in Physics Research Section A: Accelerators, Spectrometers, Detectors and Associated Equpiment,* 2008, **595**, 8-11.

85. M. F. L'Annunziata, *Handbook of Radioactivity Analysis,* 2007, **2**, 719-797.

86. S. P. Denisov, *Physics-Uspekhi,* 2015, **58**, 480-485.

87. MCP-PMT, https://www.exosens.com/products/mcp-pmt , (accessed April 2025).

88. J. Vallerga, J. Zaninovich, B. Welsh, O. Siegmund, J. McPhate, J. Hull, G. Gaines, D. Buzasi, *Nucelar Instruments and Methods in Physics Research Section A: Accelerators, Spectrometers, Detectors and Associated Equipment,* 2002, **477,** 551-555.

89. H. Tomio, G. Yang, W. Lu, X. Xu, D. Orlov, E. Kernen, R. Glazenbourg, presented in part at CLEO Conference and Exhibition, San Jose, May, 2023.

90. Z. Shareefdeen, H. Al-Najjar, *ACS Omega*, 2024, **9**, 5127-5141.

91. A. Lehmann, A. Britting, W. Eyrich, M. Pfaffinger, F. Uhlig, A. Belias, R. Dzhygadlo, A. Gerhardt, K. Götzen, G. Kalicy, M. Krebs, D. Lehmann, F. Nerling, M. Patsyuk, K. Peters, G. Schepers, L. Schmitt, C. Schwarz, J. Schwiening, M. Traxler, M. Zühlsdorf, M. Düren, E. Etzelmüller, K. Föhl, A. Hayrapetyan, B. Kröck, O. Merle, J. Rieke, M. Schmidt, E. Cowie, T. Keri, P. Achenbach, M. Cardinali, M. Hoek, W. Lauth, S. Schlimme, C. Sfienti, M. Thiel, *Journal of Instrumentation,* 2016, **11**, C05009.

92. N. Kishimoto, M. Nagamine, K. Inami, Y. Enari, T. Ohshima, *Nuclear Intruments and Methods in Physics Research A,* 2006, **564,** 204-211.

93. C. P. Uzunoğlu, Y. Babacan, F. Kaçar, M. Ugur, *Electric Power Components and Systems,* 2020, **48**, 138-147.

94. M. Kristiansen and J. Dickens, in *Encyclopedia of Physical Science and Technology (Third Edition)*, ed. R. A. Meyers, Academic Press, New York, 2003, 277-285.

95. Visualisation of a Townsend Avalanche, Wikipedia Commons, https://commons.wikimedia.org/wiki/File:Electron_avalanche.gif (accessed January 2025).

96. D. Chitnis, N. T. Kalyani, H. C. Swart, S. J. Dhoble, Renewable and Sustainable Energy Reviews, 2016, **64**, 727-748.

97. A. Lehmann, M. Böhm, W. Eyrich, D. Miehling, M. Pfaffinger, S. Stelter, F. Uhlig, A. Ali, A. Belias, R. Dzhygadlo, A. Gerhardt, K. Götzen, G. Kalicy, M. Krebs, D. Lehmann, F. Nerling, M. Patsyuk, K. Peters, G. Schepers, L. Schmitt, C. Schwarz, J. Schwiening, M. Traxler, M. Düren, E. Etzelmüller, K. Föhl, A. Hayrapetyan, K. Kreutzfeld, O. Merle, J. Rieke, M. Schmidt, T. Wasem, P. Achenbach, M. Cardinali, M. Hoek, W. Lauth, S. Schlimme, C. Sfienti, M. Thiel, *Journal of Instrumentation,* 2018, **13**, C02010.

98. T. Jinno, T. Mori, T. Ohshima, Y. Arita, K. Inami, T. Ihara, H. Nishizawa, T. Sasaki, *Nuclear Instruments and Methods in Physics Reseach Section A: Accelerators, Spectrometers, Detectors and Associated Equipment,* 2011, **629,** 111-117.

99. A. Lehmann, A. Britting, W. Eyrich, M. Pfaffinger, F. Uhlig, A. Belias, R. Dzhygadlo, A. Gerhardt, K. Götzen, G. Kalicy, M. Krebs, D. Lehmann, F. Nerling, M. Patsyuk, K. Peters, G. Schepers, L. Schmitt, C. Schwarz, J. Schwiening, M. Traxler, M. Zühlsdorf, M. Düren, E. Etzelmüller, K. Föhl, A. Hayrapetyan, B. Kröck, O. Merle, J. Rieke, M. Schmidt, E. Cowie, T. Keri, P. Achenbach, M. Cardinali, M. Hoek, W. Lauth, S. Schlimme, C. Sfienti, M. Thiel, *Nuclear Instruments and Methods in Physics Research Section A: Accelerators, Spectrometers, Detectors and Associated Equipment,* 2017, **845**, 570-574.

100. K. Chowdhury, R. Mandal, *Comprehensive Materials Processing (Second Edition),* 2024, **4**, 151-162.

101. J.-O. Carlsson and P. M. Martin, in *Handbook of Deposition Technologies for Films and Coatings (Third Edition)*, ed. P. M. Martin, William Andrew Publishing, Boston, 2010, 314-363.

102. T. Gong, L. Qin, Y. Hu, J. Li, W. Zhang, L. Hui, H. Feng, *Applied Surface Science*, 2023, **608**, 155200.

103. Lehui Guo, Liwei Xin, Lili Li, Yongsheng Gou, Xiaofeng Sai, Shaohui Li, Hulin Liu, Xiangyan Xu, Baiyu Liu, Guilong Gao, Kai He, Mingrui Zhang, Youshan Qu, Yanhua Xue, Xing Wang, Ping Chen, Jinshou Tian, *Nuclear Instruments and Methods in Physics Research Section A: Accelerators, Spectrometers, Detectors and Associated Equipment,* 2021, **1005**, 165369.

104. T. M. Conneely, J. S. Milnes, J. Howorth, *Nuclear Instruments and Methods in Physics Research A,* 2013, **732**, 388-391.

105. M. Lisowska, R. Aleksan, Y. Angelis, S. Aune, J. Bortfeldt, F. Brunbauer, M. Brunoldi, E. Chatzianagnostou, J. Datta, K. Dehmelt, G. Fanourakis, S. Ferry, D. Fiorina, K.J. Floethner, M. Gallinaro, F. Garcia, I. Giomataris, K. Gnanvo, F.J. Iguaz, D. Janssens, A. Kallitsopoulou, M. Kovacic, B. Kross, C.C. Lai, P. Legou, J. Liu, M. Lupberger, I. Maniatis, J. McKisson, Y. Meng, H. Muller, R. De Oliveira, E. Oliveri, G. Orlandini, A. Pandey, T. Papaevangelou, M. Pomorski, M. Robert, L. Ropelewski, D. Sampsonidis, L. Scharenberg, T. Schneider, E. Scorsone, L. Sohl, M. van Stenis, Y. Tsipolitis, S. Tzamarias, A. Utrobicic, I. Vai, R. Veenhof, L. Viezzi, P. Vitulo, C. Volpato, X. Wang, S. White, W. Xi, Z. Zhang, Y. Zhou, *Nuclear Instruments and Methods in Physics Research Section A: Accelerators, Spectrometers, Detectors and Associated Equipment,* 2025,**1072**, 170151.

106. J. M. Jaramillo, R. D. Mansano, L. S. Zambom, M. Massi, H. S. Maciel, *Diamond and Related Materials*, 2001, **10**, 976-979.

107. N. Budhraja, A. Pal, R. S. Mishra, *International Journal of Hydrogen Energy,* 2023, **48**, 2467-2482.

108. Radical density measurements in microwave plasma with carbon-containing gases used for carbon nanotube and nanocrystalline diamond film growth, https://www.researchgate.net/publication/266504229_Radical_density_measurements_in_microwave_plasma_with_carbon-containing_gases_used_for_carbon_nanotube_and_nanocrystalline_diamond_film_growth (accessed March 2025).

109. S. H. Mortazavi, M. Ghoranneviss, M. Dadashbaba, R. Alipour, *Bulletin of Materials Science,* 2016, **39**, 953-960.

110. K. Racka-Szmidt, B. Slonio, J. Zelazko, M. Filipiak, M. Sochacki, *Materials (Basel)*, 2021, **15**, 123.

111. D. T. Tran, C. Fansler, T. A. Grotjohn, D. K. Reinhard, J. Asmussen, *Diamond and Related Materials*, 2010, **19**, 778-782.

112. H. Mehedi, V. Mille, J. Achard, O. Brinza, A. Gicquel, *Physical Status Solidi,* 2014, **211**, 2343-2346.

113. R. Zulkharnay, G. Zulpukarova, P. W. May, *Applied Surface Science*, 2024, **658**, 159776.

114. R. Asmatulu and W. S. Khan, in *Synthesis and Applications of Electrospun Nanofibers*, eds. R. Asmatulu and W. S. Khan, Elsevier, 2019, 63-87.

115. G. E. Tranter, *Encyclopedia of Spectroscopy and Spectrometry*, 2017, **3**, 740-758.

116. D. L. Andrews, *Encyclopedia of Spectroscopy and Spectrometry*, 2017, **3**, 924-930.

117. H. Vaskova, *International Journal of Mathematical Models and Methods in Applied Sciences,* 2011, **5**, 1205-1212.

118. J. Filik, *Spectroscopy Europe,* 2005, **17**, 10-17.

119. S. Yao, H. Li, S. Pang, B. Zhu, X. Zhang, S. Fatikow, *IEEE Transactions on Instrumentation and Measurement*, 2021, **70**, 1-28.

120. J. Webb, J. H. Holgate, *Encyclopedia of Food Sciences and Nutrition (Second Edition)*, 2003, **1**, 3922-3928.

121. A. D. Micheals, *Encyclopedia of Forensic Sciences*, 2013, **1**, 483-493.

122. M. Ceniceros-Reyes, F. Rodriguez, Y. Perera-Mecrado, E. Saucedo-Salazar, E. D. Barriga-Castro, *Acta Microscopica*, 2014, **23**, 78-84.

123. J. A. Gamble, S. B. Milne, *Journal of Archaeological Science: Reports*, 2018, **18**, 847-857.

124. Basic Principles of Laser Scanning Microscopes, https://evidentscientific.com/en/learn/knowledge/metrology/lext-principles (accessed March 2025).

125. LEXT OLS5100 Laser Microscope, https://evidentscientific.com/en/products/digital-imaging/lext-ols5100 , (accessed March 2025).

126. Bristol NanoESCA Facility, https://www.bristol.ac.uk/physics/facilities/nanoesca/ , (accessed April 2025).

127. Kimball Physics Electron Guns Tutorial and Resource, https://www.kimballphysics.com/wp-content/uploads/2023/09/Electron_Gun_Tutorial_Resource_2023_0606.pdf , (accessed March 2025).

128. A. Masoumzadeh, M. Habibi, M. Afsharmanesh, *Vacuum*, 2019, **159**, 99-104.

129. J. E. Yater, A. Shih, J. E. Butler, P. E. Pehrsson, *Applied Surface Science,* 2002, **191**, 52-60.

130. K. Nishimura, T. Itotani, K. Ohya, *Japanese Journal of Applied Physics,* 1994, **33,** 4727.

131. R. Bogdanowicz, M. Ficek, N. Malinowska, S. Gupta, R. Meek, P. Niedziałkowski, M. Rycewicz, M. Sawczak, J. Ryl, T. Ossowski, *Journal of Electroanalytical Chemistry*, 2020, **862**, 114016.

132. X. Chang, Q. Wu, I. Ben-Zvi, A. Burrill, J. Kewisch, T. Rao, J. Smedley, E. Wang, E. M. Muller, R. Busby and D. Dimitrov, *Physical Review Letters*, 2010, **105**, 164801.

133. E. Piatti, A. Pasquarelli, R. S. Gonnelli, *Applied Surface Science,* 2020, **528**,146795.

134. R. L. Harniman, O. J.L. Fox, W. Janssen, S. Drijkoningen, K. Haenen, P. W. May, *Carbon,* 2015, **94**, 386-395.

135. R. Vaz, PhD Thesis, The University of Bristol, 2007.

136. K. Wei, S. Wu, H. Wang, *Journal of Electronic Materials,* 2018, **47**, 4823-4830.

137. Element Six Limited, United States Patent, 8986645, 2015.

138. V. Mortet, A. Taylor, Z. V. Živcová, D. Machon, O. Frank, P. Hubík, D. Tremouilles, L. Kavan, *Diamond and Related Materials*, 2018, **88**, 163-166.

139. P. W. May, W. J. Ludlow, M. Hannaway, P. J. Heard, J. A. Smith, K. N. Rosser, *Diamond and Related Materials*, 2008, **17**, 105-117.

140. M. Bernard, A. Deneuville, P. Muret, *Diamond and Related Materials*, 2004, **13**, 282-286.

141. Y. Gong, W. Jia, B. Zhou, K. Zheng, J. Gao, Y. Wu, Y. Wang, S. Yu, Y. Xue, Y. Wu, *Applied Surface Science*, 2024, **659**, 159838.

142. F. Pruvost, A. Deneuville, *Diamond and Related Materials*, 2001, **10**, 531-535.

143. N. M. Sulthana, K. Ganesan, P. K. Ajikumar, S. Dhara, *Diamond and Related Materials*, 2022, **128**, 109284.